Christian-Albrechts-Universität zu Kiel

Processing and Inversion of Airborne Gravity Gradient Data

Dissertation
zur Erlangung des Doktorgrades
der Mathematisch-Naturwissenschaftlichen Fakultät
der Christian-Albrechts-Universität zu Kiel

vorgelegt von

Jirigalatu

Kiel 2018

Institut für Geowissenschaften

Erster Gutachter:	Prof. Jörg Ebbing
Zweiter Gutachter:	Prof. Marco Brönner
Tag der Disputation:	03 September 2018

Declaration

I hereby certify that this thesis is my own composition, except the German abstract, which was translated by Peter Haas, all sources have been acknowledged, and my contribution to the thesis is clearly identified. The thesis has not previously been submitted or accepted for a degree at this or another institution. I certify that the work has been undertaken in compliance with the rules of good academic practice of the German Research Foundation.

11.09.2018, Kiel	Jirigalatu
Datum, Ort	Jirigalatu

Abstract

In recent years, due to increased availability of high-resolution measurements of airborne gravity gradiometry (AGG), an ever-increasing number of data processing methods and interpretation approaches have been proposed. Partly, in response to that, some traditional approaches designated to process gravity data are no longer applicable to multi-component gravity gradient data. Moreover, methods capable of taking the multi-component measurements as a whole are invariably advantageous to jointly processing AGG data.

In this thesis, a data-driven method for determining and reducing noise in AGG data will be presented and applied first. The new noise reduction method is based on the idea of iteratively projecting survey data onto a lower level, upward continuing the data back to the original survey height, and then subtracting the upward continued data from the survey data. This method is successfully applied to the AGG data over Karasjok, Norway. The results show that the new noise reduction method can detect some high-frequency noise and systematic errors due to leveling.

Next, a fast equivalent source approach based on Landweber iteration and Gauss Fast Fourier Transform (FFT) is developed. This approach handles two-component gravity gradient measurements simultaneously to preserve their consistency. By applying the method to a synthetic dataset, the method shows great efficiency and the results are less affected by edge effects due to mass outside of the computation area than the standard FFT. Two applications based on the fast equivalent source method are presented. The first is to jointly denoise the AGG data over Karasjok with carefully selected parameters. The results are comparable to the routinely processed data which represents the industry standard. The second is to estimate densities of the topography in Karasjok with the AGG data with a minor modification to the method. The results show that the estimation method is a fast way to acquire an overview of densities of topography when only sparse petrophysical samples are available.

At last, to acquire detailed density distributions of the survey area and evaluate the possibilities for mineralization, a stochastic inversion constrained by a prior lithology model and petrophysical data is applied to the AGG data. Through inverting various combinations of AGG components, the results suggest that noise reduction prior to inversion is not necessary when the existing noise level is low and behaves like zero-mean Gaussian noise. The results also indicate that the constructed and the measured components both can be used for inversion and the inclusion of more than four components in the inversion does not provide additional information. From the acquired density models, insights into potential mineralization in the Karasjok area are provided.

Zusammenfassung

In der jüngsten Vergangenheit haben sich aufgrund der zunehmenden Verfügbarkeit von hochauflösenden Messungen luftgesttzter Schweregradienten (Airborne Gravity Gradients, AGG) eine stetig zunehmende Zahl von Datenprozessierungsmethoden und Interpretationsansätze entwickelt. Im gleichen Zuge sind einige der herkömmlichen Methoden, die zur Prozessierung von Schweredaten angewendet werden, nicht mehr geeignet für multi-komponente Schweregradienten. Darüber hinaus sind diese neuen leistungsfähigen Methoden, die die Messungen der Multi-Komponenten simultan verarbeiten, vorteilhaft für das gemeinsame Prozessieren aller AGG-Daten.

In dieser Arbeit wird eine datengesteuerte Methode zur Bestimmung und Reduzierung von Rauschen (Noise) in den AGG-Daten präsentiert und erstmals angewendet. Die neue Methode zur Noise-Reduzierung basiert auf der iterativen Projizierung eines Datensatzes auf eine niedrigere Höhe mit einer darauffolgenden Feldfortsetzung zurück auf die Vermessungshöhe. Daraufhin werden die feldfortgesetzten Daten von den gemessenen Daten subtrahiert. Damit wird der Noise-Anteil der AGG-Daten halbautomatisch bestimmt und reduziert. Diese Methode wird erfolgreich auf einen AGG-Datensatz, gemessen über Karasjok, Norwegen, angewendet. Die Ergebnisse zeigen, dass die neue Methode zur Noise-Reduzierung in der Lage ist, hochfrequenten Noise und systematische Fehler, die auf die Nivellierung zurückzufhren sind, aufzudecken.

Nächstfolgend wird ein effizienter Equivalent Source-Ansatz, basierend auf der Landweber-Iteration und der Gauss Fast-Fourier-Transformation (FFT) entwickelt. Diese Methode verarbeitet wie gemessene Schweregradienten gleichzeitig, um deren Konsistenz zu bewahren. Bei der Anwendung der Methode auf einen synthetischen Datensatz zeigt diese hohe Effizienz und ist weniger stark von Randeffekten beeinflusst als die übliche FFT. Die Randeffekte werden von Massen außerhalb des Untersuchungsgebiets erzeugt. Zwei Anwendungen, basierend auf der effizienten Equivalent Source-Methode werden präsentiert. Erstere entrauscht die AGG-Daten über Karasjok mit sorgfältig gewählten Parametern. Die Ergebnisse sind vergleichbar mit gewöhnlich prozessierten Daten, wie sie auch in der Industrie bearbeitet werden. Die zweite Methode bestimmt die Dichten der Topografie in Karasjok mit den AGG-Daten mithilfe einer kleinen Änderung der Methode. Die Ergebnisse zeigen, dass diese Methode ein schneller Weg ist, um einen Überblick über die Dichten der Topografie zu bekommen, wenn nur eine geringe Anzahl petrophysikalischer Proben vorhanden ist.

Als letztes wird eine stochastische Inversion, die mit einem bekannten lithologischen Modell und petrophysikalischen Daten eingeschrnkt wird, auf die AGG-Daten angewendet, um detaillierte Dichteverteilungen im Untersuchungsgebiet zu bekommen und die Möglichkeiten für Mineralisation zu evaluieren. Die Ergebnisse der Inversion verschiedener Kombinationen von AGG-Komponenten weisen darauf hin, dass die vor der Inversion durchgeführte Noise-Reduktion nicht erforderlich ist, wenn der vorhandene Noise-Pegel gering ist und sich wie ein mittelwertfreier Gauss-Noise verhält. Sowohl die konstruierten als auch die gemessenen Komponenten können für die Inversion verwendet werden, und die Einbindung von mehr als vier Komponenten in die Inversion führt nicht zu zusätzlichem Informationsgewinn. Anhand der generierten Dichtemodelle werden Einblicke in die potentielle Mineralisation in der Gegend um Karasjok gewonnen.

Acknowledgements

I would first like to thank Prof. Dr. Jörg Ebbing for supporting me through my whole Ph.D time, providing me with the tools that I needed to choose the right direction and complete my dissertation, and also providing me great opportunities to work with excellent colleagues and minds at Kiel University.

I would also like to thank all my colleagues from the Satellite and Airborne Geophysics group for their great help and the friendly working environment.

I would like to thank Wolfgang Szwillus, my officemate, for his great help in both scientific work and life. We not only support each other by deliberating over our problems and findings, but also happily by talking about things other than just scientific stuff.

Peter Haas, I want to thank you for translating my abstract into German, excellent work.

I would like to thank Mohamed Sobh and Andreas Steinberg for proofreading my thesis and their valuable comments.

I would also like to thank my parents and my friends for their wise counsel and sympathetic ear.

I thankfully acknowledge the Geological Survey of Norway for making the Karasjok survey dataset available for my study.

Thank you very much, everyone!

Jirigalatu

Kiel, July 2018

Contents

Chapter 1

Introduction

Airborne gravity gradiometry systems have been capable of measuring one or more combinations of gravity tensor components efficiently over large and inaccessible areas (Fullagar and Glenn, 2010). As a result, gravity gradiometry has become an accepted and important tool in exploration and oil field geophysics in the search for mineral deposits (DiFrancesco et al., 2009b; Pawlowski, 1998; Kass and Li, 2008).

Although gravity gradiometry is believed to be less affected by many forms of noise than conventional gravimetry surveys, low-pass filtering is still routinely applied before data are delivered to customers (Kass and Li, 2008). For that reason, awareness of all potential noise sources is vital to reduce misinterpretation.

Several broadly accepted noise sources will mask the real signals of interest (Pilkington and Shamsipour, 2014). In general, the noise sources are divided into those related to the instrument normally due to the design of the instrument and those introduced by the routine terrain correction and leveling made to remove undesirable parts from the AGG data (Dransfield and Christensen, 2013). In addition, dynamic noise as the significant part of the noise in AGG data increases with the level of air turbulence experienced during a survey (Dransfield and Milkereit, 2007). As a consequence, the noise level is higher in reality than that in lab conditions.

Therefore, noise reduction plays an important role in processing AGG data. Although various approaches for noise reduction have been proposed (Oliveira Lyrio et al., 2004; While et al., 2006; Pajot et al., 2008; Pilkington and Shamsipour, 2014), reducing noise to an acceptable level without sacrificing too much high-frequency content in AGG data still remain challenging (Pilkington and Shamsipour, 2014), especially due to the difficulty in distinguishing noise from useful information (Jirigalatu et al., 2016).

Since normally more than one component is acquired, jointly filtering of all AGG data components is used to preserve their internal consistency and reduce the overall noise level (Pajot et al., 2008; Sanchez et al., 2005). Therefore, an appropriate approach, capable of handling multi-component measurements without corrupting their internal consistency, such as the equivalent source method, is highly desirable (Davis and Li, 2011; Martinez and Li, 2016).

Moreover, because a reliable density distribution map of the survey area through geophysical inversion will significantly facilitate the interpretation, so geophysical inversion is widely used for a quantitative interpretation (Nabighian et al., 2005; Martinez et al., 2013). In quantitatively interpreting geophysical observations, the conventional deterministic inversion plays a dominant role (Li and Oldenburg, 1996; Li and Oldenburg, 1998; Portniaguine and Zhdanov, 1999; Leliévre et al., 2012). Pilkington (2012; 2014) and Paoletti et al. (2016) argue that the choice of gravity gradient tensor components used for an inversion should be carefully made simply because inverting too many components will significantly increase computation complexity. However, few studies have systematically addressed if the choice of tensor components matters in stochastic inversion of AGG data. To solve non-linear multi-component inverse problems, geostatistic or stochastic methods e.g. (Guillen et al., 2004; Bosch et al., 2006; Shamsipour et al., 2010) appear advantageous.

To better understand the Karasjok Greenstone belt, a lithology model of the survey area in Karasjok was built by Skaar (2014) based on structural analysis, lithological interpretation and density distribution information from rock samples. A prior model composed of formations with constant densities does not provide a satisfactory fit to the short-wavelength content of the AGG data, which is believed to be associated with potential mineralization near the surface. To get a density distribution of the area by simultaneously inverting the existing geological, geophysical and petrophysical data leads to great non-linearity. Therefore, stochastic inversion based on Bayes' theorem is well-suited to untangling the problem.

Structure of the thesis

- **Chapter 2**: this chapter is dedicated to explaining the basic theories of the gravity gradients and some general information about gravity gradiometers
- **Chapter 3**: this chapter provides *a priori* information on the airborne gravity gradient data along with the survey area.
- **Chapter 4**: in this chapter, an iterative noise reduction will be presented. This method was originally published on a paper *A new noise reduction method for airborne gravity gradient data* published in *Exploration Geophysics*.
- **Chapter 5**: this chapter presents a fast way of calculating equivalent source technique and some useful application of the equivalents source technique. It is based on the work of an article submitted to *Geophysics*.
- **Chapter 6**: this chapter shows the stochastic inversion which is applied to the AGG data over Karasjok, Norway so as to obtain density distribution of the survey area, as a result of a need of a quantitative interpretation of the data. It is based on a manuscript in preparation.
- **Chapter 7**: this chapter summarizes the findings of this work and gives an outlook.

Author's contribution

The thesis is based on the author's work during his Ph.D under the supervision of Prof. Jörg Ebbing.

Chapter 4: the chapter has been published in *Exploration Geophysics*. The author developed the theory and performed the computations. Prof. Jörg Ebbing and Dr. Josef Sebera verified the analytical methods and supervised the findings of this work. All authors discussed the results and contributed to the final manuscript.

Chapter 5: the author developed the theoretical formalism, performed the analytic calculations and performed the numerical simulations. Prof. Jörg Ebbing provided critical feedback and helped shape the research, analysis and manuscript.

Chapter 6: the author conceived and planned the experiments. The author carried out the experiments. The author was responsible for compiling results and writing the manuscript. Prof. Jörg Ebbing supervised the findings of the work.

Chapter 2

Theory

2.1 Basic Concepts

A field is a set of functions of space and time. The gravitational attraction of the earth, namely the gravity field, is a vector field which has both magnitude and direction. The gravity field is inherently *conservative* and *harmonic* (Blakely, 1996). Conventionally, the relation between the field $\mathbf{F}$ and the potential U for gravity field is expressed (Kellogg, 2012)

$$\mathbf{F} = \nabla U. \tag{2.1}$$

In summary, if $\mathbf{F} = \nabla U$, then vector field $\mathbf{F}$ is *conservative* and is said to be a potential field vice versa (Blakely, 1996). Regarding the gravity field $\mathbf{g}$, the relation is

$$\mathbf{g} = \nabla U. \tag{2.2}$$

$$\nabla U\left(x, y, z\right) = U_x\mathbf{i} + U_y\mathbf{j} + U_z\mathbf{k} = \mathbf{g}\left(x, y, z\right). \tag{2.3}$$

In other words, the gravity field is the spatial changing rate of gravity potential along x, y and z directions in the Cartesian coordinate system. In this sense, the gravity field has three components $\mathbf{g}_x$, $\mathbf{g}_y$ and $\mathbf{g}_z$. As a result, there are nine gravity gradient components, which correspond to the second spatial derivatives of the gravity potential. The whole set of the gravity gradient components (Equation 2.4) is called gravity gradient tensor (GGT) (Dransfield and Milkereit, 2007).

$$\mathbf{FTG} = \begin{pmatrix} \mathbf{G}_{\mathrm{xx}} & \mathbf{G}_{\mathrm{xy}} & \mathbf{G}_{\mathrm{xz}} \\ \mathbf{G}_{\mathrm{yx}} & \mathbf{G}_{\mathrm{yy}} & \mathbf{G}_{\mathrm{yz}} \\ \mathbf{G}_{\mathrm{zx}} & \mathbf{G}_{\mathrm{zy}} & \mathbf{G}_{\mathrm{zz}} \end{pmatrix}. \tag{2.4}$$

However, only five components are independent. First of all, the fact that the gravity potential is harmonic dictates that the mixed partial derivatives of the gravity potential

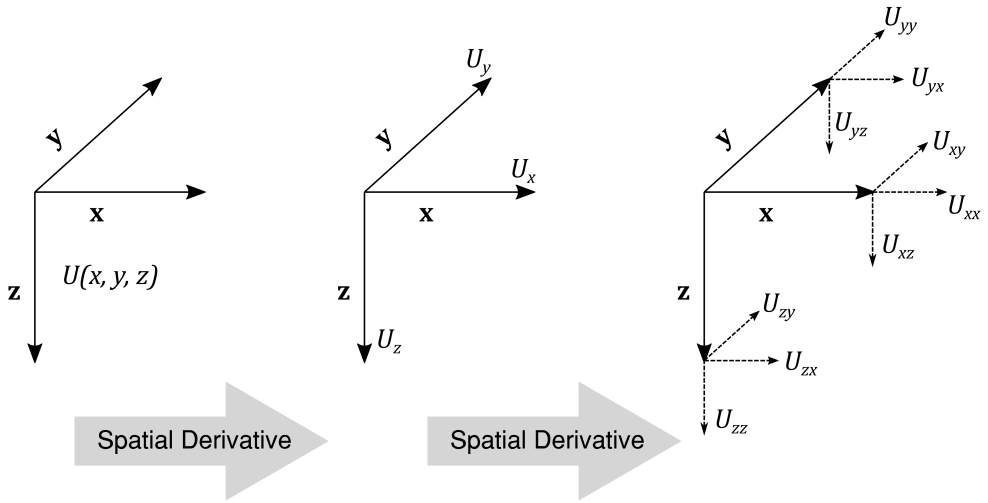

Figure 2.1: Schematic explanation of the relation between the gravity potential, the gravity field and the gravity gradients.

are equal regardless of the order in which they are taken. Therefore, $\mathbf{G}_{\mathrm{xy}}$ component is exactly the same as $\mathbf{G}_{\mathrm{yx}}$, which leads to diagonal symmetry.

Second, the gravity potential satisfies *Laplace's equation* in source-free regions (Blakely, 1996), which can be expressed by

$$\nabla^2 U = \frac{\partial^2 U}{\partial x^2} + \frac{\partial^2 U}{\partial y^2} + \frac{\partial^2 U}{\partial z^2} = 0. \tag{2.5}$$

Since $\mathbf{G}_{\mathrm{xx}}$ is equivalent to $\partial^2 U/\partial x^2$,

$$\mathbf{G}_{\mathrm{xx}} + \mathbf{G}_{\mathrm{yy}} + \mathbf{G}_{\mathrm{zz}} = 0. \tag{2.6}$$

The consequence of Equation 2.6 is the trace of FTG amounting to zero. This reduces the number of independent components to five. Nevertheless, the five independent components are still implicitly related because all of them are derivatives of the gravity field and related to the same causative density heterogeneity.

It is worth noting that in this thesis the upper case of $\mathbf{G}$ with subscripts is used to denote the gravity gradient tensor components, for example $\mathbf{G}_{\mathrm{xy}}$, whereas the lower case $\mathbf{g}$ with a subscript is used to indicate the gravity field components, such as $\mathbf{g}_{\mathrm{z}}$. Besides, regarding units, the gradient tensor components are delivered in Eötvös, which is usually abbreviated to 'Eö', by definition, 1 Eö $= 10^{-9}$ s^{-2}.

Furthermore, it is well-known that potential fields decrease with an increase of distance between the causative source and the observation. For example, if an aperiodic function

$f(x)$ over the x-axis mathematically satisfies the following requirement

$$\int_{+\infty}^{-\infty} |f(x)|\, dx \leq \infty, \tag{2.7}$$

Fourier transform can be applied to potential field (Blakely, 1996). Since Fourier transform is a very important tool in processing of potential field data, it allows filtering in the wavenumber domain (Here the wavenumber domain is equivalent to the frequency domain or Fourier domain) and constructing gradients which are not measured by instruments. With the help of the differentiation property of the Fourier transform gravity gradients (Blakely, 1996), especially for the construction of the horizontal components in 2D case can be effortlessly constructed based on the potential U

$$\frac{\partial^n}{\partial x^n}\frac{\partial^m}{\partial y^m}U(x,y,h_0) \Leftrightarrow (ik_x)^n (ik_y)^m F[U(x,y,h_0)]. \tag{2.8}$$

As for vertically related gravity gradients, it is proven that $\frac{\partial F[U(x,y,z)]}{\partial z}|_{z=h_0}$ is equivalent to $\sqrt{k_x^2+k_y^2}$, where k_x and k_y are the wavenumber along x- and y-axis, respectively. In summary, the relation between the gravity gradients $\mathbf{G}_{ab}$, where $a, b \in [x, y, z]$, and the gravity potential in the wavenumber domain is

$$F[\mathbf{G}_{uv}] = F[U] \cdot \begin{pmatrix} ik_x \cdot ik_x & ik_x \cdot ik_y & ik_x \cdot \sqrt{k_x^2+k_y^2} \\ ik_y \cdot ik_x & ik_y \cdot ik_y & ik_y \cdot \sqrt{k_x^2+k_y^2} \\ \sqrt{k_x^2+k_y^2} \cdot ik_x & \sqrt{k_x^2+k_y^2} \cdot ik_y & k_x^2+k_y^2 \end{pmatrix}. \tag{2.9}$$

The formula described by Equation 2.9 is widely used for gravity gradients construction. This property can be used to facilitate the data processing and data interpretation. Obviously, in Equation 2.9, the gravity gradients are diagonally symmetrical and satisfy the *Laplace's equation* in the wavenumber domain as well.

2.2 FALCON Airborne Gravity Gradiometer

Airborne gravity gradiometry has gained great prosperity and popularity for nearly decades on account of its rapid acquisition and high-resolution measurements (Dransfield and Christensen, 2013; Barnes and Lumley, 2011). In fact, there have been efforts on obtaining real gravity gradient observations for more than a century since the very first gravity gradiometer was introduced in 1886 by Hungarian physicist Baron von Eötvös (Chen and

Macnae, 1997; Zhdanov et al., 2004). This device was employed for various prospecting purposes in the early 1900s (DiFrancesco et al., 2009a). Since then, geophysicists put forward different approaches for the gravity gradient data acquisition. Nevertheless, no commercial gravity gradiometer instrument came into routine use prior to the 1970s (Chen and Macnae, 1997). During the 1970s, due to the US Navy's need of the covert and high-resolution navigation system for submarines, the Full Tensor Gravity (FTG) system was under development by Bell Aerospace (later acquired by Lockheed Martin). As the Cold War came to a close, the US Navy declassified the technology of Gravity Gradient Instrument (GGI) and opened the door for full commercialization of the technology (DiFrancesco et al., 2009a).

As a result of a feasibility study (Dransfield et al., 1991) and under an agreement with Lockheed Martin Australian, BHP Billiton (Australia) designed an airborne gravity gradiometer between 1991 and 2000 on the basis of the GGI technology, now FALCON™ Airborne Gravity Gradiometer (AGG) (Evstifeev, 2017). Following a series of tests and modifications, the system with the modified design was installed in a Cessna Grand Caravan aircraft. In October 1999, the first airborne gravity gradiometry survey was flown over the Bathurst Camp in New Brunswick by Sander Geophysics for BHP Billiton (Dransfield et al., 2001; Dransfield and Milkereit, 2007). The system has been proven suitable for use in mineral exploration with sufficient sensitivity and resolution for the detection of the small localized gravity anomalies associated with mineral deposits as well as for local mapping (DiFrancesco et al., 2009a).

Numerically, the gravity gradients can be deduced by differencing the value of gravity at two points separated by a small distance and dividing by this distance. Therefore, the changing rate of the gravity field can be measured by installing multiple pairs of accelerometers. It is the reason that in the original GGI, four equi-spaced accelerometers are mounted on a round disc, with their sensitive axes tangential to the circle with the same sense (Metzger, 1982). The accelerometers aligning with the positive direction of X-axis and Y-axis such as A4 and A1 in Figure 2.2a are positive and otherwise negative. The disc revolves slowly about the vertical spin axis at the speed of $\Omega = 0.5\pi$ rad/s so that the group of accelerometers are able to measure $\mathbf{G}_{\mathrm{NE}}$ and $\mathbf{G}_{\mathrm{UV}}$, where $\mathbf{G}_{\mathrm{UV}} = (\mathbf{G}_{\mathrm{NN}} - \mathbf{G}_{\mathrm{EE}})/2$, because GGI system adopts a North, East, and Down geographic coordinate system. The N (North), E (East), and D (Down) directions correspond to y, x, and z in the conventional

Cartesian coordinate system, respectively (Dransfield and Milkereit, 2007).

$$\left.\begin{aligned} A(t) &= \frac{(\mathrm{A1}+\mathrm{A2})-(\mathrm{A3}+\mathrm{A4})}{2R}, \\ B(t) &= \frac{(\mathrm{B1}+\mathrm{B2})-(\mathrm{B3}+\mathrm{B4})}{2R}. \end{aligned}\right\}$$

By following the nomenclature introduced in Section 2.1 and using directions (N, E, and D) as subscripts to denote the gravity gradient components, the measured component $\mathbf{G}_{\mathrm{NE}}$ is the north-east component, which is the gradient in the east direction of $\mathbf{g}_{\mathrm{N}}$. In that sense, $\mathbf{G}_{\mathrm{NN}}$ is the north gradient of $\mathbf{g}_{\mathrm{N}}$ whereas $\mathbf{G}_{\mathrm{EE}}$ is the east gradient of $\mathbf{g}_{\mathrm{E}}$. Concerning $\mathbf{G}_{\mathrm{UV}}$, it is the half of the difference between $\mathbf{G}_{\mathrm{NN}}$ and $\mathbf{G}_{\mathrm{EE}}$ (Dransfield and Milkereit, 2007). Because the two measured components are associated with the curvatures of the equipotential surface, the two measured component are also known as the curvature gradients (Slotnick, 1932; Li, 2015).

BHP Billiton enlarged the diameter of the rotating disc so that FALCON gravity gradiometer has sufficient room for eight accelerometers. The eight accelerometers work as two independent instruments. This exclusive design provides relatively lower noise on the average readings in comparison with the four-accelerometer setup. The FALCON gravity gradiometer acquires two curvature components, namely $\mathbf{G}_{\mathrm{NE}}$ and $\mathbf{G}_{\mathrm{UV}}$ as well. However, in comparison with the original GGI, the FALCON gradiometer during acquisition gives a pair of independent readings at each sample point for each component, which leads to two separate measured data sets simultaneously for each component. Despite the fact that these curvature components cannot intuitively be related to the causative geology, the directly measured $\mathbf{G}_{\mathrm{NE}}$ and $\mathbf{G}_{\mathrm{UV}}$ data are appropriate to be used in inversion (Fugro Data Processing Report, 2011).

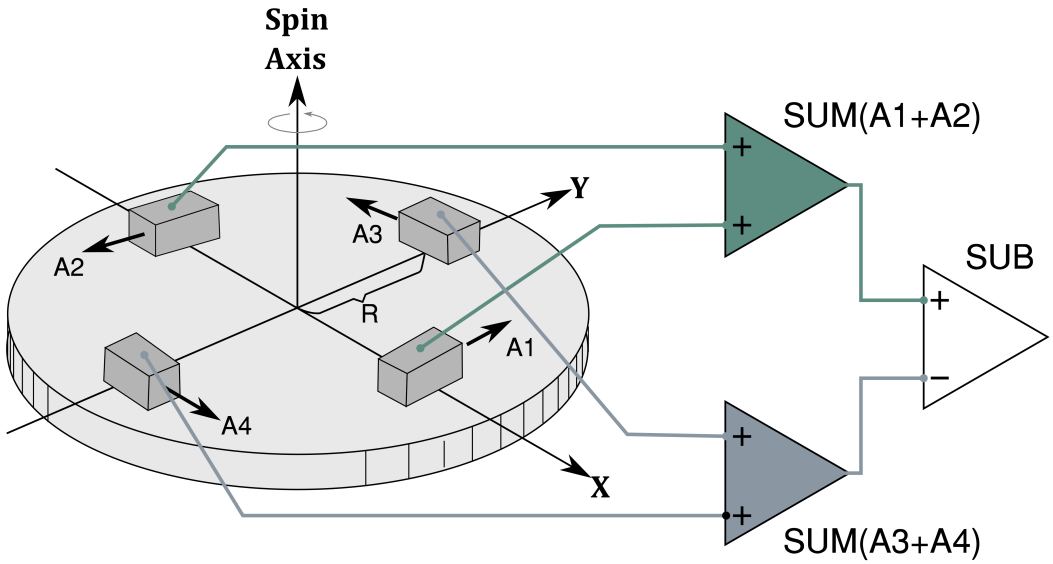

(a)

(b)

Figure 2.2: (a) Schematic diagram of the gravity gradient instrument. The sensitive axes of the accelerometers are indicated by arrows (Hofmeyer and Affleck, 1994), (b) the FALCON gravity gradiometer (DiFrancesco et al., 2009a).

2.3 Gravity Gradiometry vs. Gravimetry

Nowadays some gravity gradiometers such as FALCON AGG are compact enough to be installed in a moving platform such as fixed aircrafts, ships, which leads to fast coverage over a large area (Dransfield and Milkereit, 2007). This makes them especially well-suited for surveys in remote and inaccessible areas. Also, it is a relatively cost-effective method in comparison with other geophysical methods (Zhdanov et al., 2011). Airborne gravity gradiometry normally delivers more than one gravity gradient components which provide extra constraints for inversion. Furthermore, AGG data are known for their high sensitivity to near-surface sources (Dransfield and Christensen, 2013). From Figure 2.3, it can be seen that the resolution of the vertical gravity gradient data is significantly improved compared to the vertical gravity data. It means that the vertical gravity gradient $\mathbf{G}_{\mathrm{DD}}$ is more sensitive to small or shallow sources and has higher spatial resolution than the vertical gravity.

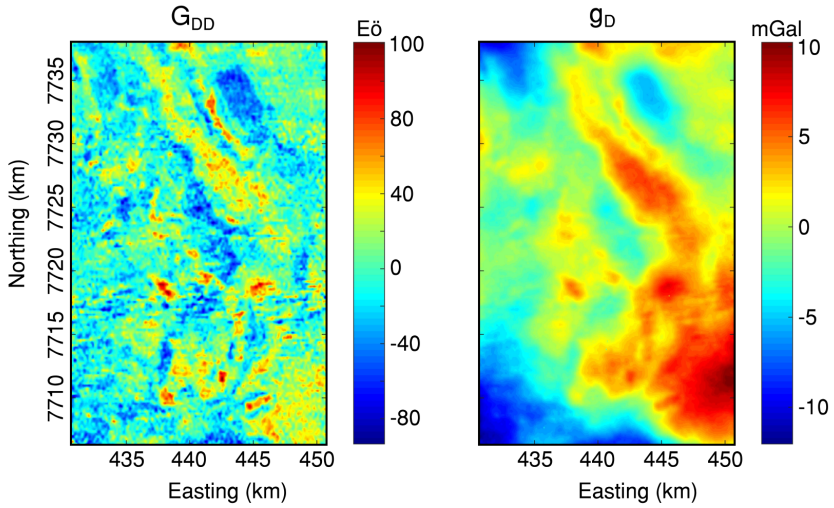

Figure 2.3: A comparison between vertical gravity gradient data $\mathbf{G}_{\mathrm{DD}}$ on the left panel and vertical gravity data $\mathbf{g}_{\mathrm{D}}$ on the right panel, collected at Karasjok, Norway.

Moreover, the vertical gravity measurement must be thoroughly and carefully corrected in practice such as free air correction, Bouguer correction, terrain correction, latitude correction, tidal correction and so on (Roy, 2007). These required corrections will inevitably introduce some artifacts which may affect the further interpretation, whereas gravity gradient measurement only requires terrain correction (DiFrancesco et al., 2009a).

Chapter 3

Airborne Gravity Gradient Data

The survey area is located northwest to Karasjok, Norway, covering the Karasjok Greenstone Belt. The Greenstone is mainly composed of Archean and Paleoprotozoic rocks. This geological setting is a favorable site for potential mineralization. Therefore, a regional gravity gradiometry survey was undertaken by Fugro Geosciences[1] for high-resolution gravity gradient measurements. The survey was conducted in an rectangular area centered on longitude 25°30' E, latitude 69°35' E (Figure 3.1). The production flights took place during August 2011. To complete the survey area coverage, a total of 6 production flights were flown and 3291 line kilometers of data were acquired in total. The survey covers an area of 31.7 × 19.7 km. The traverse line spacing is 200 m and there are 159 traverse lines and 5 tie lines (Fugro Data Processing Report, 2011).

As the aforementioned instrumental configuration, the AGG is capable of delivering two sets of the output simultaneously. The two separate observations are marked by A and B (Figure 3.2), respectively. From the two sets of measurements A and B, as for the measured $\mathbf{G}_{\mathrm{NE}}$, it is just an average of $\mathbf{A}_{\mathrm{NE}}$ and $\mathbf{B}_{\mathrm{NE}}$. As to the measured $\mathbf{G}_{\mathrm{UV}}$, the same rule is applied.

3.1 Noise

As a result of two separate measurements, we are able to estimate the inherent systematic noise. Assuming that the average of $\mathbf{A}_{\mathrm{NE}}$ and $\mathbf{B}_{\mathrm{NE}}$ is more accurate than either $\mathbf{A}_{\mathrm{NE}}$ or $\mathbf{B}_{\mathrm{NE}}$ alone (the incompatible part can be canceled out and the common part will be reinforced), the differences between the average and either A or B measurement can be considered noise. For that reason, the system noise is defined to be the standard

[1]Fugro Geosciences was responsible for the data acquisition and the data processing.

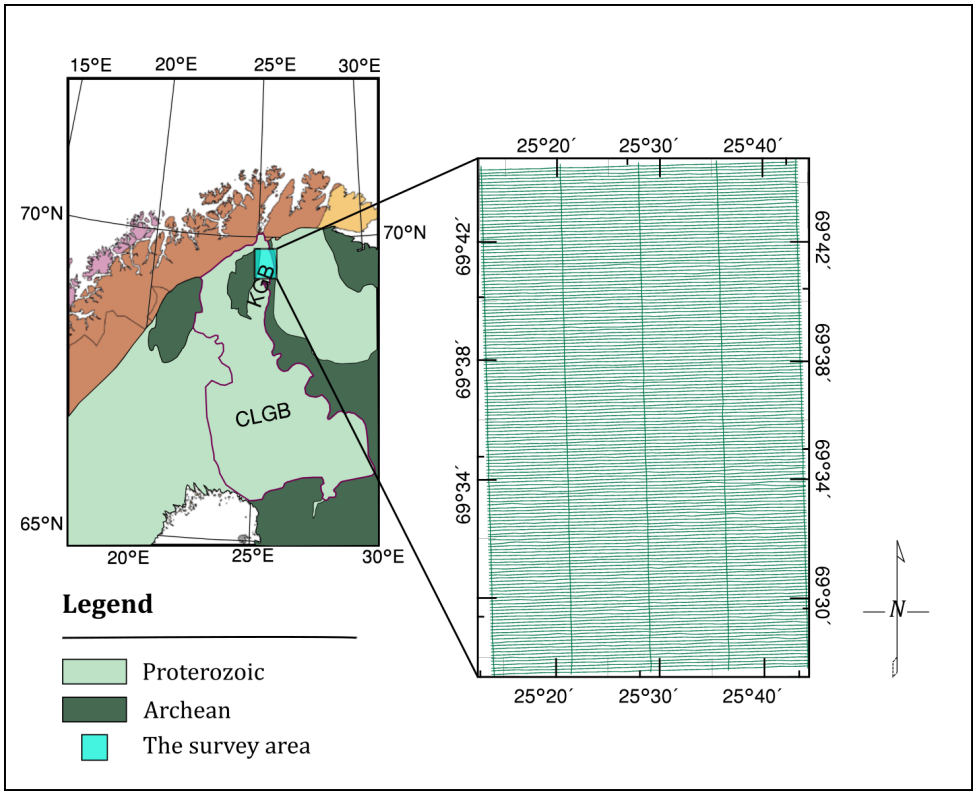

Figure 3.1: The geological setting and the traverse lines of the survey. KGB and CLGB stand for Karasjok Greenstone Belt and Central Lapland Greenstone Belt, respectively.

deviation of half the difference between the A & B components, for each of the $\mathbf{G}_{\mathrm{NE}}$ and $\mathbf{G}_{\mathrm{UV}}$ components (Fugro Data Processing Report, 2011). The standard deviation is used because the difference has been shown to follow a Gaussian statistical distribution, with a mean of zero (Dransfield and Christensen, 2013). Therefore, 95% of the systematic noise will lie between -2σ and $+2\sigma$ of the mean. For a typical survey noise estimate of, say, 3 Eö, 95% of the noise amplitude will be between ± 6 Eö. These typical errors in the curvature gradients translate to errors in $\mathbf{G}_{\mathrm{DD}}$ of about 5 Eö (Fugro Data Processing Report, 2011).

Because the respective estimated noise level for $\mathbf{G}_{\mathrm{NE}}$ and $\mathbf{G}_{\mathrm{UV}}$ is reported to be 3.71 Eö and 3.58 Eö, so in our case, 95% of the noise is between ± 7.42 Eö. Figure 3.3 displays the estimated systematic noise for each component.

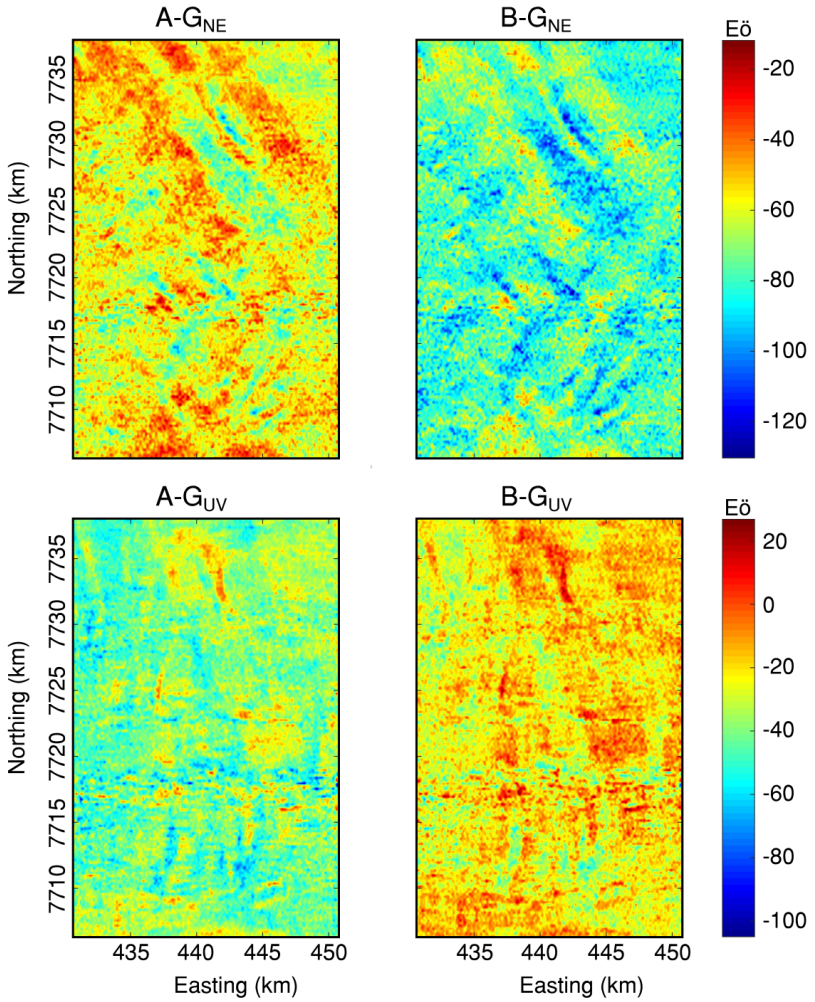

Figure 3.2: The two sets of $\mathbf{G}_{\mathrm{NE}}$ and $\mathbf{G}_{\mathrm{UV}}$ measurements after topographic correction.

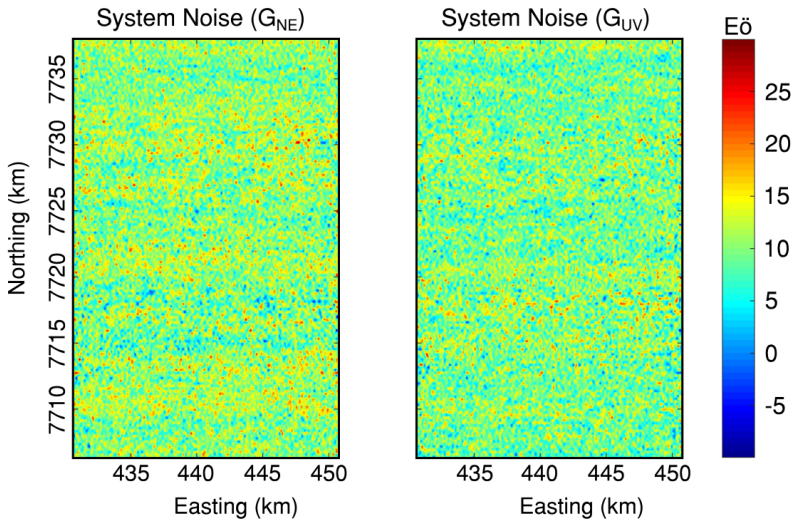

Figure 3.3: The estimated system noise of $\mathbf{G}_{\mathrm{NE}}$ and $\mathbf{G}_{\mathrm{UV}}$

3.2 Data Processing

The main sequence of processing of the gravity data are as following (Fugro Data Processing Report, 2011):

- Dynamic corrections, namely Post Mission Compensation, are designated to reduce residual aircraft motion due to the design and operation of the FALCON AGG system. Following a series of proprietary corrections, the gradient data are then demodulated and filtered along line with a 6-pole Butterworth low-pass filter with a cut-off frequency of 0.18 Hz for fixed-wing operations.

- Self gradient corrections are applied to reduce the time-varying gradient response from the aircraft and platform.

- Terrain corrections are applied.

- Leveling is applied to correct the resolution problem caused by GPS during the acquisition. The terrain- and self gradient-corrected $\mathbf{G}_{\mathrm{NE}}$ and $\mathbf{G}_{\mathrm{UV}}$ data are tie-leveled across the entire survey using a least-squares minimization of differences at survey line intersections.

- $\mathbf{G}_{\mathrm{NE}}$ and $\mathbf{G}_{\mathrm{UV}}$ are transformed into the full tensor gravity.

3.2.1 Terrain corrections

Gravity gradient data are highly sensitive to near surface masses (Chinnery, 1961). The topographic effect is constantly seriously masking airborne gravity gradient measurements, due to the significant density difference between the crust and the air (Chen and Macnae, 1997; Zengerer et al., 2016). Consequently, uncorrected gravity gradient data have a high correlation with topography (DiFrancesco et al., 2009a). Distinguishing the signature of topography from near-surface geology is important to gravity gradient survey data (DiFrancesco et al., 2009a).

For airborne gravity gradiometry at low survey altitudes, a detailed digital terrain map (DTM) shown in Figure 3.4 is required for terrain correction. Typically, an acceptable digital terrain map will need to be sampled at a cell size roughly one-third to one-half of the survey height with a position accuracy of better than 1 m and large enough to cover area in a distance of 10 km from each survey measurement point (Stone and Simsky, 2001; Dransfield and Zeng, 2009).

In the calculation of terrain corrections for $\mathbf{G}_{\mathrm{NE}}$ and $\mathbf{G}_{\mathrm{UV}}$, a density which is able to represent the terrain of the survey area is desirable. Empirically, 2.67 g/cm^3 was used for terrain correction (Hinze, 2003). Generally, 2.67 g/cm^3 will work well for most terrain types but may still lead to over correction or under correction in some areas (Fugro Data Processing Report, 2011). Comparing the DTM with the terrain-corrected $\mathbf{G}_{\mathrm{DD}}$ map for different densities is a reliable way to confirm the legitimacy of terrain correction. Regarding adopting a new density value for terrain correction, there is a simply method by following a linear relation between terrain-corrected $\mathbf{G}_{\mathrm{NE}}(\rho_1)$ and non-terrain-corrected $\mathbf{G}_{\mathrm{NE}}(\rho_2)$ data. Therefore, the new corrected data with new terrain correction density $\mathbf{G}_{\mathrm{NE}}(\rho_{\mathrm{new}})$ is given by

$$\mathbf{G}_{\mathrm{NE}}(\rho_{\mathrm{new}}) = \mathbf{G}_{\mathrm{NE}}(\rho_1) + \left[\frac{\mathbf{G}_{\mathrm{NE}}(\rho_2) - \mathbf{G}_{\mathrm{NE}}(\rho_1)}{\rho_2 - \rho_1}\right]. \tag{3.1}$$

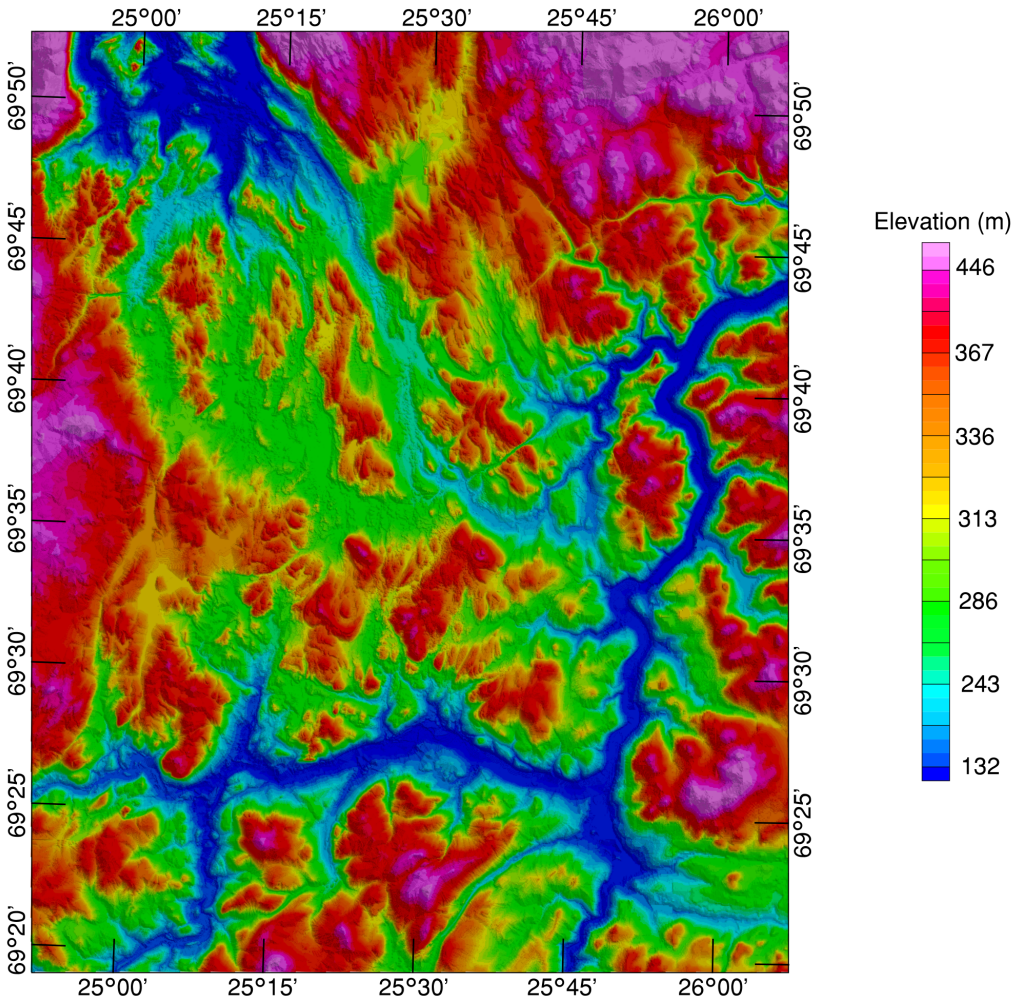

Figure 3.4: The digital terrain map used for terrain correction of the AGG data over Karasjok, Norway.

3.2.2 Transforming into full tensor gravity

Because the AGG system measures only two non-vertical gravity gradients $\mathbf{G}_{\mathrm{NE}}$ and $\mathbf{G}_{\mathrm{UV}}$, the full tensor gravity (FTG) has to be constructed, either by applying Fourier transformation or the equivalent source method (Nabighian et al., 2005; Barnes and Lumley, 2011). For future reference, constructed data are acquired based on the above construction methods whereas measured data in this thesis are direct measurements of FALCON AGG system without any construction process.

3.2.2.1 The Fourier transform technique

Remember the relation between the gravity gradients and the gravity potential in Equation 2.9 in the page of 6. So as to avoid artifacts caused by singularities at $k_x = 0$ or $k_y = 0$ in the construction process, the application of the complex function $\mathbf{G}_{\mathrm{NE}} + \mathbf{i}\mathrm{G}_{\mathrm{UV}}$ for the transform is adopted because this complex function provides a stable and accurate calculation for the transform (Pilkington, 2014). This construction is based on the following relation,

$$\begin{cases} F[\mathbf{G}_{\mathrm{NE}}] = k_x k_y \cdot F[U] \\ F[\mathbf{G}_{\mathrm{UV}}] = \dfrac{k_x^2 - k_y^2}{2} \cdot F[U]. \end{cases} \tag{3.2}$$

So in the wavenumber domain, the new measurement $\mathbf{G}_{\mathrm{NE}} + \mathrm{i}\mathbf{G}_{\mathrm{UV}}$ becomes

$$F[\mathbf{G}_{\mathrm{NE}} + \mathrm{i}\mathbf{G}_{\mathrm{UV}}] = \left(k_x k_y + \mathrm{i}\frac{k_x^2 - k_y^2}{2} \right) F[U]. \tag{3.3}$$

In that case, the gravity potential is retrieved by the following expression (Lee, 2001)

$$F[U] = \frac{-2\mathrm{i}}{(k_x - k_y)^2} \cdot F[\mathbf{G}_{\mathrm{NE}} + \mathrm{i}\mathbf{G}_{\mathrm{UV}}]. \tag{3.4}$$

By examining Equation 3.4, the formula is singular only when $k_x = 0$ and $k_y = 0$. With Equation 3.4 in conjunction with Equation 2.9 in the page of 6, the FTG components can be constructed in the Fourier transform domain. Figure 3.5 shows the constructed FTG. Theoretically, in the transform, coherent signals are reinforced but noise components that out of phase tend to be reduced after the transform (Pilkington, 2014). It is noteworthy that Fugro Geosciences also uses a low-pass filter to improve the signal-to-noise ratio by removing processing artifacts and other information which is known to be beyond the sampling resolution. A cut-off wavelength of 200 m was used in the low-pass filter (Fugro Data Processing Report, 2011).

However, even with the relation shown in Equation 3.4, some trivia such as data extension to make input gradient data periodic and compatible are worth some attention. Otherwise, incompatibility caused by careless data preparation will introduce strong artifacts.

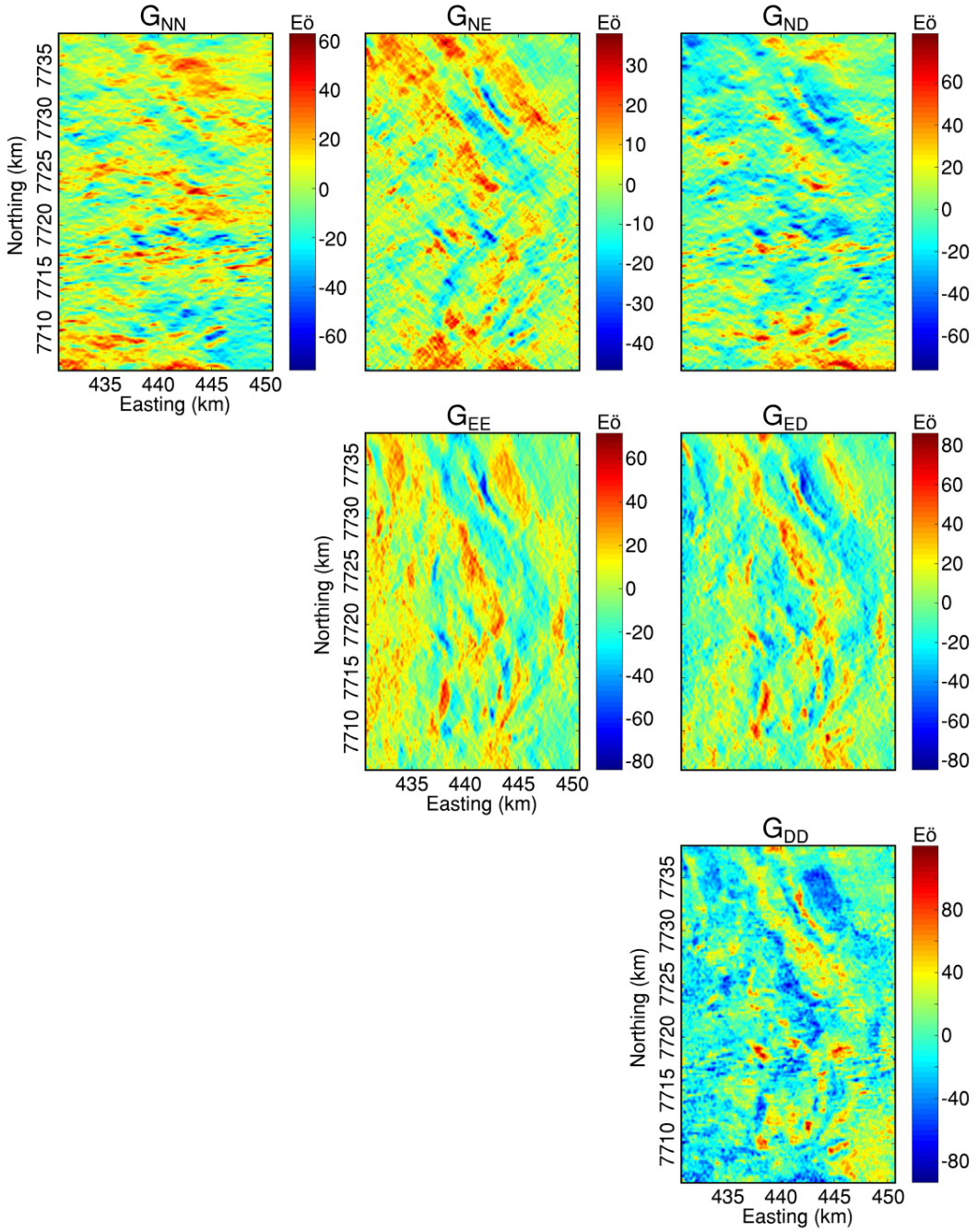

Figure 3.5: The constructed full tensor gravity (FTG) based on Fourier transform provided by Fugro Geosciences.

3.2.2.2 The equivalent source technique

The equivalent source technique (Dampney, 1969) constructs an equivalent source layer that satisfies all components at all locations within the data grid (Sanchez et al., 2005). It means that the inherent relationship among the different components of gravity gradiometer data requires that the processing applied to the data must be consistent from component to component. The gravity gradients are a response caused by density heterogeneity of the earth. As a result, in addition to computing the gravity potential in the wavenumber domain, density is an alternative to construct the gravity gradients.

The aim of the equivalent source construction is to find a fictitious source layer that can reproduce all data simultaneously. A natural solution to the problem is to use a laterally varying layer of density, which is normally discretized into a set of pixels with a constant density value inside each pixel, and then to place it at some distance below the observational surface. This set of values, together with the depth, thickness,and horizontal sizes, define the equivalent source layer. As a rule, the equivalent source layer is considered to be placed as close to the observation surface as possible to ensure that the short-wavelength content will be kept in the constructed data (Li, 2001).

It is possible to closely match the wavelength characteristics of the Fourier transform results by placing the sources at a depth of 200 meters (Fugro Data Processing Report, 2011). However, this technique involves too much computation and the risk of over-smoothing and under-smoothing the data (Pilkington, 2014). Therefore, Fugro Geosciences only provided three components $\mathbf{G}_{\mathrm{DD}}$, $\mathbf{G}_{\mathrm{NE}}$ and $\mathbf{G}_{\mathrm{UV}}$ which were constructed or reconstructed with the equivalent source technique (Figure 3.6).

The equivalent source method relies on a smooth model inversion to calculate the density of a surface of sources and from these sources, a forward calculation provides FTG. The smoothing results in an output that is equivalent to the result of the low-pass filter in the Fourier domain method.

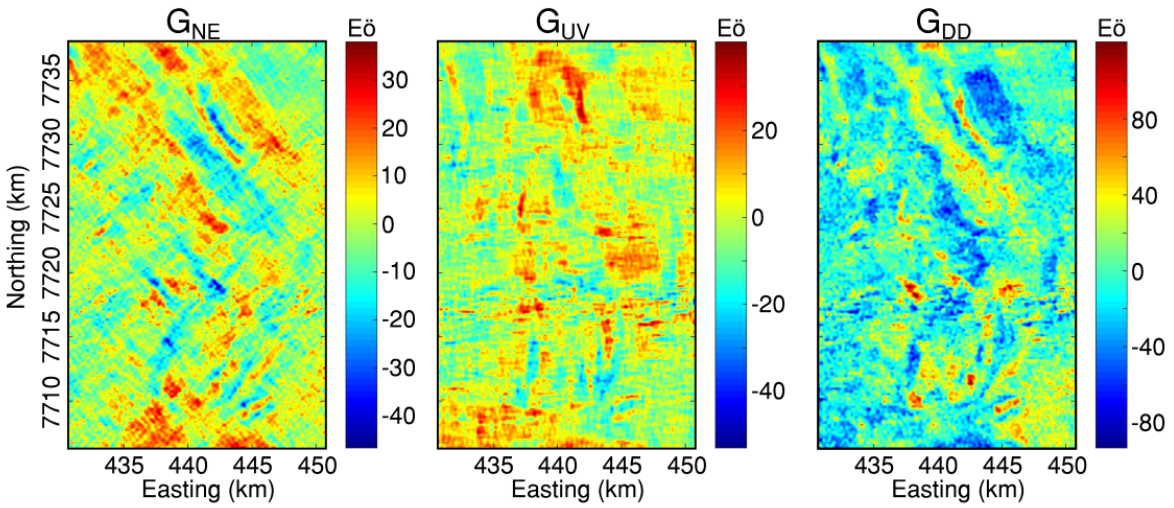

Figure 3.6: The constructed gradients based on the equivalent source technique provided by Fugro Geosciences.

Chapter 4

A New Noise Reduction Method for Airborne Gravity Gradient Data

Airborne Gravity gradient (AGG) measurements offer an increased resolution and accuracy compared to terrestrial measurements. But interpretation and processing of AGG data are often challenging as leveling errors and survey noise affect the data, and these effects are not easily recognized in the gradient components. We adopted the classic method of upward continuation in the noise reduction using the noise level estimates by the AGG system. By iteratively projecting the survey data to a lower level and upward continuing the data back to the survey height, parts of the high-frequency signal are suppressed. The filter, which is defined by this approach, is directly dependent on the noise level of the AGG data, the maximum number of iterations and the iterative step. We demonstrate the method by applying it to both synthetic data and real AGG data over Karasjok, Norway, and compare the results to the directional filtering method. The results show that the iterative filter can effectively reduce high-frequency noise in he data

4.1 Introduction

Since the first gravity gradiometer was introduced in 1886 by Hungarian physicist Baron von Eötvös, the technique of gravity gradiometry has been developed gradually (Zhdanov et al., 2004). Terrestrial gradiometer measurements have required much laborious field preparation, which made theme basically obsolete (Rummel and Gelderen, 1992; Jekeli, 2006). Since the 1970s, most gravity gradiometer instruments are based on a rotating accelerometer (Hofmeyer and Affleck, 1994). The technology of airborne gravity gradiometer (AGG) systems is the basis of commercial AGG system such FALCON airborne gravity gradiometer system (Lee, 2001).

There are two types of Lockheed Martin gravity gradiometers currently in operation: the 3D FTG (full tensor gravity gradiometer deployed in either a fixed-wing aircraft or a ship) and FALCON gradiometer (a partial tensor system with eight accelerometers and deployed in a fixed-wing or a helicopter). The FALCON gradiometer simultaneously measures four relative components, two for $\mathbf{G}_{\mathrm{NE}}$ and two for $\mathbf{G}_{\mathrm{UV}}$, where the $\mathbf{G}_{\mathrm{UV}}$ component is defined as $(\mathbf{G}_{\mathrm{NN}} - \mathbf{G}_{\mathrm{EE}})/2$, to increase the signal-to-noise ratio (Dransfield and Milkereit, 2007; DiFrancesco et al., 2009a) ($\mathbf{G}_{\mathrm{NE}}$: north-east gravity gradient component; $\mathbf{G}_{\mathrm{EE}}$: east-east gravity gradient component; $\mathbf{G}_{\mathrm{NN}}$: north-north gravity gradient component).

In recent years, an ever-increasing number of AGG surveys have been applied to mineral and hydrocarbon exploration (Barnes and Lumley, 2011). AGG data is best known for its sensitivity to near-surface sources and the ability to detect and image sources both in the vertical and lateral direction. But AGG data may be as well affected by systematic errors from the moving platform and a relatively high signal-to-noise ratio for the most AGG surveys compared to the traditional ground measurements. An average noise level is around 3-5 Eö (Eö = 0.1 mGal/km = 10^{-9} s^{-2}), which is considered acceptable for most surveys (Dransfield and Milkereit, 2007; Dransfield and Christensen, 2013). Conventional filters (e. g. Butterworth filter and cosine roll-off filter) in the frequency or spatial domain to a certain extent can improve the data, but an inappropriate choice of the cut-off wavelength may affect the signal content and the geophysical interpretation. Hence, filtering of high frequencies, which are sensitive to shallow and local structure, is a challenge in AGG data processing.

Different approaches to tackle this issue have been proposed. While et al. (2006) explained how to test the internal consistency of measured gravity gradients by using the power spectrum. This method is used to determine which part of the power spectrum is not source-related so that it can be filtered out. The simultaneous and joint filtering of all components of gravity gradient tensor components can preserve its internal consistency and reduce the overall noise level (Pajot et al., 2008; Sanchez et al., 2005). This method is reliant on a consistent reconstruction of all tensor components and a fixed relation between noise and frequency content, which may not reflect the measuring characteristics.

Another idea is to assume that noise and signal content in gravity gradient data have different wavelet coefficients across the scales of an orthonormal wavelet transform. Under this assumption, one can analyse the energy distribution to determine which part of the wavelet coefficients can be filtered out (Oliveira Lyrio et al., 2004). This method has

been successfully applied to synthetic data. Its application to real data is challenging as certain assumptions must be made (Pajot et al., 2008). Pilkington and Shamsipour (2014) proposed to modify and rotate a Gaussian filter along the estimated strike direction to filter out the noise and, to a large extent, preserve the geological signal. This method works well for simple geological settings, but it is not clear whether this holds for cases with more complex geology where the estimate of the strike direction might be distorted. Another way of reducing the noise from real gravity gradient data may use a strategy, in which the input data are iteratively fitted with their approximations while the differences are treated as noise. This method has been successfully applied to satellite gravity gradients from the Gravity Field and Steady-State Ocean Circulation Explorer (GOCE) mission (Bouman et al., 2015; Sebera et al., 2014) and is further developed here for an application to airborne gravity gradiometry data.

In this paper, we first provide a detailed derivation of the method and the explanation of all required parameters. Our method is tested on a synthetic simple example and also applied to a real-life AGG example of Karasjok in Norway. In both cases, we investigate the performance and effectiveness of our approach. Finally, the results are discussed and compared to the directional filtering method.

4.2 Methodology

Our method is based on the theory of the Landweber iteration for solving Fredholm integral equations of the first kind such as that used in downward continuation of the potential field (Landweber, 1951; Sebera et al., 2014; Zeng et al., 2013). In this section, we will show how Landweber iteration based downward continuation can be modified for noise reduction.

The classic upward-continuation integral equation of potential field in the planar approximation (Blakely, 1996), is given by

$$U_1(x,y,z_1) = \int_{-\infty}^{+\infty}\int_{-\infty}^{+\infty} \frac{h}{2\pi[(x-\xi)^2+(y-\mu)^2+h^2]^{\frac{3}{2}}} U_0(\xi,\mu,z_0)d\xi d\mu. \tag{4.1}$$

Here $K(x,y) = h/2\pi(x^2+y^2+h^2)^{\frac{3}{2}}$ is the convolution kernel, h is the continuation height equal to $h = z_1 - z_0$, where z_0 is a reference level, and x and y represent corresponding horizontal locations of a certain measurement along x-axis and y-axis, respectively.

Computing $U_1(x, y)$ from $U_0(x, y)$ is called the upward continuation, which presents a forward problem. Obtaining $U_0(x, y)$ from $U_1(x, y)$ is called the downward continuation, which is known to be an ill-conditioned inverse problem. In the next step, we turn to iterative approximation instead of the direct way to solve the above equation. We use $\otimes$ to denote the convolution operation so that the iterative approximation to the solution of the downward continuation has a general form such as (Zeng et al., 2013)

$$U_n = U_{n-1} + \alpha K^T \otimes (G - K \otimes U_{n-1}). \tag{4.2}$$

Here α is the iterative step which controls the speed of the iterations, and U_n is the nth approximation to the theoretical solution. If we assume that G_n stands for the nth approximation to the input data G and $G_n = K \otimes U_n$, the relation between the measured data and its nth approximation G_n becomes

$$G_n = G_{n-1} + \alpha K \otimes K^T \otimes (G - G_{n-1}). \tag{4.3}$$

Because the spatial convolution can be transfered into a simple multiplication in the wavenumber domain, all calculations are efficiently and easily conducted in the wavenumber domain. Therefore, Equation 4.3 in the wavenumber domain can be written as

$$\widetilde{G}_n = \widetilde{G}_{n-1} + \alpha \widetilde{K}^2 \cdot (\widetilde{G} - \widetilde{G}_{n-1}), \tag{4.4}$$

where the variables with $\sim$ denote their corresponding Fourier transform and the kernel function $\widetilde{K} = \exp(-h\sqrt{k_x^2 + k_y^2})$ (k_x and k_y are the wavenumbers along x-axis and y-axis, respectively).

Furthermore, assuming $G_0 = 0$ for a given n so $\widetilde{G}_n$ has the explicit form

$$\widetilde{G}_n = [1 - (1 - \alpha \widetilde{K}^2)^n]\widetilde{G}. \tag{4.5}$$

In accordance with Equation 4.5, we finally obtain the filter function; that is, $\Delta = [1 - (1 - \alpha \exp(-2h\sqrt{k_x^2 + k_y^2}))^n]$. To make this filter work, $\left\|1 - \alpha \widetilde{K}^2\right\| < 1$ must be met. Consequently, the iteration step should be $0 < \alpha < 2/\lambda_{max}^2$, where λ_{max} is the largest singular values of the kernel matrix $\widetilde{K}^2$. We depict a low-pass filter Δ in the wavenumber domain in Figure 4.1. We define the cut-off wavenumber where the response of the filter falls to 95% of the maximum value. Therefore, we let $\Delta = 0.95$ so that the cut-off wavenumber of the filter is given by

$$k = -\frac{1}{2h} \log \left[\frac{1}{x} (1 - \sqrt[n]{0.05}) \right], \tag{4.6}$$

which is a function of the iteration step, the number of conducted iterations and the difference in height.

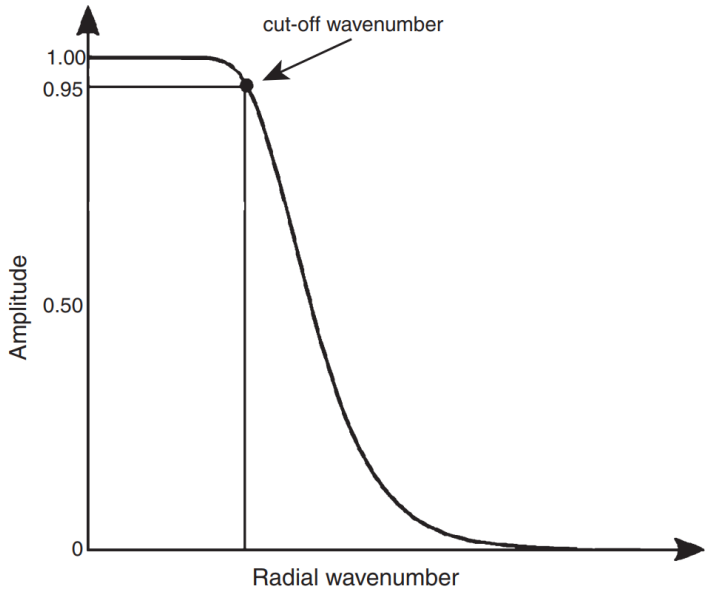

Figure 4.1: Diagram of the frequency response of the iterative low-pass filter, where the horizontal axis is the radial wavenumber and the the vertical axis is the amplitude.

Parameters As mentioned in the previous section, our iterative approach depends on a few parameters that have to be set with care. An appropriate choice of the iteration step is important because it is a prerequisite for the filter to function. A simple trick can facilitate this determination. By giving τ a small value equal to $\frac{1}{a}\frac{2}{\lambda_{max}^2}$, a new range of the iteration step $0 \leq \tau \leq \alpha \leq (2/\lambda_{max}^2 - \tau)$ becomes available, and then $\alpha \geq 2$. Furthermore, the closer the step is to $2/\lambda_{max}^2$, the faster the process is. Theoretically, $\alpha \to +\infty$, and then $\alpha = \frac{2}{\lambda_{max}^2}\left(1 - \frac{1}{a}\right) \to \frac{2}{\lambda_{max}^2}$. In practice, a cannot be infinite so that we conservatively set a equal to 50.

An acceptable result of this method is controlled by an appropriate choice of the height. According to Equation 4.3 and filter function $\Delta = [1 - (1 - \alpha \exp(-2h\sqrt{k_x^2 + k_y^2}))^n]$, the height can be any arbitrary distance, but the height is an important key to determining the shape and the behavior of this filter. For effective noise reduction, the height should always be not smaller than twice the grid interval.

To avoid unnecessary calculations and, in the meantime, to remove as much noise as possible, the stopping criterion should be slightly smaller than the estimated noise level

(in this paper, a standard deviation of the noise regarded as the noise level).

4.3 Synthetic example

To test our approach, the dataset was contaminated by Gaussian noise with zero mean and a standard deviation of 3 Eö as shown in Figure 4.2a. The maximum number of iterations was set to 1000, the height for noise reduction to 20 m that is equivalent to twice the grid spacing, and the threshold to 95% of the noise level because it is a pseudo-randomly behaving Gaussian noise. As seen from Figure 4.3, the process stopped after 157 iterations. Regarding the Equation 4.6 and the wavelength λ is equal to $2\pi/k$, we get a cut-off wavelength $\sim$ 170 m. From Figure 4.3, it is seen that the root mean square (RMS) of the residuals has started converging before being terminated automatically by the threshold. This means that the estimated noise level and noise suppressed by the iterative filter are comparable. Figure 4.4 shows that the original input data is dominantly affected by noise for wavelength smaller than 126 m. Before noise reduction, the power spectral density of the synthetic is flat. After the noise was reduced, the power spectral density of the filtered data in Figure 4.4 is dramatically decaying at higher frequencies.

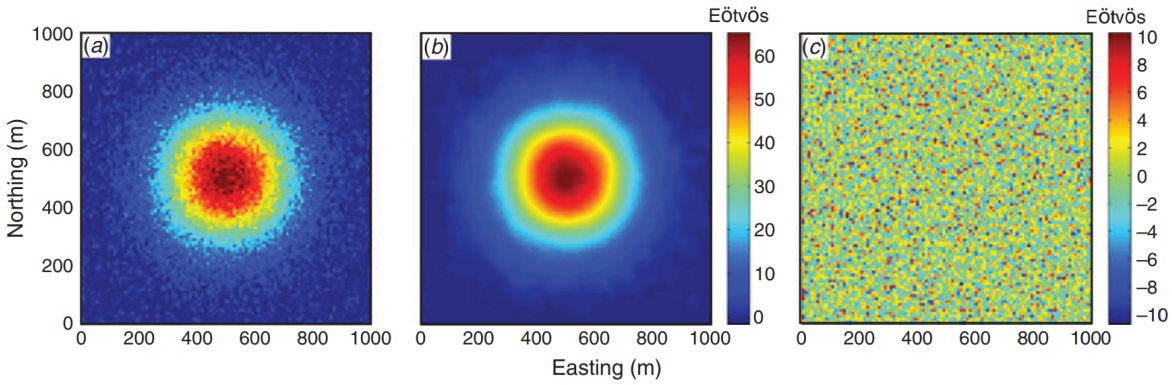

Figure 4.2: The synthetic vertical gravity gradient ($\mathbf{G}_{zz}$) data were calculated for a cube of dimensions 300 $\times$ 300 $\times$ 300 m with a density of 1000 kg/cm^3 at a depth of 1000 m. The grid spacing was chosen to be 10 m along both the x-axis and y-axis. (a) Data contaminated by Gaussian noise with zero mean and 3 Eö as standard deviation; (b) data after noise reduction; (c) differences between Figure 4.2a and Figure 4.2b.

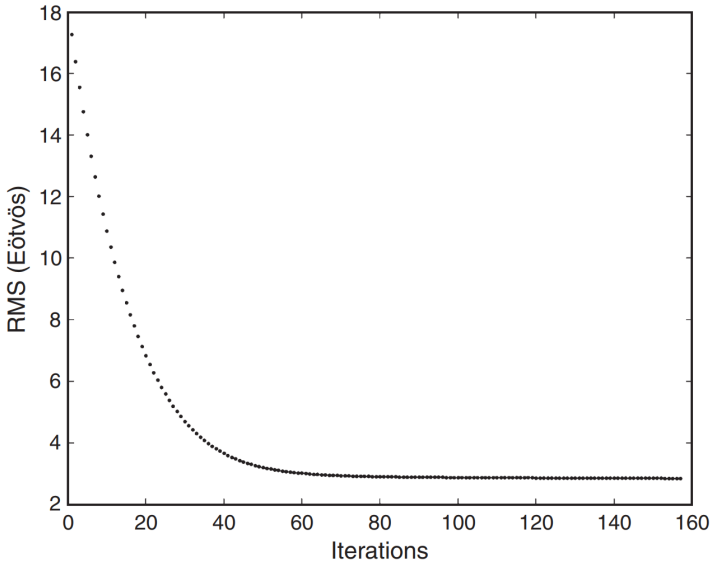

Figure 4.3: The RMS of the differences with respect to each iteration.

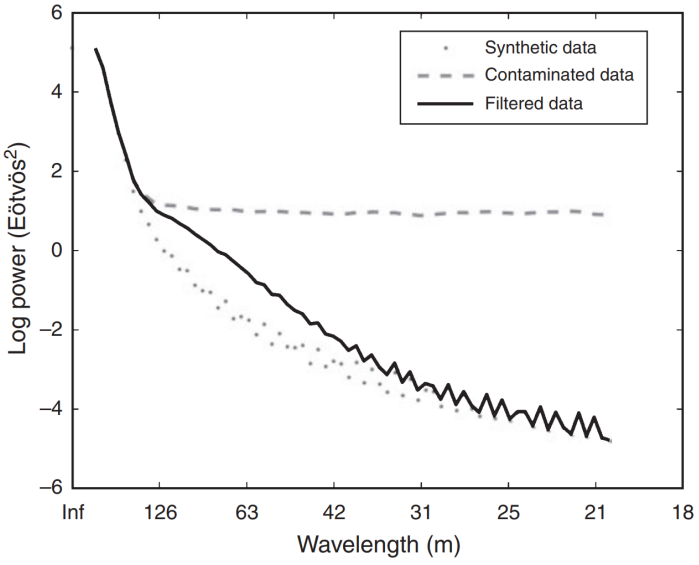

Figure 4.4: A comparison of the power spectrum derived from noise-free synthetic data, the contaminated data in Figure 4.2a and noise-reduced data in Figure 4.2b (note: the wiggles at the end of the power spectrum come from numerical rounding in the Fast Fourier transform. However, due to the small amplitudes, they do not impair the accuracy of the results).

4.4 Real example

We now test our approach on a real AGG dataset over the Karasjok Greenstone Belt in Norway. In the area, three main belt structures run roughly north to south with a bend in the central area (Skaar, 2014). The survey has an extension of 31.7 × 19.7 km and traverse lines were flown from west to east with additional five tie-lines perpendicular to the traverse lines. The average spacing of the traverse lines is 200 m, and the flight clearance is around 117 m with reference to the terrain. The grid spacing is 50 m along northing and easting direction. The data available to us were pre-processed, terrain corrected, leveled and low-pass filtered at a cut-off wavenumber of 0.18Hz (Fugro Data Processing Report, 2011). We use the $\mathbf{G}_{\mathrm{NE}}$ and $\mathbf{G}_{\mathrm{UV}}$ components in our analysis, as these most closely resemble the measured data and not constructed components of the gravity tensor. In the processing report (Fugro Data Processing Report, 2011), the estimated noise level for $\mathbf{G}_{\mathrm{NE}}$ and $\mathbf{G}_{\mathrm{UV}}$ components is 3.71 Eö and 3.58 Eö, respectively.

In applying our filter, the height was set to 100 m, equivalent to twice the sample interval, the maximum number of iterations was set to 1000 which is used to stop the iteration if the threshold at 90% of the noise level cannot be achieved. The results are presented in Figure 4.5 and Figure 4.6. The iterative process stopped after 239 iterations for the $\mathbf{G}_{\mathrm{NE}}$ and 266 iterations for the $\mathbf{G}_{\mathrm{UV}}$ component, corresponding to the cut-off wavelengths of 510 m and 489 m, respectively (Figure 4.6). Figure 4.5 shows that there is, in general, a low noise level as the data have already been low-pass filtered. The power spectra from the iterative filter (Figure 4.5d, j) indicates that the noise has been reduced significantly. On a regional scale, no noticeable trends or structures resembling the input data have been detected in Figure 4.5c, i. Figure 4.6 shows that the RMS of the residuals for $\mathbf{G}_{\mathrm{NE}}$ and $\mathbf{G}_{\mathrm{UV}}$ from the iterative filter is in agreement with the pre-defined noise levels.

To demonstrate the usefulness of the iterative filter, we compare our results to that of the directional filter. This Gaussian-based directional filter was introduced by Pilkington and Shamsipour (2014)

$$g(\theta, x, y) = \exp\left[-\frac{(x\cos\theta + y\sin\theta)^2}{\sigma_x^2} - \frac{(y\cos\theta - x\sin\theta)^2}{\sigma_y^2}\right], \tag{4.7}$$

where $g(\theta, x, y)$ is a filtered value at a point (x, y) from the data index origin $(0, 0)$. θ is the angle between the filter and x-axis. Variables σ_x and σ_y determine the width of the filter and hence the degree of smoothing.

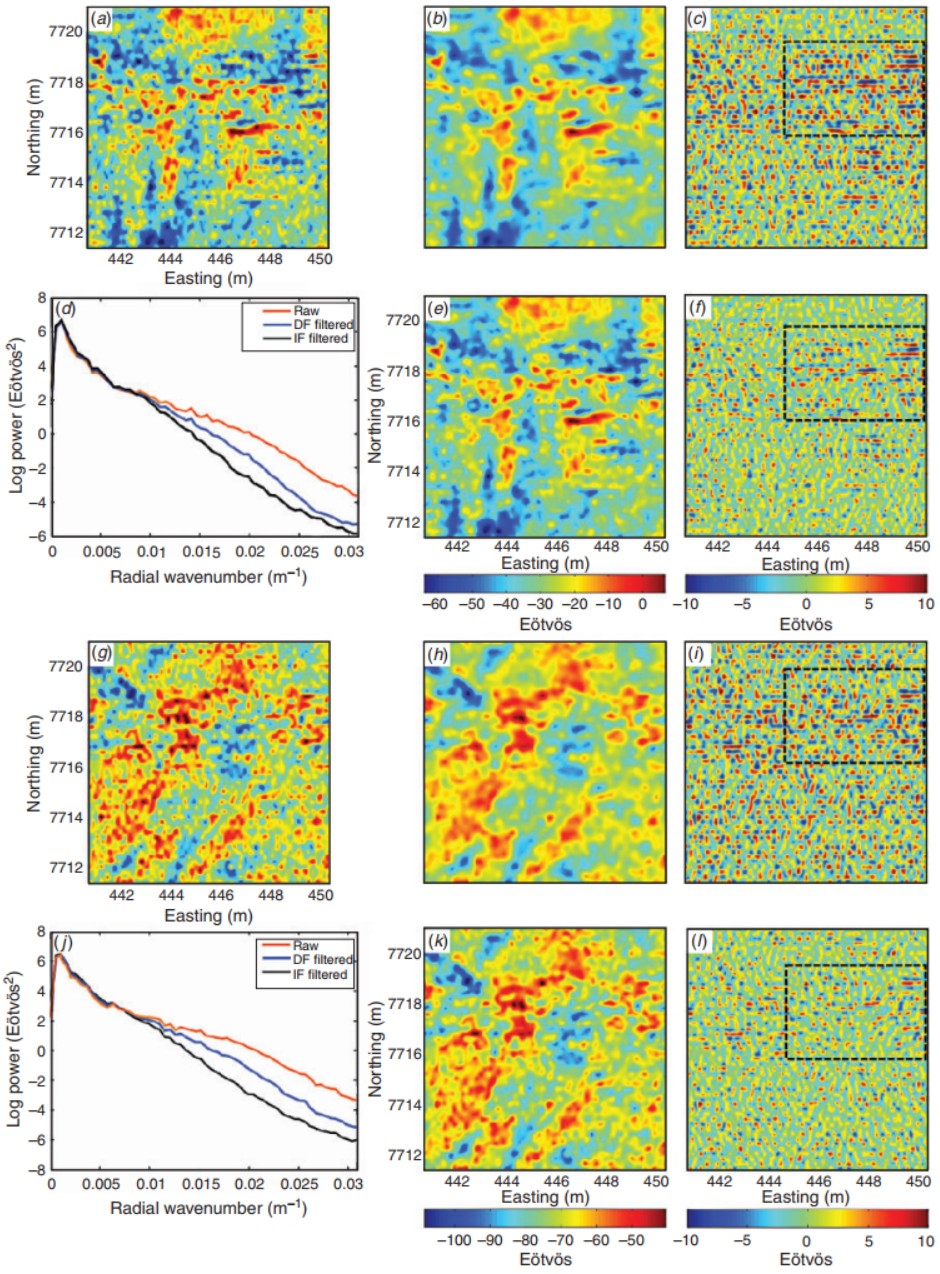

Figure 4.5: The upper panels from (a) to (f) display the $\mathbf{G}_{\mathrm{UV}}$ component for (a) raw input data, (b) filtered data derived from the iterative filter, (c) differences between Figure 4.5a and 4.5b, (d) the comparison of the power spectrum of raw data, iteratively filtered data and the directionally filtered data, (e) filtered data derived from the directional filter and (f) differences between Figure 4.5a and Figure 4.5e. The lower panels from (g) to (l) shows the $\mathbf{G}_{\mathrm{NE}}$ component for (g) raw input data, (h) filtered data derived from the iterative filter, (i) differences between Figure 4.5g and 4.5h, (j) the comparison of the power spectrum of raw data, iteratively filtered data and the directionally filtered data, (k) filtered data derived from the directional filter and (l) differences between Figure 4.5g and 4.5k.

For the directional filter, the data need to be first low-pass filtered to estimate the strike direction with little distortion. After several attempts at trial-and-error filtering, we decided to set the cut-off wavelength at 5 km for $\mathbf{G}_{\mathrm{NE}}$ and $\mathbf{G}_{\mathrm{UV}}$ because, with this cut-off wavelength, both the data and the strike-like trends are smooth. According to Pilkington and Shamsipour (2014), a reliable value for σ_x is half of the cut-off wavelength used in low-pass filtering in the first place. Furthermore, a ratio of σ_x/σ_y close to 1/4 seems useful for the process. Accordingly, we set σ_x and σ_y to 2.5 km and 10 km. Only a small part of the signal is considered as noise by the directional filter. This conclusion is also supported by 4.5d, j, where the power spectrum of $\mathbf{G}_{\mathrm{NE}}$ and $\mathbf{G}_{\mathrm{UV}}$ as well as their filtered counterparts are shown. The comparison of the signal and noise content (Figure 4.5) shows that the iterative filtering has scrubbed more of the high-frequency part in the signal. Both filters, to some degree, have removed some west-to-east oriented artifacts probably related to the flight line orientation outlined in the black box in Figure 4.5c, f, i, l.

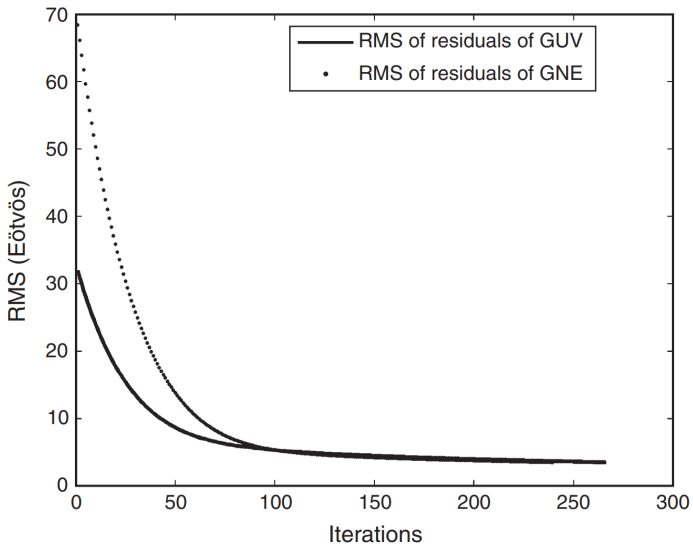

Figure 4.6: The RMS of residuals for $\mathbf{G}_{\mathrm{UV}}$ and $\mathbf{G}_{\mathrm{NE}}$ for iterative process.

4.5 Discussion

Our iterative noise reduction method is designed to specifically reduce the noise in AGG data with the help of the estimated noise level. According to Figure 4.5c, i, we can see that the iterative filter succeeded in suppressing some high-frequency content. In addition, some noticeable west-east strip artifacts have been revealed and removed by the filtering

as well. The flight line parallel to the orientation of the signal is an indication that these artifacts are small residual systematic errors from leveling.

As this method has an explicit expression, it can also be used as a traditional low-pass filter by a specific combination of the height h and the n in the equation $\Delta = [1 - (1 - \alpha e^{-2h\sqrt{k_x^2+k_y^2}})^n]$. In fact, the iteration step changes with height, which can be determined in a automatic way as stated in the previous section. In an iterative way, the selection of height can be critical because too large a height prevents the algorithm form reaching the threshold, so the height should be kept as small as possible, but no smaller than twice the grid interval.

The comparisons show us that the directional filter has suppressed less high-frequency content than the iterative filter. This may be due to the complex geological setting. The strike estimation may be affected by super-positioned sources, which can affect directional filtering and thus final geophysical interpretation. The directional filter highly depends on the user's experience. Consequently, the results from the directional filter may vary with a user. Nevertheless, the process of filtering along the strike direction is reasonable for preserving the geological signal compared to an ordinary low-pass filter that simply discards a signal above a certain cut-off wavenumber, but does not consider the available estimate of error threshold. The advantage of our iterative approach is that it considers the noise level of the measured data, which can be estimated from the measuring system (A and B measurements for FALCON data).

4.6 Conclusion

We presented an iterative filter, which successfully suppressed high-frequency noise with the help of the noise level provided by FALCON AGG system. With appropriately chosen parameters, the residual, interpreted as noise, does not resemble the input data. This method is sensitive to both high-frequency noises and some systematic errors in AGG data. Therefore, the iterative approach is a simple alternative to conventional filters and preferable to simple bandwidth filtering. But the method is not absolutely autonomous, and it also involves some subjective selection of parameters. However, the iterative filter can also be used in a semi-automatic way to reduce the noise with the help of *a priori* noise level from the original input data.

Chapter 5

A Fast Equivalent Source Technique

Airborne gravity gradiometry measures more than one components as conventional gravimetry does. However, processing of multi-component airborne gravity gradient data without corrupting their internal consistency is often challenging. Here, we adopt an equivalent source technique to process multiple gravity gradients jointly while keeping their consistency. Often the considerable computation cost of the equivalent source technique in the space domain hinders its application to gravity gradient data. With a combination of Gauss-FFT and the Landweber iteration, we developed an efficient way to compute equivalent sources for airborne gravity gradient data. This method can handle two components simultaneously. We first demonstrate its viability by applying this approach to a synthetic example. Afterward, we take advantage of the versatility of the method for joint reduction of measured airborne gravity gradient data for the Karasjok area, northern Norway. Our result is similar to the results obtained by Fugro Geosciences but with great efficiency. Subsequently, we show how to apply the method with a minor modification to estimate the apparent density of topography and discuss the result in comparison to in-situ density measurements.

5.1 Introduction

Gradiometry has been introduced into real applications for decades and its great practicality in prospecting for mineral deposits and even in petroleum exploration has been demonstrated (DiFrancesco et al., 2009a; Kass and Li, 2008). Airborne gravity gradiometry (AGG) measurements offer an increased resolution and accuracy compared to the ground gravimetry (Barnes et al., 2011). But processing AGG data is often challenging because of residuals due to routine corrections and instrumental noise (Dransfield and

Christensen, 2013). These influences cannot be easily recognized (Jirigalatu et al., 2016). In addition, the conventional way of individually handling gravity gradient components is prone to corrupting their internal consistency. As a consequence, a method capable of effectively processing multiple gravity gradient components and simultaneously preserving their internal consistency is highly desirable and yet remains challenging. FitzGerald and Holstein (2006) proposed a proprietary approach based on quaternion vector to preserve the internal consistency of gravity gradients in the course of data processing. Aside from this method, the widely used equivalent source method (Dampney, 1969) seems another appropriate alternative to preserve consistency.

But the high computation cost of the method limits its applicability (Pawlowski, 1994). To combat this difficulty, e. g., Xia et al. (1993) calculated the equivalent source for potential field data in the wavenumber domain using a fixed point iteration. Cooper (2002) introduced a fixed point iteration method to solve the linear system in equivalent source technique. That only requires forward calculations and thereby a computation and memory intensive method is converted to a computation intensive method only. Li and Oldenburg (2010) developed a method by using wavelet compression technique that reduces memory consumption for the computation with negligible loss of accuracy. Barnes and Lumley (2011) proposed a method based on quadtree representation, which allows users to process large datasets on personal computers. Oliveira Jr. et al. (2013) have developed a method by approximating the physical property of the equivalent source with a piecewise bivariate polynomial inside user-defined small windows, which is demonstrated to be able to effectively accelerate the computation. Siqueira et al. (2017) proposed a fast iterative equivalent source method based on the excess of mass and the positive correlation between the observed gravity data and the masses on the equivalent layer. This approach requires neither matrix multiplications nor solving linear systems. However, only a few of these approaches have been applied to single-component gravity measurements.

In this paper, we present an efficient way of computing equivalent sources for multi-component airborne gravity gradient data, using Gauss-FFT (Wu and Tian, 2014) and Landweber iteration (Landweber, 1951). Our method in principle can efficiently handle industry-standard two-component gravity gradient data simultaneously of FALCON AGG system. In this paper, we explain the method and demonstrate its applicability to a synthetic dataset and AGG survey data from the Karasjok area in Norway. For the

Karasjok area, we show as well how to apply the method in order to retrieve the apparent density of topography and compare this model with in-situ density measurements.

5.2 Methodology

5.2.1 Forward calculation

In this section, we explain the forward calculation in the wavenumber domain, which is the core of our method. Blakely (1996) states "*The forward calculation will form the foundation for more complex density sources, eventually leading to a wide variety of applications, including forward and inverse calculations.*" In the following discussion, F and F^{-1} stand for forward Fourier transform and inverse Fourier transform, respectively. The dot multiplication "$\cdot$" denotes element-wise multiplication otherwise the matrix multiplication. The Fourier transform of the gravitational potential observed on a horizontal plane at z caused by a point mass located underneath the place at z_0 can be written as

$$F\left[U\right] = 2\pi\gamma m \frac{e^{k(z-z_0)}}{k}, z < z_0, \tag{5.1}$$

where $k = \sqrt{k_x^2 + k_y^2}$ (k_x and k_y are wave numbers in the x and y directions, respectively) and m is the mass. In the paper, γ is the gravitational constant. Considering a center point Q of a prism at $(0, 0, z_0)$ with dimensions of $pw \times pl \times ph$, its potential on a horizontal plane z can be obtained by integral of the kernel shown in Equation 5.1 along x-axis, y-axis and z-axis inside the prism (Zhao et al., 2018). The potential caused by this prism can be written as

$$F\left[U\right] = 2\pi\gamma \frac{e^{k\cdot z}}{k^2} \frac{2\sin(0.5pwk_x)}{k_x} \frac{2\sin(0.5plk_y)}{k_y} \left(e^{-kz_t} - e^{-kz_b}\right) F\left[\rho\right]. \tag{5.2}$$

However, traverse lines of an airborne gravity gradiometry are normally draped to topography, leading to an uneven observation surface. That limits the applicability of Fourier transformation. To overcome this limitation, we apply a Taylor's series to approximate a rugged observation surface in Equation 5.2 (Xia et al., 1993). As the distance between z and z_0 is $d = z - z_0$, the distance d can be also expressed by $d = d_0 + \Delta d$, where d_0 is the mean of d and Δd is the difference between d and Δd, illustrated in Figure 5.1. Let $Cx = \frac{2\sin(0.5\cdot pw\cdot k_x)}{k_x}$ and $Cy = \frac{2\sin(0.5\cdot pl\cdot k_y)}{k_y}$, Equation 5.2 can be expressed as

$$U = 2\pi\gamma Cx \cdot Cy \cdot \sum_{t=0}^{\infty} k^n \cdot \frac{F[\Delta d^n]}{t!} \frac{e^{k\cdot d_0}}{k^2} \left[e^{-k(z_0 - 0.5\cdot ph)} - e^{-k(z_0 + 0.5\cdot ph)}\right] F\left[\rho\right] \tag{5.3}$$

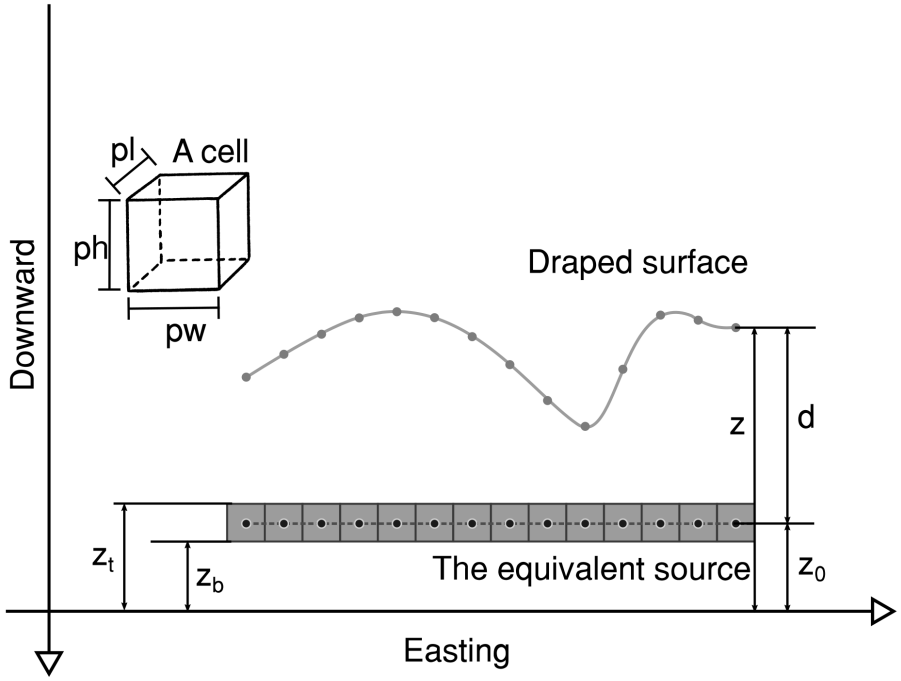

Figure 5.1: A 1D schematic representation of the draped observation surface and the equivalent source layer.

Moreover, according to differentiation theorem Blakely, 1996, the gravity gradient tensor U_{uv}, where $u, v \in [x, y, z]$, can be expressed as

$$F\left[U_{uv}\right] = \begin{pmatrix} -k_x^2 & -k_x k_y & ik_x k \\ & -k_y^2 & ik_y k \\ & & k^2 \end{pmatrix} \cdot F\left[U\right]. \tag{5.4}$$

5.2.2 Integrating Gauss-FFT into forward calculation

Instead of using the standard fast Fourier transform (FFT), we use Gauss-FFT introduced by Wu and Tian (2014). Gauss-FFT is able to significantly improve the numerical accuracy of forward calculations of potential fields in the wavenumber domain. The theory involves an application of the shift properties of Fourier transform (Blakely, 1996) and Gauss-Legendre quadrature rule.

If we have N datum points sampled at $s = m\Delta s$, where Δs is the spatial interval and $m \in [-\frac{N}{2}, \frac{N}{2} - 1]$. The associated wavenumber should be $\omega = n\Delta\omega$, where $\Delta\omega$ is the frequency interval in the wavenumber domain and $n \in [-\frac{N}{2}, \frac{N}{2} - 1]$, accordingly. So the

inverse discrete Fourier transform is given by

$$g\left(m\Delta s\right)=F^{-1}\left[G\left(n\Delta\omega\right)\right], \tag{5.5}$$

where $\Delta\omega=\frac{1}{N\cdot\Delta s}$ and G is equivalent to forward calculation in the wavenumber domain. We impose a small positive perturbation $\delta\in[0,1]$ to shift the wavenumber, and then the shifted wavenumber is $\omega_\delta=\omega+\delta\Delta\omega, n\in[-\frac{N}{2},\frac{N}{2}-1]$. Equation 5.5 becomes

$$g_\delta\left(m\Delta s\right)=F^{-1}\left[G\left(\omega+\delta\Delta\omega\right)\right]. \tag{5.6}$$

For simplicity, we define $G_\delta=G\left(\omega+\delta\Delta\omega\right)$ as the spectrum of the newly shifted wavenumber.

$$g_\delta=\mathrm{Re}\left\{e^{2\pi j\frac{m\delta}{N}}\cdot F^{-1}\left[G_\delta\right]\right\},\quad\text{where}\quad j^2=-1. \tag{5.7}$$

It's worth noting that as the wavenumber has been shifted, the spectrum of density source has to be shifted by the same amount. Assuming a Fourier transform pair for density to be $F[\rho]=P$, the shifted density spectrum density P_δ is given by

$$P_\delta=F\left[\rho\cdot e^{-2\pi j\frac{\delta m}{N}}\right]. \tag{5.8}$$

If we let K be a forward operator in the wavenumber domain, its shifted counterpart is marked as K_δ. Thus, the whole forward calculation with shifted wavenumber can be expressed by

$$G_\delta=K_\delta\cdot P_\delta. \tag{5.9}$$

In general, the Gauss-FFT is a sum of results with different shift parameters δ_i as

$$g=\sum_{i=1}^{M}w_i\mathrm{Re}\left(g_{\delta i}\right), \tag{5.10}$$

where δ_i and w_i are the ith node and ith weight of even-node Gaussian-Legendre quadrature on the interval $[0,1]$. In Equation 5.10 can only be even numbers. Empirically, M equals to 6 should be sufficient in most cases. Eventually, the forward calculation supported by Gauss-FFT in 1D scenario can be summarized as

$$g=\sum_{i=1}^{M}w_i\mathrm{Re}\left\{e^{2\pi j\frac{\delta_i m}{N}}\cdot F^{-1}[K_{\delta i}\cdot P_{\delta i}]\right\}, \tag{5.11}$$

For a 2D case, the formula can be easily obtained by applying the same rule.

5.2.3 Inversion

Another important part of equivalent source technique is to solve the linear equation:

$$\mathbf{A}\mathbf{x} = \mathbf{d}. \tag{5.12}$$

When solving Equation 5.12 using Landweber iteration (Landweber, 1951), we have the lth iterative form of Landweber iteration

$$\Delta\mathbf{x}_l = \mathbf{d} - \mathbf{A}\mathbf{x}_l, \tag{5.13}$$

$$\mathbf{x}_{l+1} = \mathbf{x}_l + \alpha\mathbf{A}^*\Delta\mathbf{x}_l. \tag{5.14}$$

where the relaxation factor α satisfies $0 < \alpha < 2/\sigma_{max}^2$ and σ_{max} is the largest singular value of $\mathbf{A}$. The asterisk denotes transposition. As for two components $\mathbf{d}_1, \mathbf{d}_2$ with corresponding forward calculation kernels $\mathbf{A}_1, \mathbf{A}_2$, we simply define the sum multiplied by the same relaxation factor which should be the smallest relaxation factor for all components, that is, $\alpha_{min} = \mathrm{Min}(\alpha_1, \alpha_2)$.

$$\mathbf{x}_{l+1} = \mathbf{x}_l + \alpha_{min} \cdot \left(\mathbf{A}_1^*\Delta\mathbf{x}_{1l} + \mathbf{A}_2^*\Delta\mathbf{x}_{2l}\right), \tag{5.15}$$

5.2.4 Edge effects

Edge effects are inevitable due to the limited extent of measured data. Therefore, one has to extend the calculation area by extrapolation or padding. However, gravity gradient components are internally related, which cannot be properly resolved by conventional extrapolation methods (Briggs, 1974). As a solution, we use a mask matrix used for deconvolution of astronomical images (Vio et al., 2005). This mask matrix $\mathbf{M}$ can be easily integrated into Landweber iteration. The mask matrix has entries set to 1 in correspondence to the pixels containing the original data and 0 otherwise. This simple manipulation can, to a large degree, reduce the edge effects without increasing the computation complexity as the whole process is based on element-wise multiplication. This mask matrix allows our algorithm only to evaluate data in correspondence to the pixels in the original data $\mathbf{d}$. Conventionally, we would have to extrapolate different gravity gradient components and maintain their internal consistency. Using the mask matrix, it does not require that the extrapolated data for different gravity gradients are internally consistent. So padded data for multiple gravity gradient components can be zero at the same time. Furthermore, the extra calculation area as a result of the zero-padding can

improve the accuracy of forward calculation in the wavenumber domain even with few Gaussian nodes M. As a result, the new recursive Landweber solver has become

$$\Delta \mathbf{x}_l = \mathbf{d} - \mathbf{M} \cdot \mathbf{A}\mathbf{x}_l. \tag{5.16}$$

5.2.5 Implementation

By examining Equation 5.13 and Equation 5.14 closely, we notice that for every iteration, the forward calculation, i. e., $\mathbf{A}\mathbf{x}_l$ and $\mathbf{A}^*\Delta\mathbf{x}_l$ are implemented twice. Therefore, the inversion part can be easily programmed by just simply recycling the forward calculation codes. The resultant data should be sure of being transformed into the space domain. As for multi-component datasets, the inversion evaluates Equation 5.16 for each component first and then updates Equation 5.15 component by component in the space domain until the algorithm reaches the maximum iteration. However, due to the difficulty of expressing the Jacobian matrix $\mathbf{A}$ explicitly, the mentioned approach of determining the relaxation factor is not used here. The relaxation factor has to be carefully selected by trial-and-error.

5.3 Synthetic Example

First, we apply our method to a synthetic dataset to demonstrate its viability. For the purpose, we use the 3D random field method as proposed by Tontini et al. (2009). The synthetic signal induced by the density distribution simulated by the random 3D field is relatively more similar to a real scenario than a superimposed model with only a few simple sources. To generate the 3D random field, We start off with 3D zero-mean Gaussian random data w with a standard deviation of 2 g/cm^3, and then transform the random data into the wavenumber domain denoted by W and its conjugate matrix is represented by $\overline{W}$. Then we can calculate the following formula $D = \overline{W} \cdot \left(k_x^2 + k_y^2 + k_z^2\right)^{-\frac{\beta}{2}}$, where k_x, k_y and k_z are wavenumber along x-, y- and z-axis, respectively. The scaling parameter β is equal to 6. The final step is to transform the newly computed data D back into the space domain. The 3D random field has been confined to a half-space volume with dimensions as 5000 m $\times$ 5000 m $\times$ 5000 m to serve as a real subsurface model as shown in Figure 5.2 and the other top half-space is the observation domain. The respective grid interval along North, East, and Down-axis is 50 m, 50 m, and 50 m.

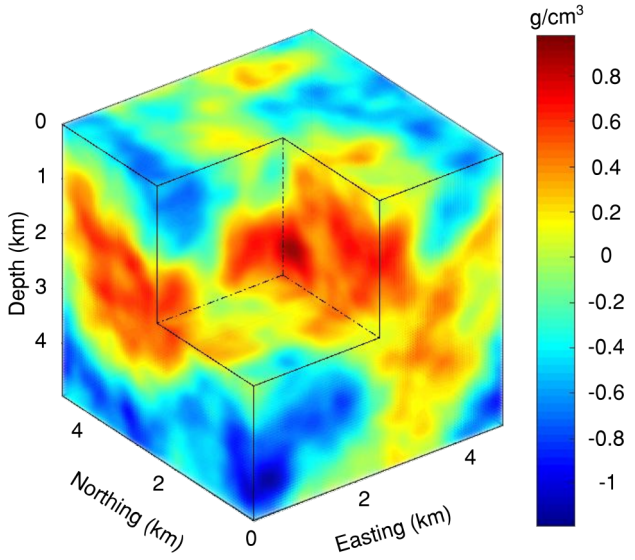

Figure 5.2: The synthetic 3D density contrasts.

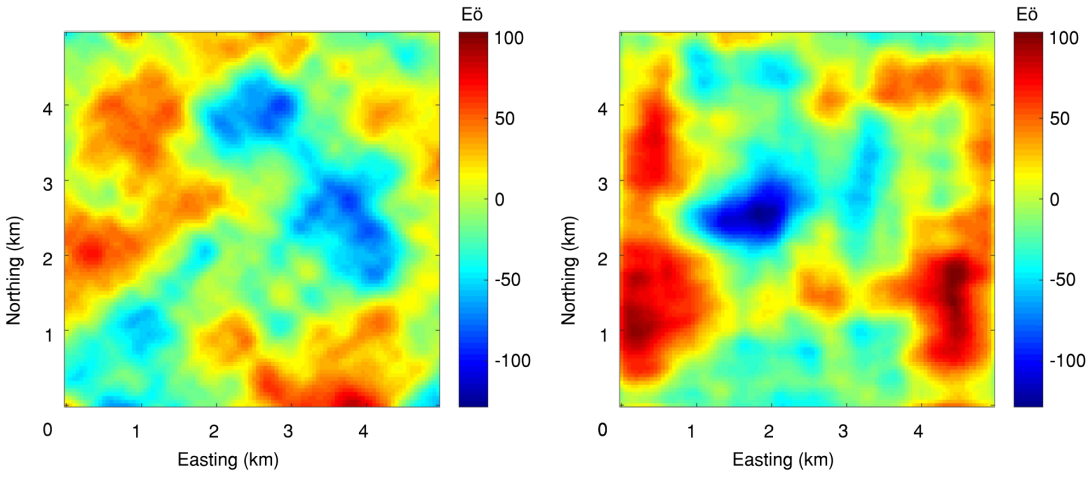

(a) (b)

Figure 5.3: The two synthetic gravity gradients resulting from the synthetic density.(a) $\mathbf{G}_{\mathrm{NE}}$, (b) $\mathbf{G}_{\mathrm{UV}}$.

We simulate the two-component gradient data as measured by FALCON airborne gravity gradiometer of CGG. The system has been used for various prospecting purposes (Dransfield and Milkereit, 2007).The system measures two curvature components, namely $\mathbf{G}_{\mathrm{NE}}$ (the North-East component of the gravity gradients) and $\mathbf{G}_{\mathrm{UV}}$ (half of the difference between the East-East component and the North-North component of the gravity gradients) (Lee, 2001). The $\mathbf{G}_{\mathrm{NE}}$ and $\mathbf{G}_{\mathrm{UV}}$ components from the synthetic 3D model are calculated at a height of 100 m above the surface, approximated by a stack of superimposed prisms in the space domain (Li and Chouteau, 1998; Forsberg, 1984), (Figure 5.3a and Figure 5.3b). In most cases, terrain correction of gravity gradient data is done by Fugro Geosciences. As a consequence, terrain effects are not considered in the synthetic scenario.

Among other problems we may face while retrieving equivalent source, edge effects as a consequence of data due to mass outside the survey area need to be considered. Consequently, we compile different results using various padding schemes in Table 5.1. For the following four cases, the respective parameters for the relaxation factor, iteration as well as Gaussian nodes are set 0.001, 100 and 4, respectively. These parameters are selected by trial-and-error. One rule of thumb is first to select the number of Gaussian nodes for Gauss-FFT (Practically, 2 or 4 is generally enough for our method) and then to try different relaxation factors.

Case	Padding	Mask	Area	Method	Domain	Duration (s)
1	No	No	00%	None	Space	383
2	Yes	No	20%	Only zeros	Wavenumber	9
3	Yes	No	20%	Consistent	Wavenumber	9
4	Yes	Yes	20%	Only zeros	Wavenumber	9

Table 5.1: Different set-ups to reduce edge effects. Only zeros indicates that for both, only zero values are added to extend the calculation areas. Consistent means we use forward calculation to extend the area for both input gradient components so that the internal consistency of the data is kept. Area defines how much the survey area is extended. Duration means calculation time.

Some edge effects are clearly seen in Figure 5.4a and Figure 5.5a. This is not unexpected, even with calculations in the space domain and this obviously will affect the

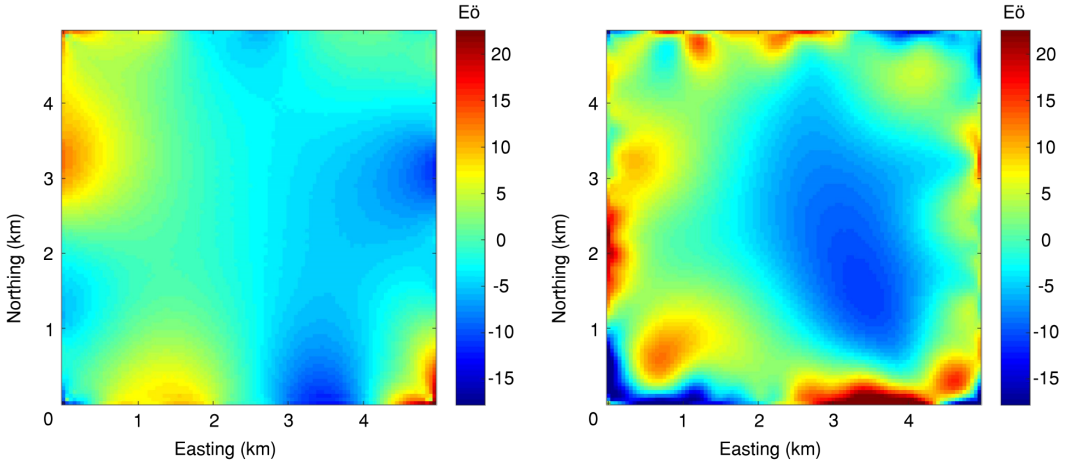

(a) (b)

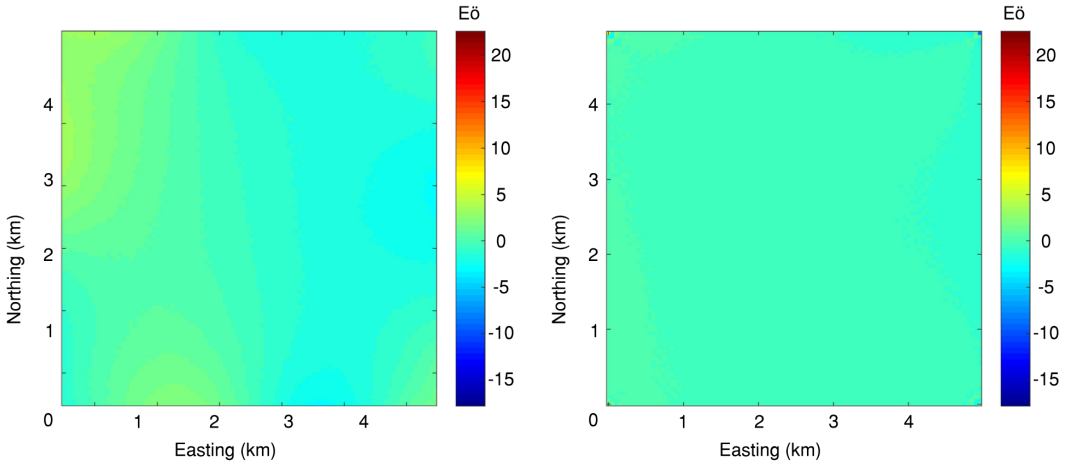

(c) (d)

Figure 5.4: The residual error maps between the input $\mathbf{G}_{\mathrm{NE}}$ and the predicted $\mathbf{G}_{\mathrm{NE}}$ with the different edge reduction approaches, (a) without padding and without the mask matrix, (b) with zero-padding extra 20% calculation area without the mask matrix, (c) with padding extra 20% calculation area but internal consistency kept and without the mask matrix, (d) with zero-padding extra 20% calculation area and the mask matrix.

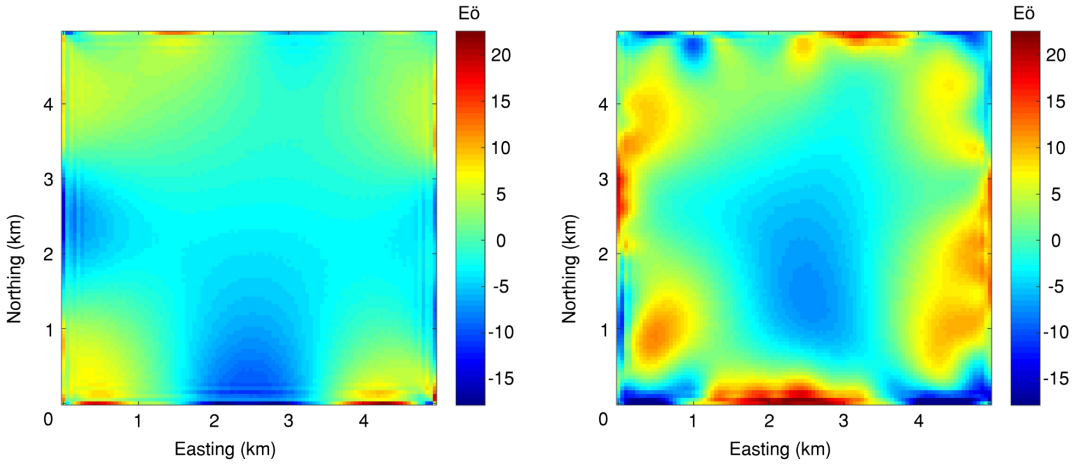

(a) (b)

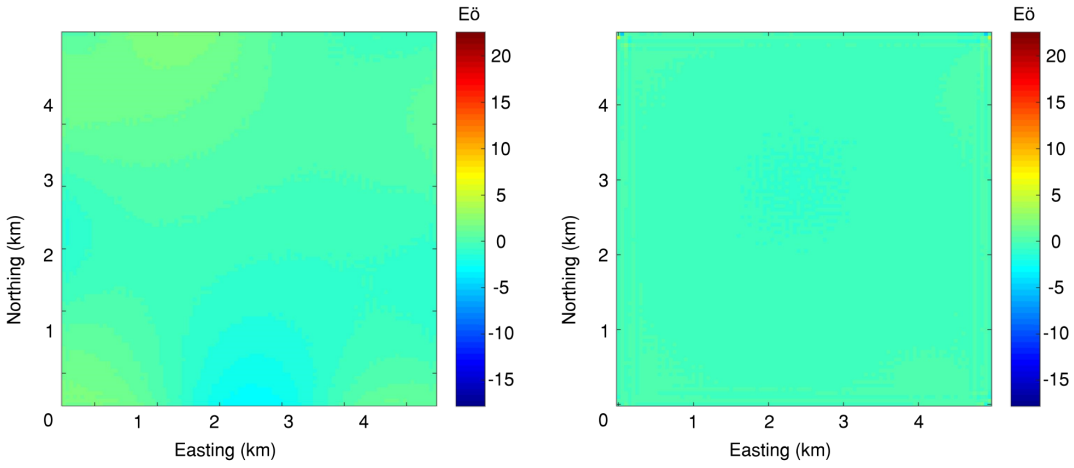

(c) (d)

Figure 5.5: The residual error maps between the input $\mathbf{G}_{\mathrm{UV}}$ and the predicted $\mathbf{G}_{\mathrm{UV}}$ with the different edge reduction approaches, (a) without padding and without the mask matrix, (b) with zero-padding extra 20% calculation area without the mask matrix, (c) with padding extra 20% calculation area but internal consistency kept and without the mask matrix, (d) with zero-padding extra 20% calculation area and the mask matrix.

wavenumber domain as well. The edge effects also lead to some misfits of a part of long wavelength content. In principle, the second test will not work properly. Due to the discontinuity at the edges and the incompatibility with the original data, the severe edge effects shown in Figure 5.4b and Figure 5.5b are not surprising. In the third approach, the significant improvement demonstrated in Figure 5.4c and Figure 5.5c is due to the preserved the internal consistency by forward calculating the missing data of the extended calculation area from the synthetic model. However, in practice, it is not easy to extend the gravity gradient data continuously and preserve consistency of the components. The fourth approach exhibited in Figure 5.4d and Figure 5.5d gives even better results even though some oscillations around the edges can still be detected. The fourth approach arguably provides improved results, at least with the chosen near-source distance of our observations. In sum, the fourth approach appears to be a good compromise for real applications.

5.4 Case Example

We now test our method using a real dataset. The first step is to reduce noise jointly from measured gravity gradient data over Karasjok, Norway based on the inherent ability to deal with multi-component gravity gradient datasets and then examine whether our result is comparable with industrial output provided by Fugro Geosciences. The second application is to estimate the apparent density of the topography with minor modification to the forward calculation of the method.

5.4.1 Background

The Karasjok Greenstone Belt is regarded to have a potential for mineral prospection as it hosts both ultramafic intrusions, komatiites, and widespread gabbroic intrusions (Nillsson and Often, 2006). The Greenstone Belt has a North-South trend with a length of about 160 km, and ranges in width from 20 to 40 km (Figure 5.6). To the west, it is non-conformably overlying and partly thrust over the granitic basement rocks of the Archaean Jergul Gneiss Complex (JGC), which provides a base for the Karasjok Greenstone Belt (Krill, 1985). To the east, it is bounded by the over-thrusted Tanaelv Migmatite Complex (TMC), which is a narrow belt of high-grade metamorphic rocks (Often, 1985).

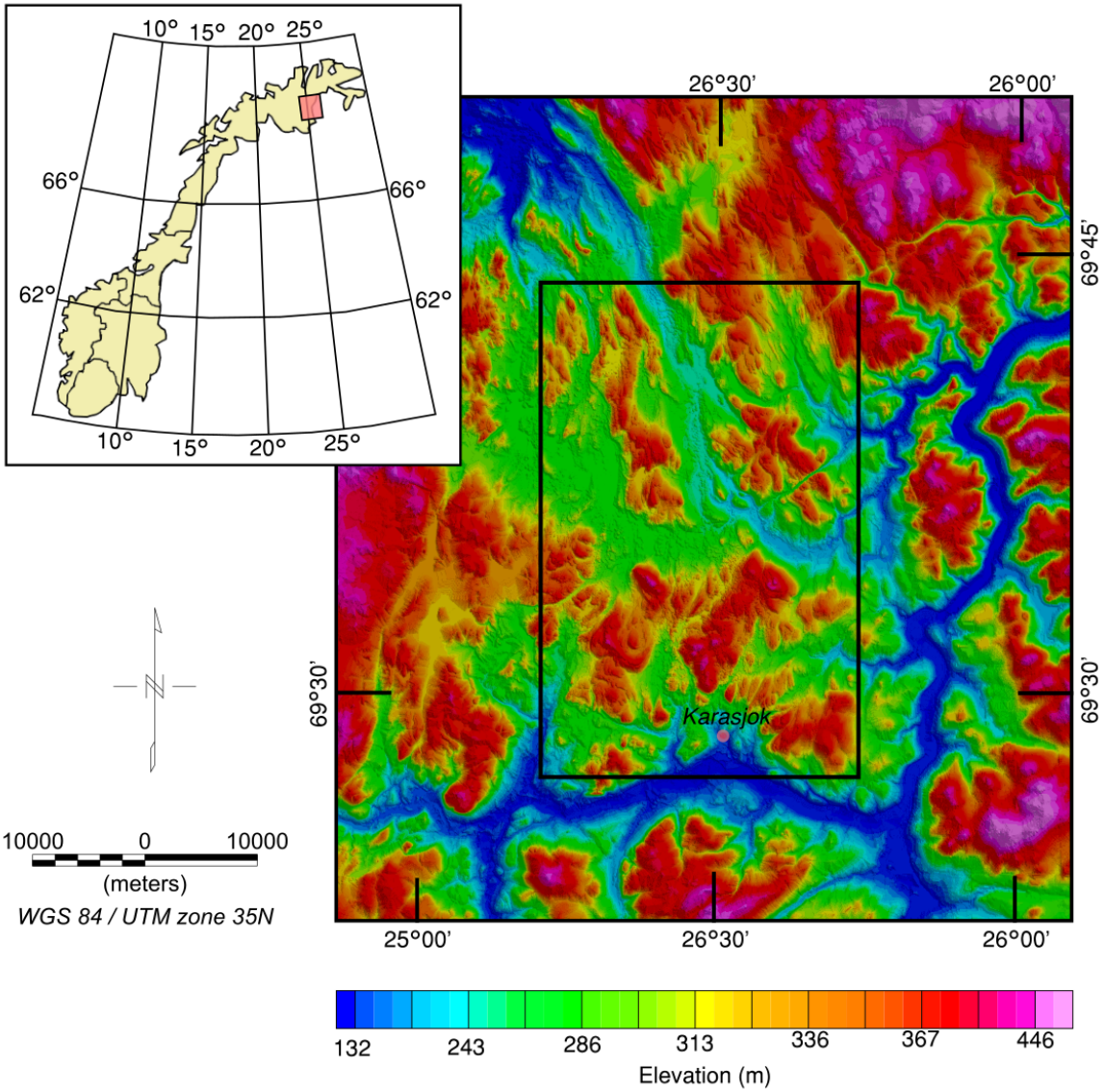

Figure 5.6: A regional digital elevation map of the northern part of the Finnmarksvidda and the survey area is outlined with a black rectangle.

To further the understanding of the internal structure of the Greenstone Belt, an airborne gravity gradiometry survey was flown in 2011 with a FALCON™ AGG system. The survey covers an area of 31.7 km × 19.7 km of the northern part of the Karasjok Greenstone belt outlined with a black rectangle in Figure 5.6. The average ground clearance is 117 m and the survey lines in East-West with 200 m line spacing. The measured $\mathbf{G}_{\mathrm{NE}}$ and $\mathbf{G}_{\mathrm{UV}}$ shown in Figure 5.7a and Figure 5.7d were routinely low-pass filtered at 0.18Hz, terrain-corrected, and tie-line leveled by Fugro Geosciences (Fugro Data Processing Report, 2011).

5.4.2 Joint noise reduction

Joint noise reduction means that different measured components from gravity gradiometry should theoretically make an equal contribution to determining and reducing existing noise. The concept of equivalent source technique is well-suited for this purpose because gravity gradients are as a result of horizontal and vertical density variation. Therefore, we only need to jointly translate the multi-component gravity gradients into a common density variation and leave the algorithm naturally to reject incompatible content. Because the FALCON AGG system measures two gravity gradients, $\mathbf{G}_{\mathrm{NE}}$ and $\mathbf{G}_{\mathrm{UV}}$, the full tensor gravity (FTG) is constructed from the two main approaches currently in use, such as the Fourier transform approach and the equivalent source method (Barnes and Lumley, 2011; Nabighian et al., 2005). Reducing noise in the measured $\mathbf{G}_{\mathrm{NE}}$ and $\mathbf{G}_{\mathrm{UV}}$ is critical. We use the measured $\mathbf{G}_{\mathrm{NE}}$ and $\mathbf{G}_{\mathrm{UV}}$ component.

We invert the measured $\mathbf{G}_{\mathrm{NE}}$ and $\mathbf{G}_{\mathrm{UV}}$ component for the equivalent source density. Each of the components is gridded into equally spaced data with 633×401 points. For the calculation, 20% of the extra calculation area is appended to the original inputs. We use a flat equivalent source layer with the same size at a height of 100 m above the sea level. The draped surface as shown in Figure 5.8a is a 2D representation of the traverse lines. The relaxation parameter, iteration number and the number of Gaussian nodes M are defined as 0.005, 100 and 2, respectively. The relaxation factor is determined by trial-and-error. We run this method on a desktop with 16 Gigabytes RAM and Intel Core i7-4790 four-core processor as well as 64-bit Windows Enterprise. The process only takes 762 s.

The predicted $\mathbf{G}_{\mathrm{NE}}$ and $\mathbf{G}_{\mathrm{UV}}$ are shown in Figure 5.7b and Figure 5.7e. Clearly, the residuals shown in Figure 5.7c and Figure 5.7f reveal some patterns mimicking the flight lines and are patchy otherwise. The estimated noise-reduced components are visually smoother for the noise is jointly reduced. We compare our results with those of Fugro Geosciences on the drape surface depicted in Figure 5.8b. Figure 5.9a and Figure 5.9d show the comparison of $\mathbf{G}_{\mathrm{NE}}$ and $\mathbf{G}_{\mathrm{UV}}$, respectively. The comparison shows that our method delivers similar results as Fugro Geosciences which represents the industry standard. It's worth noting that because we do not have access to how exactly Fugro Geosciences implemented their equivalent source algorithm, it is difficult to assuredly explain where the discrepancy comes from. However, according to the patterns displayed

in Figure 5.9c and Figure 5.9f, there is a possibility that the discrepancy may be induced by leveling residuals.

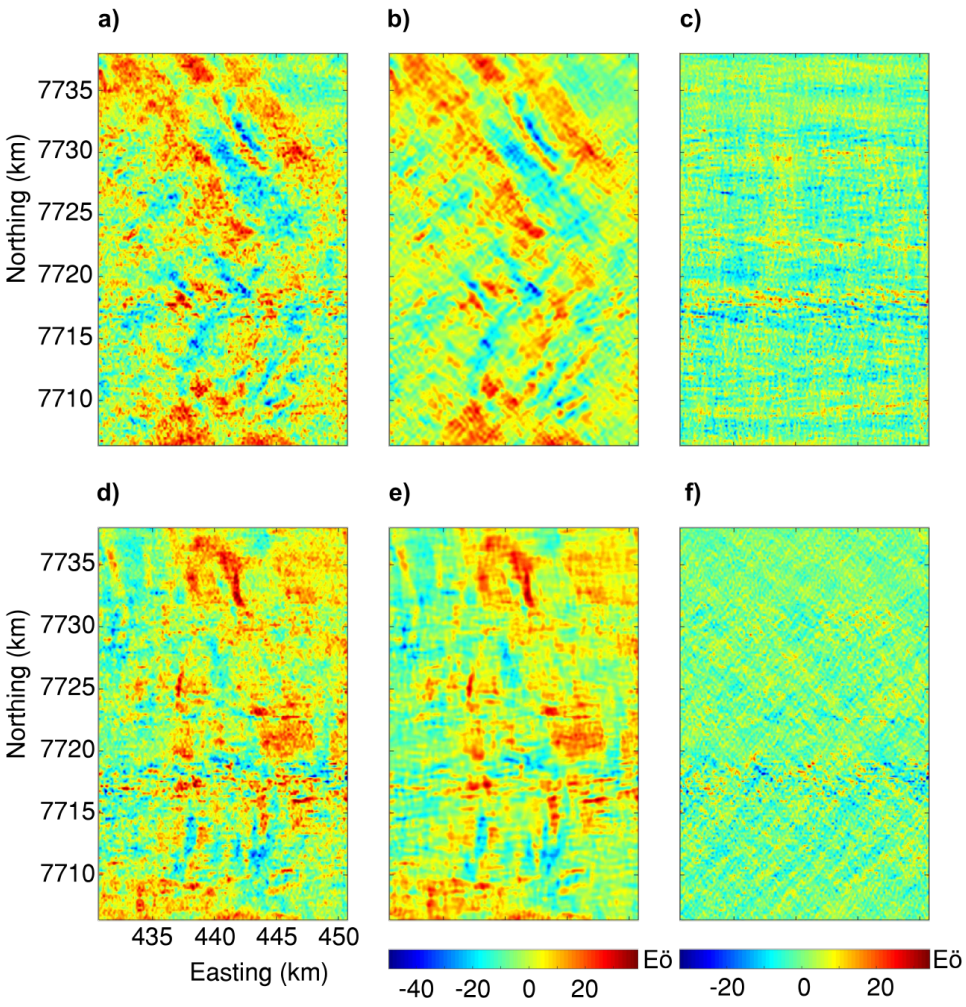

Figure 5.7: Comparisons between the measured $\mathbf{G}_{\mathrm{NE}}$ (a) and $\mathbf{G}_{\mathrm{UV}}$ (d) and the corresponding predicted $\mathbf{G}_{\mathrm{NE}}$ (b) and $\mathbf{G}_{\mathrm{UV}}$ (e) derived from the our method accompanied by their respective differences (c) and (f).

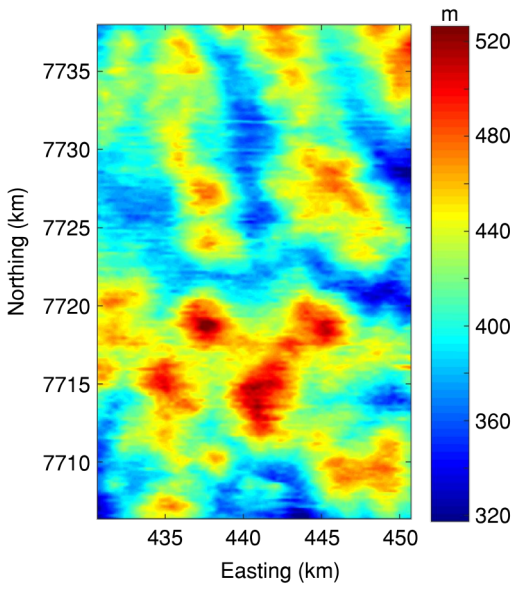

(a)

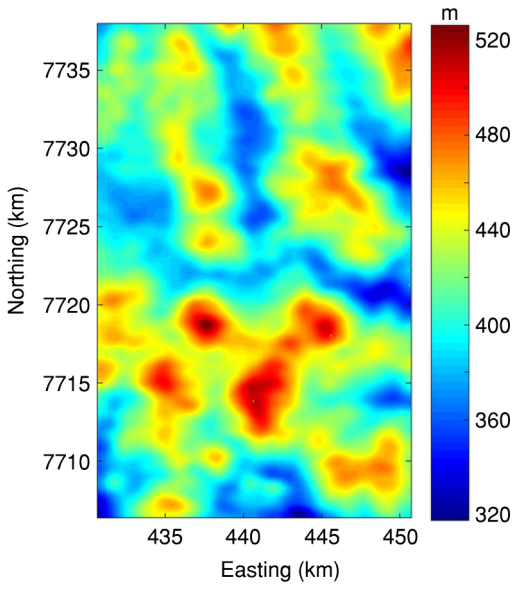

(b)

Figure 5.8: The draped surface (a) for the joint noise reduction and the smoothed draped surface (b) (provided by Fugro Geosciences) for the comparison with the constructed data by Fugro Geosciences

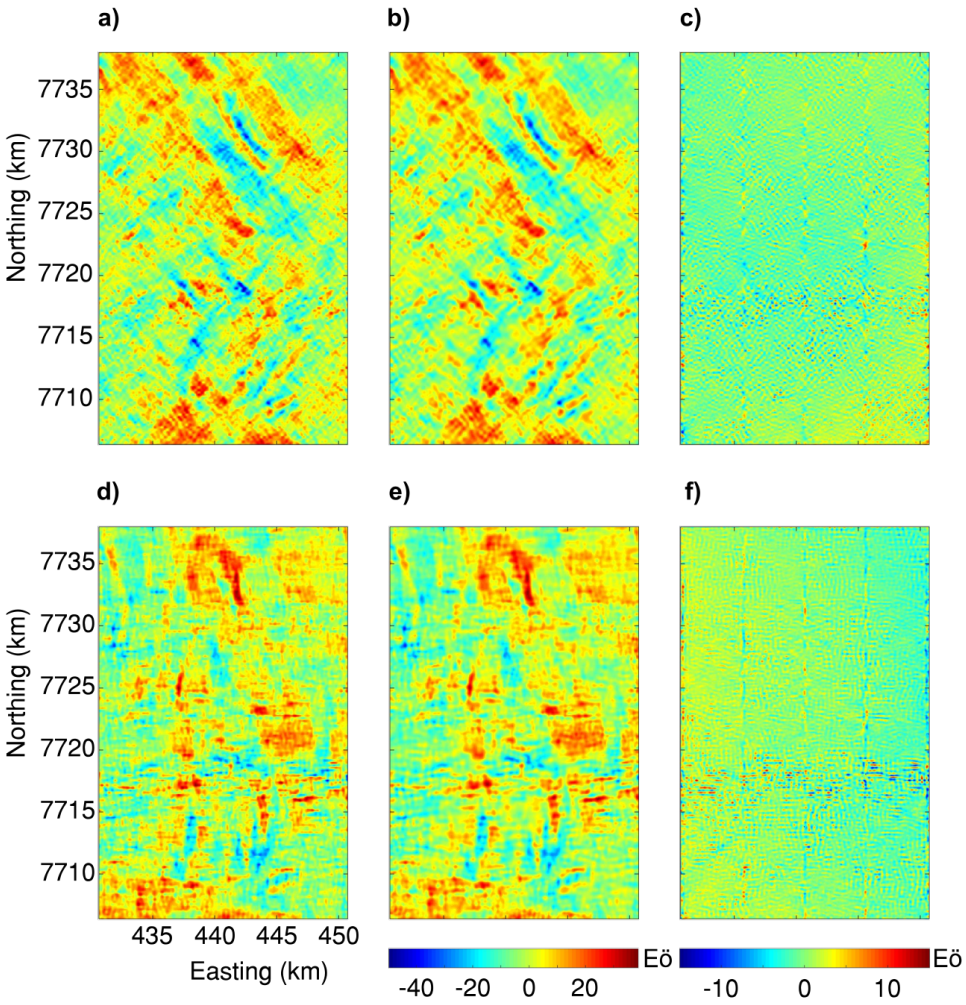

Figure 5.9: Comparison between the equivalent-source reconstructed $\mathbf{G}_{\mathrm{NE}}$ (a) and $\mathbf{G}_{\mathrm{UV}}$ (d) by Fugro Geosciences and the corresponding predicted $\mathbf{G}_{\mathrm{NE}}$ (b) and $\mathbf{G}_{\mathrm{UV}}$ (e) derived from the our method accompanied by their respective differences (c) and (f).

5.4.3 Apparent density estimation

The apparent density estimation itself is another application to demonstrate the versatility of the method. The estimation is based on an underlying assumption that the non-terrain corrected data are heavily masked by the signal from the topography. Our apparent density estimation is dependent on the source layer with the vertically varied dimension. This estimation takes advantage of high-resolution multi-component AGG data as well. The only difference in comparison to the joint noise reduction is that the vertical dimension of the source layer varies with elevation of the topography. We first set up a layer of prisms to approximate the digital elevation map (DEM) of the survey area. We have to modify Equation 5.17 to be able to meet the requirement for apparent density estimation as a result of limitations of FFT.

$$F\left[U\right] = 2\pi G \frac{e^{kz}}{k^2} \frac{2\sin(0.5 \cdot pw \cdot k_x)}{k_x} \frac{2\sin(0.5 \cdot pl \cdot k_y)}{k_y} \left(e^{-kz_t} - e^{-kz_b}\right) F\left[\rho\right]. \tag{5.17}$$

If we can apply Taylor expansion to approximate the undulating upper surface of the

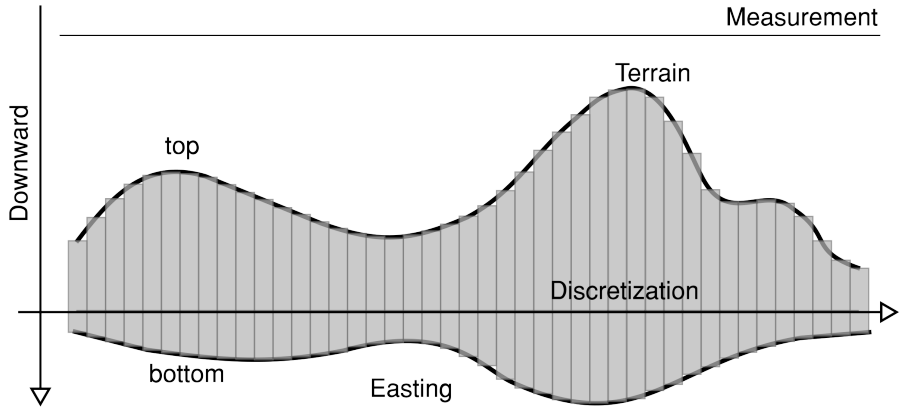

Figure 5.10: The scheme for terrain correction density estimation.

terrain. To accelerate its convergence, we introduce an average depth z_{mt} to the top of the terrain and $z_t = z_{mt} + dz_t$. Following the same rule, there is $z_b = z_{mb} + dz_b$, assuming z_{mb} is the average depth of the bottom of the terrain as illustrated in Figure 5.10. Fortunately, the forward calculation can be done separately and then a simple subtraction followed. So we have its final form as

$$F\left[U_{top}\right] = F\left[\sum_{n=0}^{\infty} \frac{(dz_t)^{tt}}{tt!} \cdot \rho\right] \cdot C_k \cdot e^{-kz_a} \cdot (-k)^n, \tag{5.18}$$

$$F\left[U_{bottom}\right] = F\left[\sum_{m=0}^{\infty} \frac{(dz_d)^{tb}}{tb!} \cdot \rho\right] \cdot C_k \cdot e^{-kz_d} \cdot (-k)^m, \tag{5.19}$$

where $C_k = 2\pi\gamma \frac{e^{k \cdot z}}{k^2} \frac{2\sin(0.5 \cdot pw \cdot k_x)}{k_x} \frac{2\sin(0.5 \cdot pl \cdot k_y)}{k_y}$.

$$F\left[U\right] = F\left[U_{top}\right] - F\left[U_{bottom}\right]. \tag{5.20}$$

It is noteworthy that here m and n can be different, which entirely depends on how complicated the top surface and the bottom surfaces are. In this application, we used 15 Taylor series terms to approximate the terrain. The rest calculations follow Section 5.2.

The depth to the top of the layer is the elevation of the terrain, whereas the bottom of the layer is positioned at the sea level. In this case, it is necessary to modify the kernel that we previously used since the source layer is no longer flat. Because of that, following apparent density estimation will be based on Equation 5.20. Equation 5.20 also requires that the data should be measured at a constant height. It necessitates leveling the two measured components with no topographic correction from the draped surface shown in Figure 5.8a onto a plane at the height of 500 m, which is eight meters higher than the maximum height of the terrain, equivalent to 10 times the grid interval. The resultant $\mathbf{G}_{\mathrm{NE}}$ and $\mathbf{G}_{\mathrm{UV}}$ are shown in Figure 5.12a and Figure 5.12d, respectively. The input DEM is exhibited in Figure 5.11. In addition, as for all geophysical inversions, a proper starting model is essential. According to the in-situ density observations, the average bulk density of the survey area is around 2.9 g/cm^3. Therefore, we start the algorithm off with a homogeneous starting model with density of 2.9 g/cm^3. We invert two measured components simultaneously at the same time to constrain the inversion. As a rule, the parameters like the relaxation factor and the number of Gaussian nodes M are 0.001 and 2, respectively.

While the algorithm runs recursively, we compare the residue derived from the predicted data subtracted from the input data with the measured $\mathbf{G}_{\mathrm{NE}}$ and $\mathbf{G}_{\mathrm{UV}}$ terrain corrected by Fugro Geosciences at every iteration. In that case, we are able to find out at which iteration the algorithm has started fitting content associated with deep sources. The presumption is that after topographic correction, the influence of the terrain effects has been greatly minimized. Therefore, we use a mathematical distance between the derivative residue and the terrain-corrected data for this purpose. The distance is defined as the root mean square (RMS) of the difference between the residue and the terrain-corrected data. The distance curves shown in Figure 5.13 are expected because, with

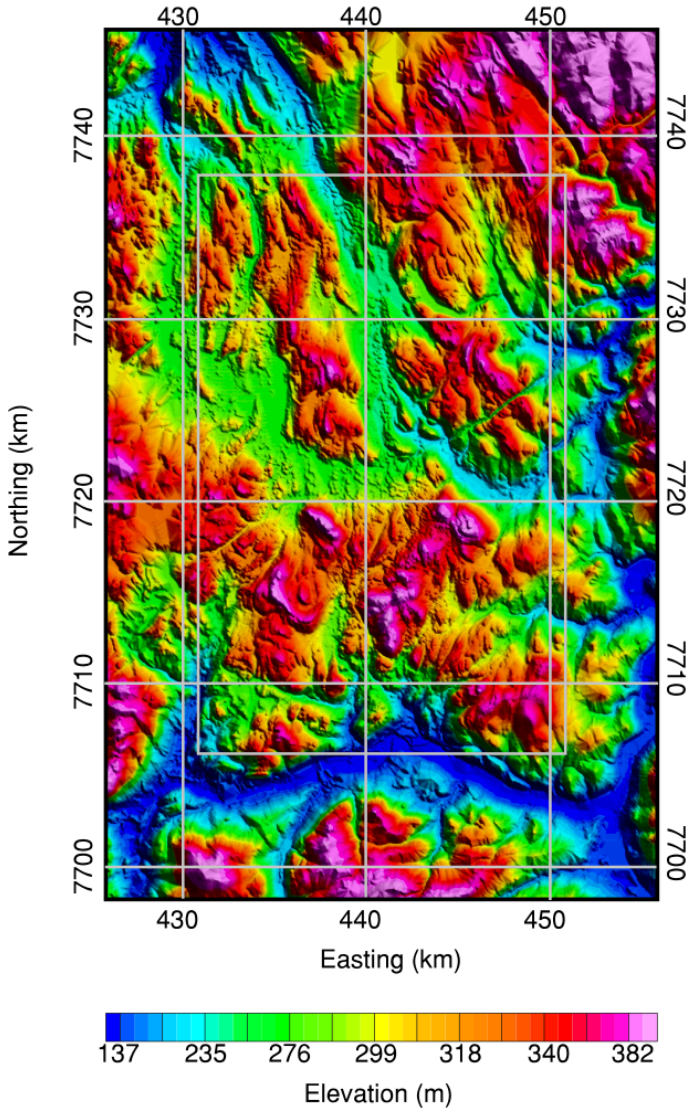

Figure 5.11: The extended digital elevation map re-gridded from the data provided by Fugro Geosciences for the purpose of the apparent density estimation, in which the survey area is outlined by a solid line rectangle in the middle.

iterations, the algorithm will eventually fit the signal from the deep structures until it reaches a certain level of fitness. Presumably, a point at which the increasing distance slows down plays an important role in the indication like the 10th iteration. Because the larger distance indicates that more signal from the deep sources has been translated into the apparent density. So we just take the inverted densities derived from the first five iterations and then average them to retrieve the estimated apparent density. (As for the reason that the first five iteration instead of possible combination are used for the estimation, it is beyond the scope of the paper.). The predicted $\mathbf{G}_{\mathrm{NE}}$ and $\mathbf{G}_{\mathrm{UV}}$ from

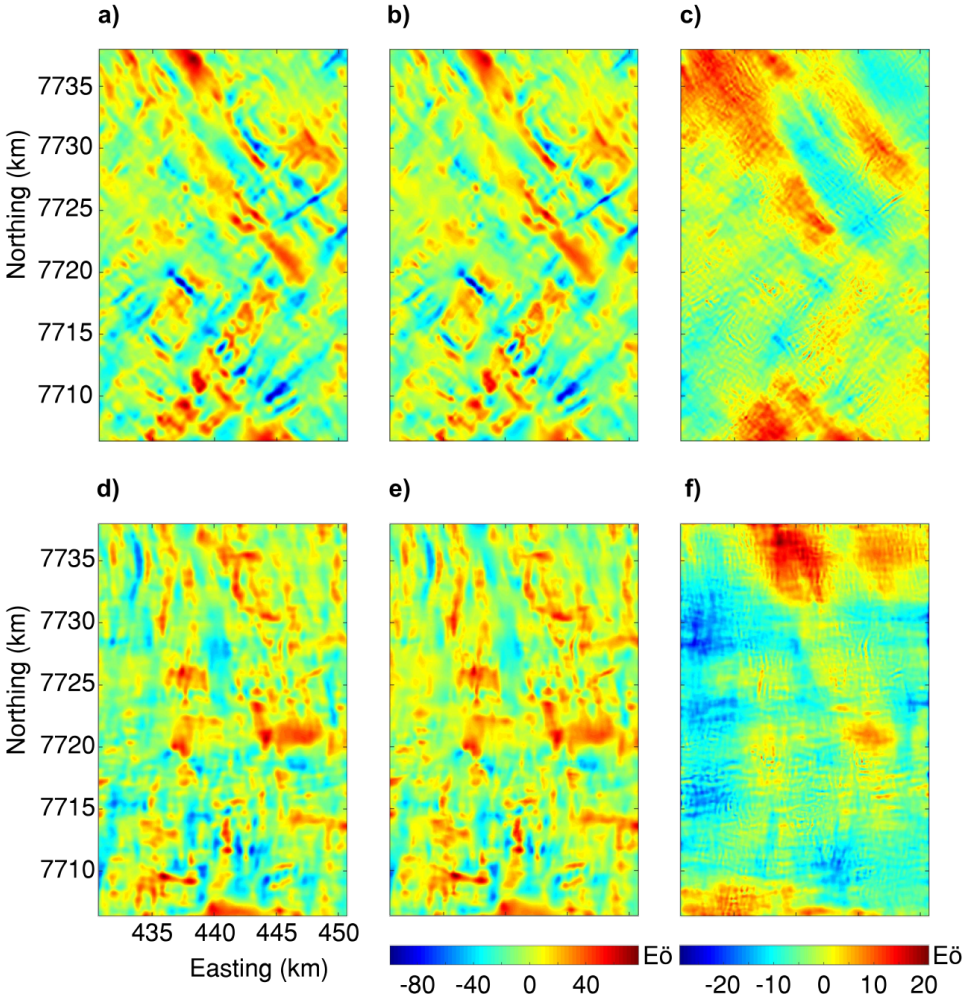

Figure 5.12: Comparison between the input $\mathbf{G}_{\mathrm{NE}}$ (a) and $\mathbf{G}_{\mathrm{UV}}$ (d) data without topographic correction jointly leveled up to 500 m and the corresponding predicted $\mathbf{G}_{\mathrm{NE}}$ (b) and $\mathbf{G}_{\mathrm{UV}}$ (e) as well as their respective differences (c) and (f).

the estimated apparent density are displayed in Figure 5.12b and Figure 5.12e. Visually, the major contents in both components are translated into the density distribution. The minor difference between the input data and predicted data can be regarded the content induced by the deep structures. The $\mathbf{G}_{\mathrm{NE}}$ and $\mathbf{G}_{\mathrm{UV}}$ component do not look straightforward. For convenience, we take the $\mathbf{G}_{\mathrm{DD}}$ component (the Down-Down component of gravity gradients) as an example, because the behavior of $\mathbf{G}_{\mathrm{DD}}$ can to some extent reflect the shape of the sources. In Figure 5.14, the left panel displays the $\mathbf{G}_{\mathrm{DD}}$ data with the reduced terrain effects, resulted from the estimated apparent density, and the middle panel presents the terrain corrected $\mathbf{G}_{\mathrm{DD}}$ data by Fugro Geosciences along with the $\mathbf{G}_{\mathrm{DD}}$

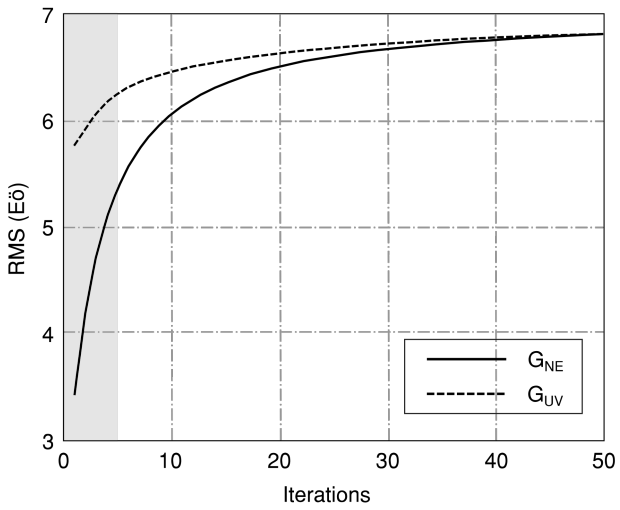

Figure 5.13: The distance derived from recursive comparison between the residue (the predicted data subtracted from the input) and the terrain corrected measured data by Fugro Geosciences for both components.

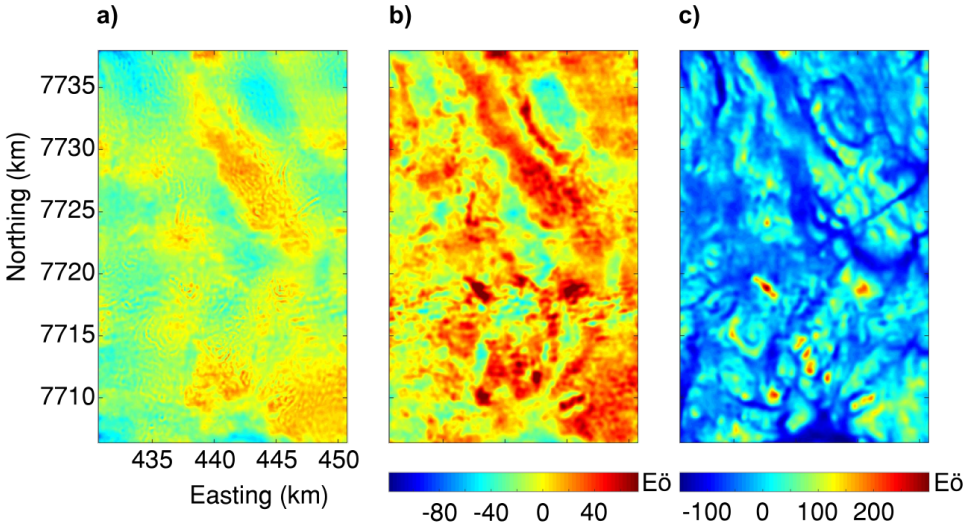

Figure 5.14: Comparison between different methods of reducing terrain effects. The panels display from left to right, the $\mathbf{G}_{\mathrm{DD}}$ data with reduced terrain effects (a) resulted from the method, the $\mathbf{G}_{\mathrm{DD}}$ data after topographic correction (b) by Fugro Geosciences, and the $\mathbf{G}_{\mathrm{DD}}$ data with no topographic correction.

data without topographic correction. The above three datasets are leveled up to the same height of 500 m. In comparison, the left panel shows less high-frequency content, especially some topography-related structures. Some residuals due to terrain correction such

as two anomalously high positive signal in the lower middle of Figure 5.14b and Figure 5.14c are not visually detected in the left panel. In summary, it appears that the method is able to deliver acceptable estimated apparent density.

The resultant apparent density of the topography is displayed in Figure 5.15 and Table 5.2. From Figure 5.15, the corresponding points of the two pictures show general resemblance. In Table 5.2, the samples listed in the table are samples geographically close to the grid points consisting of the estimated apparent densities. The following analysis is built on the assumption that the in-situ measured density is representative of the host rock at depth. From the table, there are 9 estimated apparent density samples with the error smaller than 0.1 g/cm^3 out of 16. The root mean square of the error is only 0.148 g/cm^3. It seems inevitable that the in-situ density samples are highly unlikely to adequately represent the survey area with an average 200m thickness of the terrain. Superficial rocks are subject to weathering and often are less dense than their deeper and unweathered counterparts. For instance, densities given by Sample 7 and 8 as well as Sample 11 and 12 in Table 5.2 have quite a large discrepancy around 0.16 g/cm^3, which might be due to alterations of the surface as for example from weathering.

We notice that the estimated apparent density in some regions is anomalously high or low. The following factors are plausible causes of this issue. First of all, in reality, the fact that the method does not allow density to vary vertically inside a prism-shaped column itself leads the approach to compromise. Second, to separate terrain effects from the whole is often an arduous task. Thus, the influence of the deep structures on the estimate is impossible to avoid. The factors discussed above play an important part in accurate apparent density estimation. It is no wonder that the estimated apparent density may over-represent or under-represent the area like the in-situ measured density data. Nevertheless, it still offers an opportunity for quick apparent density estimation to give a general idea about the terrain.

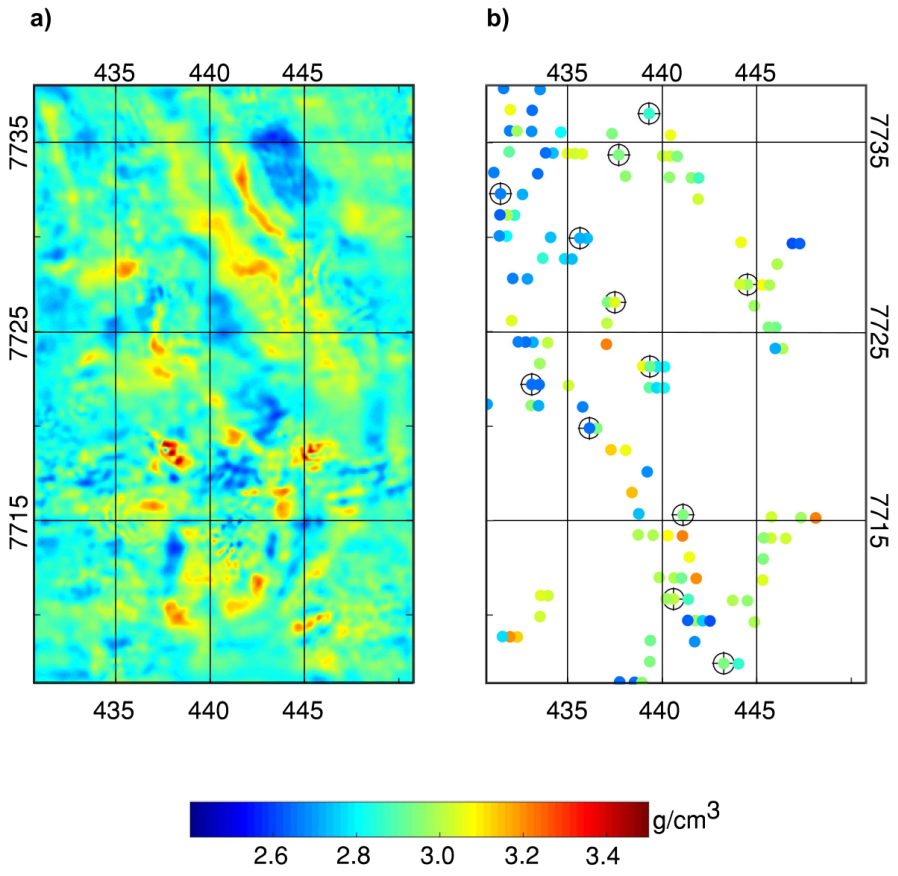

Figure 5.15: A display of the resultant apparent density estimate (a) and the measured density (b) sampled inside the survey area. A cross outlined by a circle is used to indicate samples listed in Table 5.2.

Number #	X-coordinates (m)	Y-coordinates (m)	Measured (g/cm^3)	Apparent (g/cm^3)	Estimation error (g/cm^3)	Rock type
1	440597	7710854	3.04	2.97	0.07	Gabbro
2	440597	7710854	3.00	2.97	0.03	Gabbro
3	437697	7734354	2.95	2.97	-0.02	Amphibolite
4	439302	7736544	2.85	2.82	0.04	Metasediment
5	444505	7727492	2.97	3.03	-0.05	Metasediment
6	439347	7723156	2.92	2.97	-0.05	Pelite
7	436147	7719893	2.84	2.81	0.03	Pelite
8	436147	7719893	2.65	2.81	-0.16	Pelite
9	435641	7729947	2.71	2.85	-0.14	Pelite
10	443253	7707443	2.94	2.85	0.09	Psammite
11	441098	7715303	3.09	2.80	0.29	Gabbro
12	441098	7715303	2.93	2.80	0.13	Gabbro
13	437491	7726551	3.06	2.86	0.21	Gabbro
14	437491	7726551	3.04	2.86	0.18	Gabbro
15	431442	7732296	2.67	2.76	-0.09	Gneiss
16	433096	7722208	2.65	2.96	-0.31	Pelite

Table 5.2: A comparison between 16 in-situ measured density and their geographically closest estimated apparent density (the distance discrepancy $\leq$ 10 m). The identified rock types where the samples are located are also provided, accordingly.

5.5 Conclusion

We present a fast method to calculate equivalent source for multiple airborne gravity gradient components. In our method, we integrated Gauss-FFT with Landweber's iteration coupled with a mask matrix originally for deconvolution of astronomical images to reduce the computation cost of equivalent source technique with acceptable accuracy. Our method is successfully applied to the synthetic data. We also demonstrate how to apply our method to jointly reduce the noise of the measured data in Karasjok, Norway. The result turns out to be comparable with the industrial-standard output provided by Fugro Geosciences. Plus, with minor modification, we are able to estimate apparent density of the topography of the survey area, which offers us another opportunity to have a general idea of density distribution inside the topography. And the efficiency and effectiveness of our method have been demonstrated with both the synthetic and the real examples. Admittedly, it is inevitable for the method to inherit some weaknesses of calculation in the wavenumber domain. In the future, we hope that we will be able to apply this method for real full tensor gravity measurements and there might be the possibility of modifying this method for 3D inversion. However, our method is a fast alternative to people interested in using equivalents source method for large-scale multi-component datasets processing.

Chapter 6

Stochastic Inversion of Airborne Gravity Gradient Data

We present results from inversion of airborne gravity gradient data of the Karasjok Greenstone Belt. Airborne gravity gradient data had been previously used to construct a structural model in conjunction with surface geological observations and bedrock properties. Forward calculation of this structural model fits the long-wavelength signals of the airborne gravity gradient data but poorly explains the observed short-wavelength signals. This can be explained by resolution of the model and the use of constant densities for each lithology. To the refine density distribution of the model, we apply stochastic inversion in a Bayesian inversion framework to handle the model uncertainties and to avoid computing large-scale matrix inversion. The inversion is applied to the measured airborne gravity gradient components, noise-reduced gravity gradient components, and various combinations of the constructed gravity gradient tensor components. It is shown that noise-reduction is not necessary a must prior to inversion unless noise is significant enough to mask real signals or noise is no longer Gaussian random noise. It is also demonstrated that the inversion of five or six tensor components does not necessarily improve the model resolution and provide additional information. An inversion of the two measured or a subset of the constructed full tensor gravity components can equally serve the purpose of interpretation with significantly reduced computation time. The results show a bent area with high-densities ($\geq$0.4 g/m^3) that can be associated with mineralization, for example in the Gallujavri area. These areas are more clearly seen in the inverse results than from the geological 3D model alone.

6.1 Introduction

In recent years, due to the advantage of rapid acquisition and high spatial resolution as well as high signal-to-noise ratio measurements, an ever-increasing number of airborne gravity gradiometry (AGG) surveys have been flown for mineral exploration (Barnes and Lumley, 2011; Dransfield and Christensen, 2013). As for many geophysical methods used for mineral exploration, inversion is widely used as a quantitative way of geological interpretation (Martinez et al., 2013). Therefore, various inversion approaches for gravity data have been developed, such as deterministic e.g., (Li and Oldenburg, 1996; Zhdanov et al., 2004; Leliévre et al., 2012) and stochastic methods e.g., (Guillen et al., 2004; Bosch et al., 2006; Shamsipour et al., 2010).

However, there is still noise existing in the delivered gravity gradient data (Dransfield and Christensen, 2013; DiFrancesco et al., 2009a). Therefore, it is important to examine whether the existing noise influence results of inversion and if it is necessary to do noise reduction prior to inversion, even though conventional inversion algorithms has some noise immunity (Zhdanov et al., 2004).

Furthermore, because AGG system only measures two curvature components, the other gravity gradient tensor components have to be constructed (Nabighian et al., 2005). However, the construction causes discrepancies up to 5 Eö between measured and constructed components. Along with the difficulty of accurately estimating the noise level of the constructed data, some geophysicists argue that only the measured data should be used in inversion (per. comm. Tim Archer).

Concerning linearized deterministic inversion of multi-component gravity gradient data, one may intuitively think that the more tensor components are involved, the more information can be extracted from the data. However, Pilkington (2012) has examined the optimal gravity gradient components for inversion and points out that the choice of tensor components included in inversion should be carefully made according to the measurement-source distance rather than simply using as many tensor components as possible. Paoletti et al. (2016) suggest that keeping algebraic ambiguity and noise level low is more important than the choice of tensor components in inversion. In stochastic inversion, owing to strong dependence on prior information, fewer studies have systematically addressed such issue.

AGG data are known for their high sensitivity to near-surface sources and the ability to detect and image sources vertical and lateral directions (Dransfield and Christensen, 2013). Conventionally, a routine interpretation of gravity gradient data includes structural analysis, lithological interpretation, geological model construction and last but not least density distribution determination (Forward modelling and inversion with 3D GeoModeller by Intrepid Geophysics). Following the above routines, a geological model of the area of interest is normally built dependent on the acquired geophysical and petrophysical data. Even though as many constraints as available are considered, any resulting model is always a simplification of the real scenario. For example, the complexity of the upper surface of the earth makes the choice of a constant density for a lithology insufficient to describe the real geological scenario, especially not appropriate for the prospecting purpose.

In this paper, we will invert airborne gravity gradient data with the constraints of acquired petrophysical data and an existing lithology model in order to retrieve the detailed density distribution of the survey area and in the meanwhile to examine the influence of noise reduction on inversion and the usefulness of various combinations of gravity gradient tensor component in inversion. This will make the inverse problem great non-linear and lead to difficulty in handling the inverse problem in a conventional deterministic manner. For that reason, we adopt a stochastic approach implemented in an industry-standard software GeoModeller[2] within the Bayesian framework to tackle this issue. We will first review the basics of stochastic inversion used in the software, and then briefly describe the survey and geology settings of the study area. Subsequently, we will present the results from stochastically inverting six different combinations of the AGG components. At the end, we will discuss some details of the Karasjok Greenstone Belt and as zones of potential mineralization with the help of the inverse density model.

6.2 Methodology

From measurements to the causative source, this process refers to inversion. The inverse calculation can be systematically unstable (Zhdanov, 2002) and several approaches exist to circumvent this limitation. For example, instead of obtaining least square sense solution

[2]GeoModeller is software for building implicit 3D geological models, and performing forward & inverse geophysical modeling directly using stochastic inversion techniques, for more details: http://www.intrepid-geophysics.com.

to a strongly ill-posed inverse problem, we can resort to statistical or Bayesian inversion, which can systematically handle uncertainties of models and reduce ill-posedness.

In addition, the knowledge available on the model other than measurements is referred to as prior probability density (Tarantola, 2005). Using vector notation, the probability of observed data $\mathbf{d}_{\text{obs}}$ given a model $\mathbf{m}$ is expressed with likelihood function $P(\mathbf{d}_{\text{obs}}|\mathbf{m})$ that measures the level of fit between measurements and predictions resulted from the model $\mathbf{m}$, the objective function of Bayesian inversion is given by (Tarantola, 2005)

$$P(\mathbf{m}|\mathbf{d}_{\text{obs}}) = \frac{P(\mathbf{d}_{\text{obs}}|\mathbf{m})P(\mathbf{m})}{P(\mathbf{d}_{\text{obs}})}. \tag{6.1}$$

The denominator is the probability of observations. It is independent of a particular model and can be regarded as a constant. Then Equation 6.1 can be simplified as

$$P(\mathbf{m}|\mathbf{d}_{\text{obs}}) \propto P(\mathbf{d}_{\text{obs}}|\mathbf{m})P(\mathbf{m}), \tag{6.2}$$

where the likelihood function in Equation 6.2 is proportional to $\exp\left[-\frac{1}{2}\left(\frac{\mathbf{d}_{\text{obs}}-\mathbf{Gm}}{\sigma}\right)^2\right]$. In the equation, $\mathbf{G}$ stands for a sensitivity matrix connecting input data and a given model, which is a Jacobian matrix of partial derivatives of synthetic data with respect to model parameters (Sen and Stoffa, 2013).

Directly sampling the posterior probability density function $P(\mathbf{m}|\mathbf{d}_{\text{obs}})$ usually is impossible in hyper-dimensional solution space. Therefore, the Metropolis-Hastings algorithm is designated to solve this problem (Hastings, 1970). The algorithm dictates that a newly proposed model that can reduce misfit will be definitely accepted, and otherwise accepting or rejecting the newly proposed model is randomly determined. Therefore, the accepted realizations are candidate solutions, which is equivalent to direct drawing samples from the posterior probability distribution.

As for GeoModeller, the implementation of the stochastic inversion is summarized in Figure 6.1. Since no depth weighting functions and other constraints are used for lithology structures, an acceptable prior model as a result of the joint interpretation of available geophysical observations, geological observations as well as petrophysical observations is a prerequisite for stochastic inversion. Typically, a prior model is composed of several geological units. Then we have to determine physical laws for all the geological units by statistical analysis of rock samples which are taken inside a certain geological unit, such as density distributions, susceptibility distributions and so forth. In our case, since density normally follows Gaussian distributions, a density distribution is conventionally

described by an arithmetic mean and a standard deviations of a group of rock samples. As a result, it is called litho-constrained stochastic inversion (Guillen et al., 2004).

With the input prior lithology model and user-defined physical laws, a random starting model is automatically generated according to the input. This randomly generated starting model will be given a random change in the subsequent inversion in every iteration. After millions of iterations, GeoModeller will generate a great number of realizations (density models in our case), but only the realizations which are accepted by the Metropolis-Hastings algorithm will be preserved as candidate solutions to the stochastic inversion. The statistics of the preserved realizations are automatically retrieved such as an arithmetic mean and a standard deviation, accordingly. The arithmetic mean can be used for the interpretation (Fontanini, 2016), and the standard deviation is a measure of the dispersion of the accepted realizations. A small standard deviation indicates that the realizations are close to the arithmetic mean of the set, whereas a high standard deviation indicates that the realizations are spread out over a wider range of values. Therefore, a small standard deviation is invariably desirable.

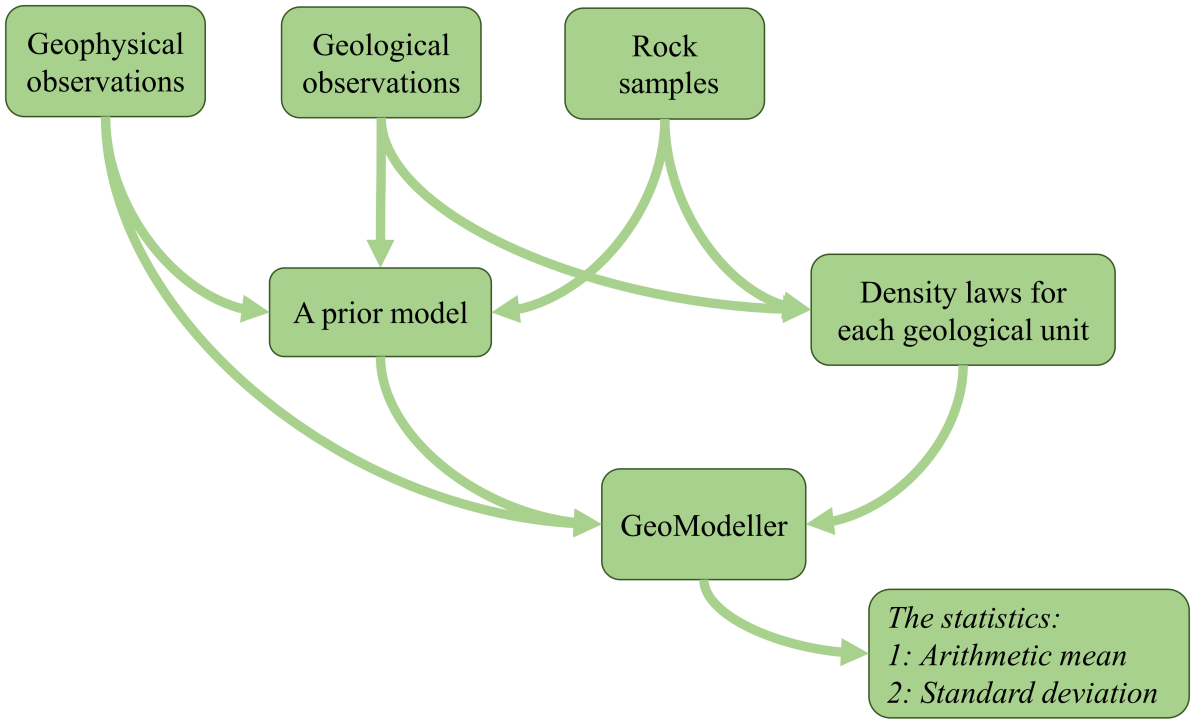

Figure 6.1: A schematic flowchart about the way of stochastic inversion conducted in GeoModeller (The User Help and accompanied by tutorials of GeoModeller).

6.3 Data

Measured data The airborne gravity gradiometry survey undertaken by FALCON Airborne Gravity Gradiometer(AGG) system took place around the area centered on longitude 25°30' E, latitude 69°35' N in Norway and covers of 31.7 $\times$ 19.7 km of the northern part of the Karasjok Greenstone belt outlined with a black rectangle in Figure 6.2. The AGG system simultaneously acquires two non-vertical gravity gradient components, namely $\mathbf{G}_{\mathrm{NE}}$ (the North-East component of gravity gradient tensor) and $\mathbf{G}_{\mathrm{UV}}$ (a half of the difference between the North-North component and the East-East component of gravity gradient tensor). The survey was flown at a height of around 117 m above the terrain and the line spacing of the West-East traverse lines is 200 m. The measured $\mathbf{G}_{\mathrm{NE}}$ and $\mathbf{G}_{\mathrm{UV}}$ (shown in Figure 6.2) were low-pass filtered at 0.18Hz (Fugro Data Processing Report, 2011). In addition, the data were routinely terrain-corrected and tie-line leveled by Fugro Geosciences.

Denoised data In Chapter 4, the measured data have been demonstrated to have some noise. Therefore, the noise-reduced (denoised) data are also provided. In applying the new noise reduction method, the height was set to 100 m, equivalent to twice the sample interval, the maximum number of iterations was set to 1000 which is used to stop the iteration if the threshold at 90% of the noise level cannot be achieved. The results are presented in Figure 6.3 and Figure 6.4. The respective the cut-off wavelengths for $\mathbf{G}_{\mathrm{NE}}$ and $\mathbf{G}_{\mathrm{UV}}$ are 510 m and 489 m. It can be seen that the distributions of the differences follow a zero-mean Gaussian distribution (Figure 6.4). The respective standard deviations for $\mathbf{G}_{\mathrm{NE}}$ and $\mathbf{G}_{\mathrm{UV}}$ are 3.34 Eö and 3.22 Eö. As a consequence, it is important to know if the noise reduction plays a role in inversion.

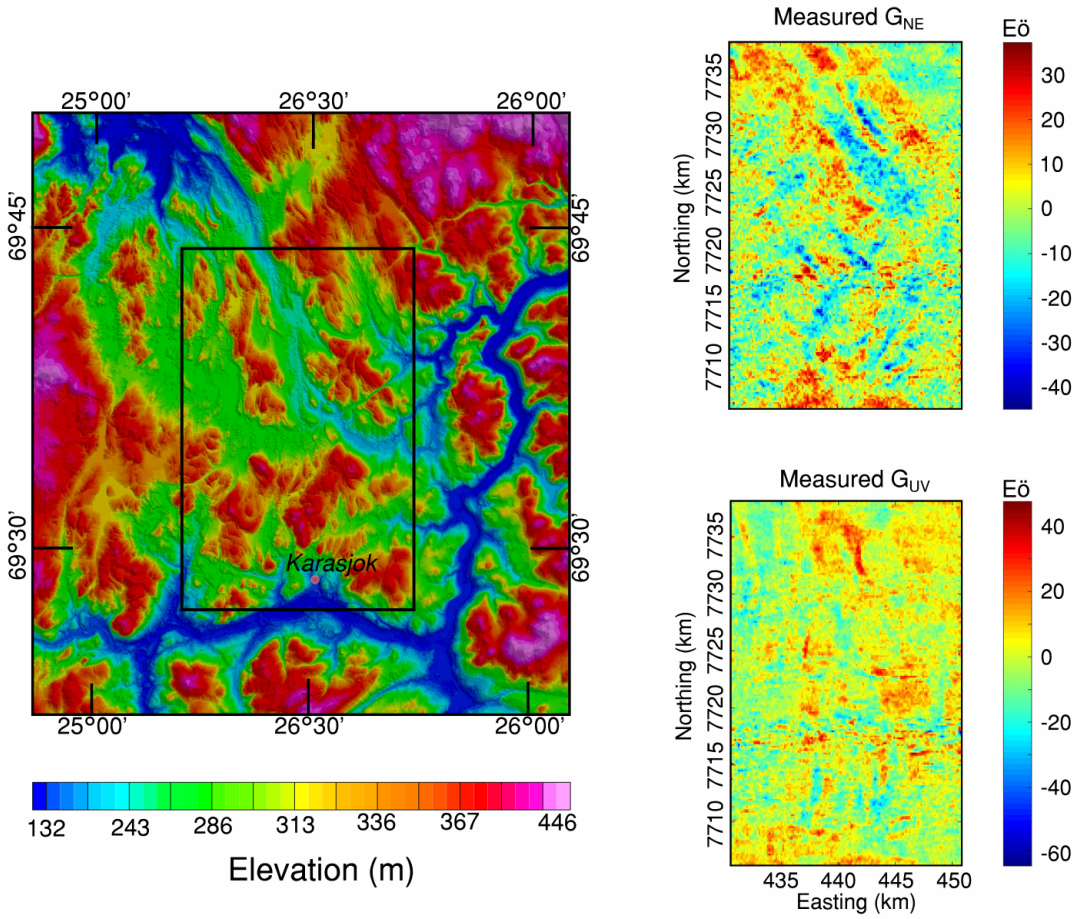

Figure 6.2: The measured data and the survey area, which is outlined with a black rectangle.

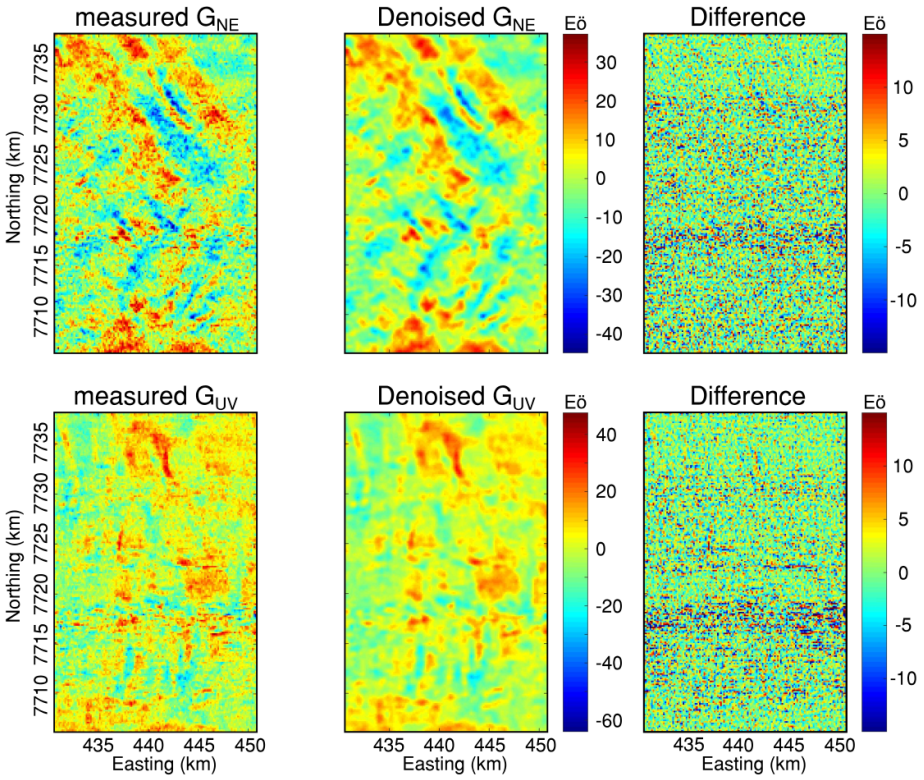

Figure 6.3: Comparison between the measured data and the noise-reduced data demonstrated in Chapter 4 and their corresponding differences.

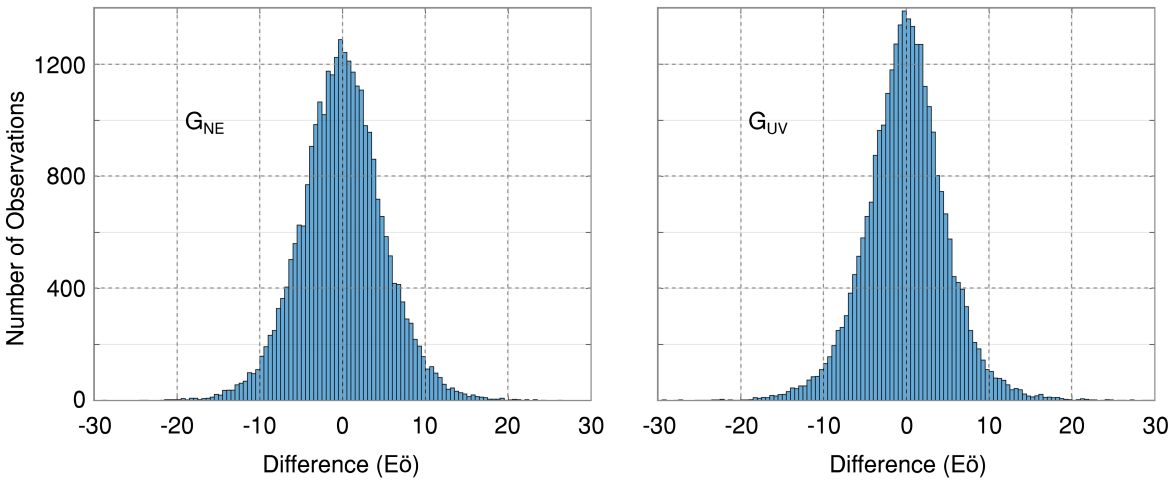

Figure 6.4: Distributions of the differences between the measured data and the noise-reduced data.

Constructed data Since FALCON AGG system measures two non-vertical gravity gradients $\mathbf{G}_{\mathrm{NE}}$ and $\mathbf{G}_{\mathrm{UV}}$, the full tensor gravity (FTG) has to be obtained from the two main approaches currently in use, such as the Fourier transform approach and the equivalent source method (Nabighian et al., 2005; Barnes and Lumley, 2011). For future reference, constructed data are acquired based on the above data processing methods whereas measured data in the paper are direct measurements delivered by FALCON AGG system without any construction process. Due to the difficulty of computing equivalent sources without over-smoothing or under-smoothing the data and the fact that only $\mathbf{G}_{\mathrm{NE}}$, $\mathbf{G}_{\mathrm{UV}}$, and $\mathbf{G}_{\mathrm{DD}}$ were constructed based on the equivalent source method by Fugro Geocsiences, whereas the full tensor gravity components were constructed based on Fourier transform, the Fourier transform approach is often preferred (Pilkington, 2014). As we are using data measured from the FALCON system, the potential field can be determined (Lee, 2001)

$$F(\Phi) = -\frac{-2i}{(k_x - ik_y)^2} F(\mathbf{G}_{\mathrm{NE}} + \mathrm{i}\mathbf{G}_{\mathrm{UV}}), \tag{6.3}$$

where k_x and k_y are wavenumbers in the x-axis and y-axis, respectively. The Fourier transform of the gravity gradient potential Φ can be calculated. F stands for the forward Fourier transform. The filter can be considered as a band-pass filter. Theoretically, coherent signals are reinforced but noise and incompatible contents out of phase tend to be reduced after the transform (Pilkington, 2014). The constructed $\mathbf{G}_{\mathrm{NN}}$, $\mathbf{G}_{\mathrm{EN}}$, $\mathbf{G}_{\mathrm{DN}}$, $\mathbf{G}_{\mathrm{EE}}$, $\mathbf{G}_{\mathrm{ED}}$, and $\mathbf{G}_{\mathrm{DD}}$ are shown in Figure 6.5.

Actually, the constructed $\mathbf{G}_{\mathrm{NE}}$ and $\mathbf{G}_{\mathrm{UV}}$ are comparable with their measured counterparts but not exactly identical (Figure 6.6). Despite the fact that the measured data have been low-pass filtered by Fugro Geosciences, the respective standard deviations of the differences for $\mathbf{G}_{\mathrm{NE}}$ and $\mathbf{G}_{\mathrm{UV}}$ components are up to 5.18 Eö and 5.11 Eö. The differences also follow normal distributions (Figure 6.7).

According to Equation 6.3, the high-frequency noise and errors will inevitably propagate into constructed data. As a result, it is important to examine if the routinely processed data which meet the industry standards are able to deliver equally comparable results and if the discrepancy due to the construction process will affect results of inversion. For this purpose, we do not apply any extra noise reduction methods to the AGG data and only use the data which were routinely processed by Fugro Geosciences.

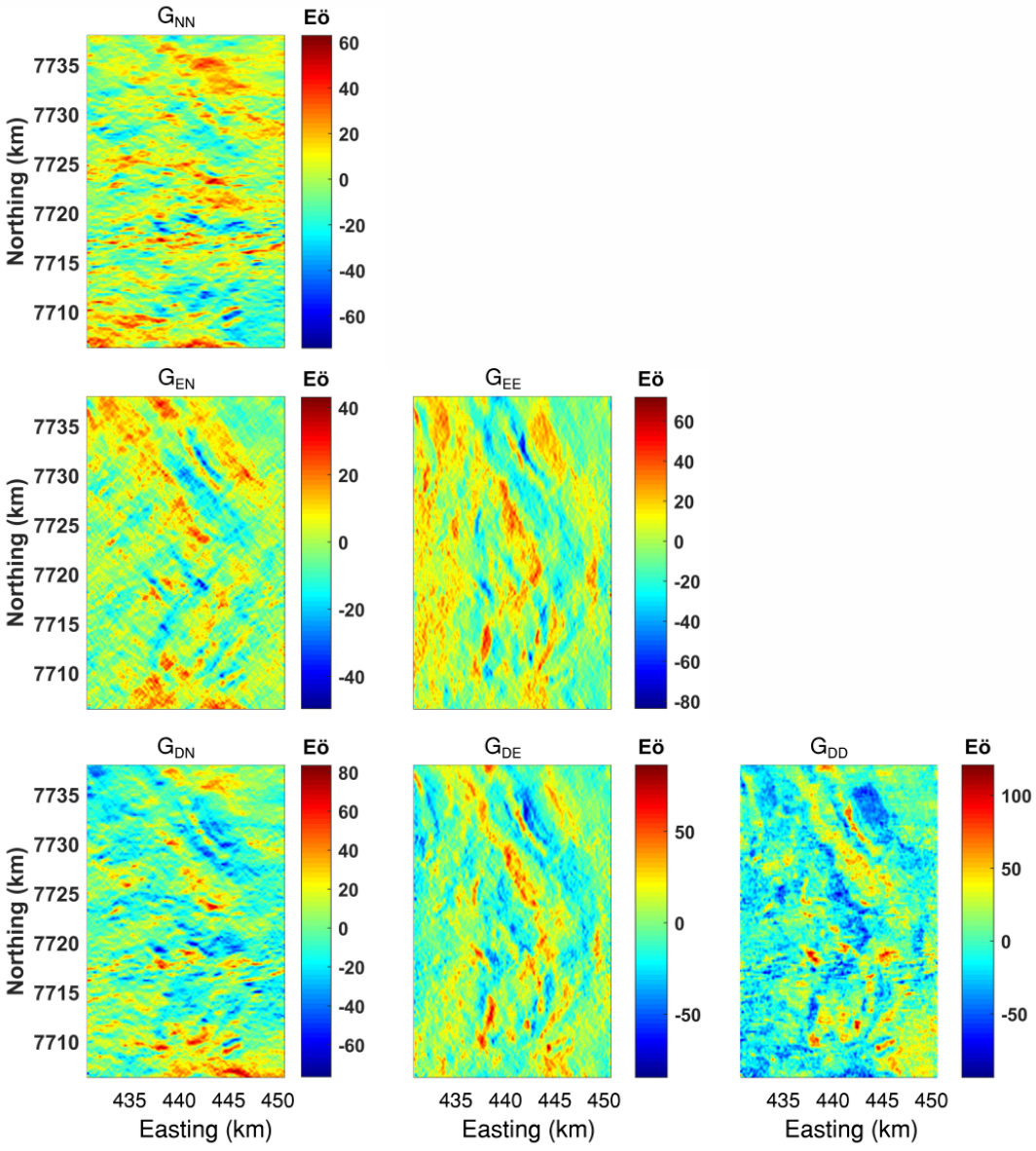

Figure 6.5: Display of the constructed gravity gradient data. The data were routinely low-pass filtered, terrain corrected, and constructed by Fugro Geosciences.

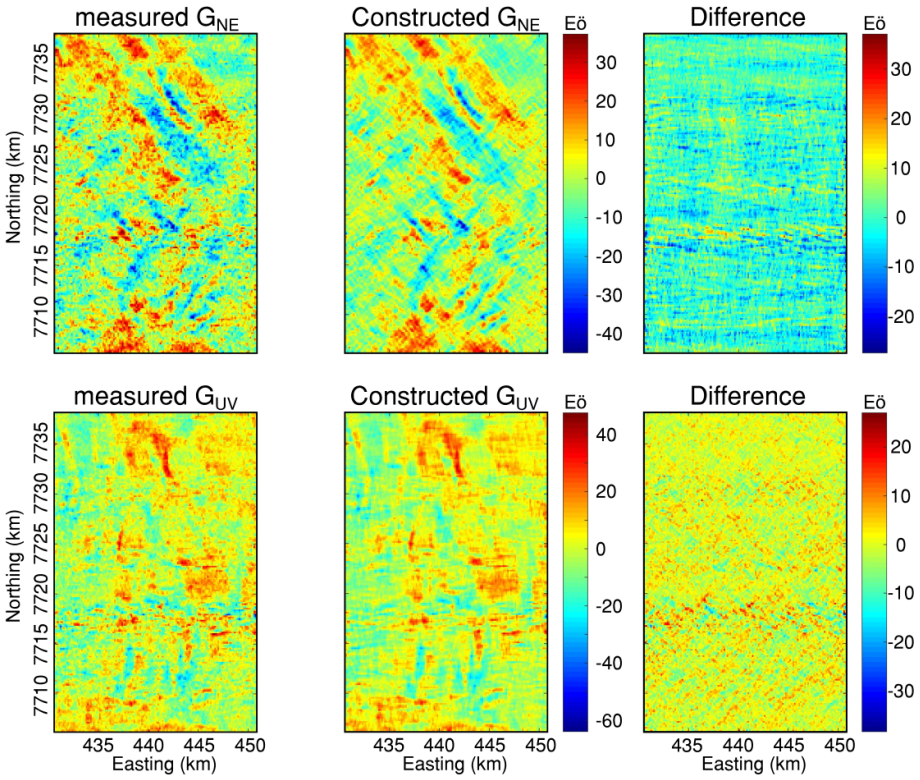

Figure 6.6: Comparison between the measured $\mathbf{G}_{\mathrm{NE}}$ and $\mathbf{G}_{\mathrm{UV}}$ and the constructed $\mathbf{G}_{\mathrm{NE}}$ and $\mathbf{G}_{\mathrm{UV}}$ and their corresponding differences. The constructed $\mathbf{G}_{\mathrm{UV}}$ here is directly computed from the constructed $\mathbf{G}_{\mathrm{NN}}$ and $\mathbf{G}_{\mathrm{EE}}$ components as shown in Figure 6.5.

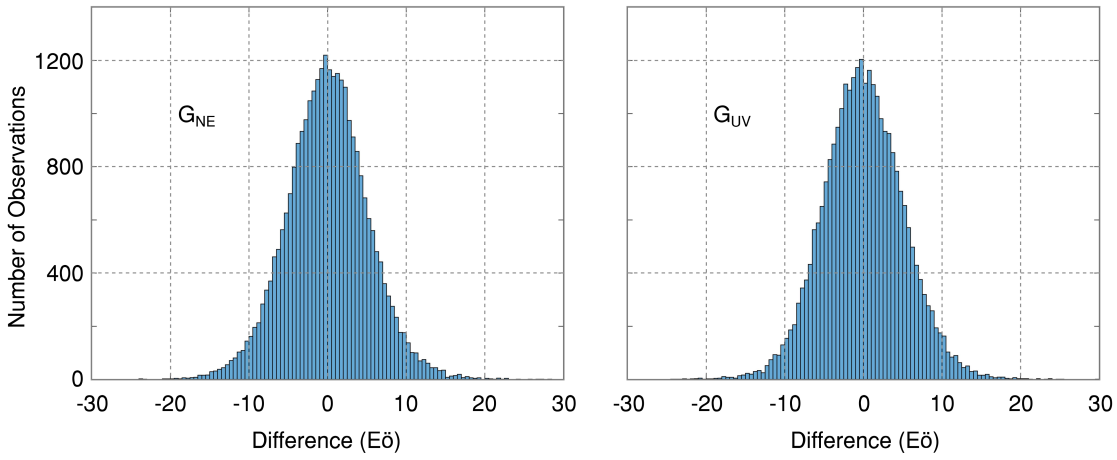

Figure 6.7: Distributions of the differences between the measured data and the constructed data.

6.4 Geology

The Paleoproterozoic Karasjok Greenstone Belt (KGB) is unique amongst the Norwegian greenstone belts as it has both abundant ultramafic intrusions, komatiites and abundant gabbroic intrusions across greenstones, amphibolites and even migmatites (Nillsson and Often, 2006). The rock samples were systematically collected from the Finnmark area (Midtun, 1988). The acquired petrophyiscal measurements shown in Figure 6.8 are summarized in Table 6.1.

The Karasjok Greenstone Belt (Figure 6.8) has a North-South trend with the length of about 160 km, and a range in width from 20 to 40 km. To the west, it is non-conformably overlying and partly thrust over the granitic basement rocks of the Archean Jergul Gneiss Complex (JGC), which provides a base for the Karasjok Greenstone Belt (Krill, 1985) To the east, it is bounded by the over-thrusted Tanaelv Migmatite Complex (TMC), which is a narrow belt of high-grade metamorphic rocks (Often, 1985). The two most predominant parts of the Karasjok Greenstone Belt are the Gallebaike Formation and the Bakkilvarri Formation (Often, 1985; Siedlecka, 1985; Braathen and Davidsen, 2000).

The Bakkilvarri Formation is interpreted as a thick monotonous sequence of low magnetic amphibolites with mafic or ultramafic volcanic rocks, minor distribution of metasediment and an unusual abundance of relatively highly magnetic komatiite by volume compared to other greenstone belts (Often, 1985). Due to the the presence of the amphibolites, the average density of the Bakkilvarri Formation is relatively higher than that of the Gallebaike Formation .

The Gallebaike Formation consists of mixed lithologies, ranging from metapsammites and metapelites to thin layers of amphibolites. Mica schists and fuchsite-bearing schist, with 5-10 m thick beds of amphibolites, make up the lowermost part of the formation. The upper parts show a transition to sandstones and feldspar-rich quartz (Often, 1985; Siedlecka, 1985; Skaar, 2014). These relatively low-density rocks make up the average density of the area of around 2.8 g/cm^3 (See Table 6.1).

Several mafic to ultramafic intrusions can be observed throughout the stratigraphical units in the KGB. The mafic and ultramafic intrusions occur dominantly as isolated intrusions, without any clear relation to each other (Skaar, 2014).

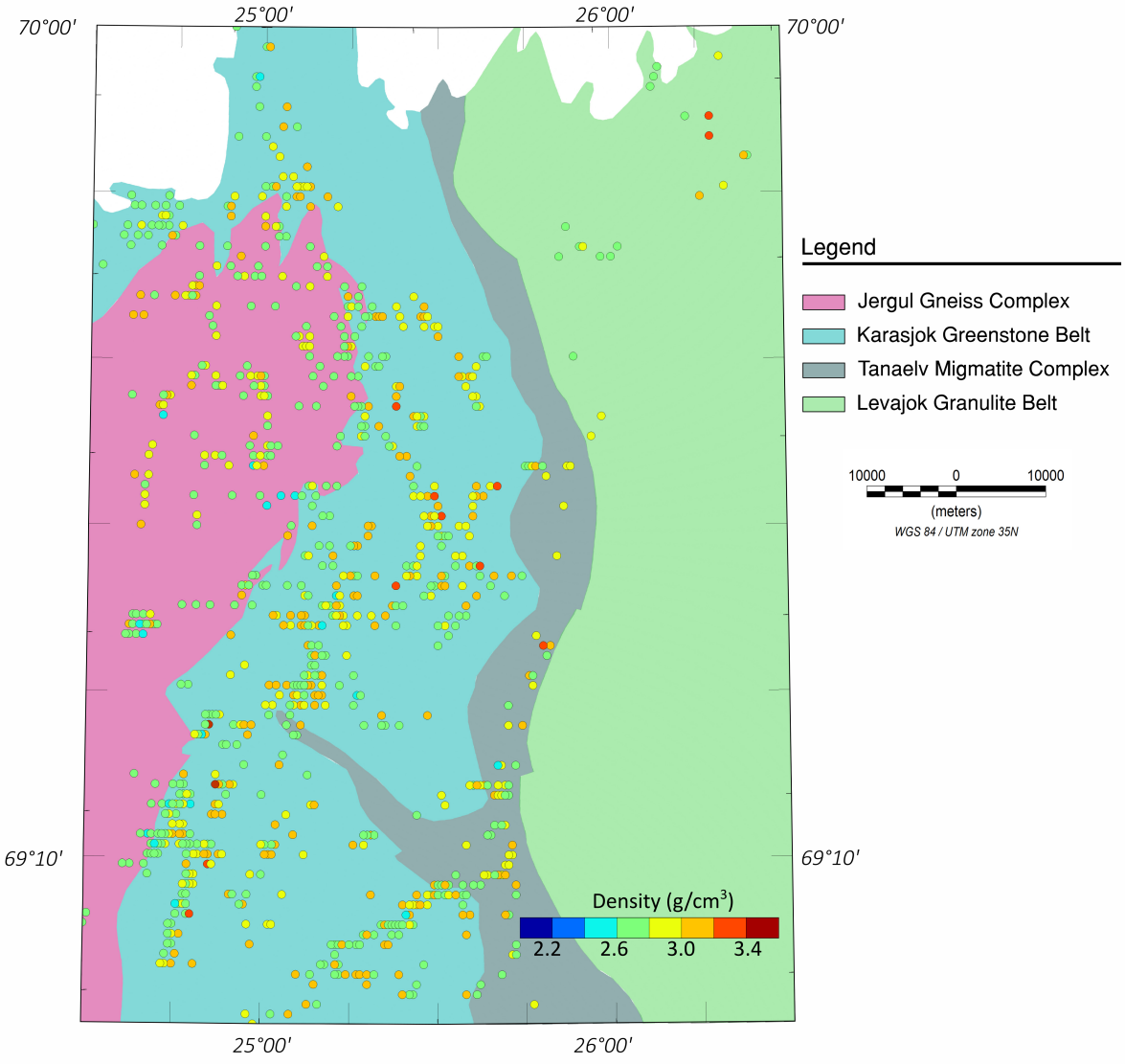

Figure 6.8: Simplified lithology map of Finnmarksvidda and the locations of rock samples.

6.5 Previous geophysical interpretation

To understand the crustal architecture, a 3D model (Figure 6.9) covering of the survey area was built by Skaar (2014) in IGMAS+ (Götze et al., 2007). The model was built using the high-resolution AGG data, new geological field observations, and petrophysical data. Also, since the KGB is a north-trending continuation of the Central Lapland Greenstone Belt (CLGB) in Finland, studies by analogy with the structures of CLGB were also used to constrain the modeling procedure (Nilsson et al., 2015; Skaar, 2014). The model includes 24 vertical cross-sections, intersecting the main trend of the greenstone belt. The distance between the cross-section varied between 1.5 km to 500 m, based on the complexity of the geological structures (Skaar, 2014).

The modeled fields from the 3D model are shown in Figure 6.10. According to Figure 6.10, the model generally fits the data. However, some short-wavelength features are clearly missing, which, to some degree, sacrifices the overall resolution of the high-resolution AGG data. More importantly, the details are believed to be associated with information which may be helpful to reveal some potential mineral deposits. One plausible explanation for that problem is that in the model geological unit has only one density despite the fact that density usually varies spatially. The simplification reduces the overall resolution of the model, which leads to the difficulty in explaining the short-wavelength signals. In this case, the key is to get proper density distributions for the geological units, which is a typical geophysical inverse problem.

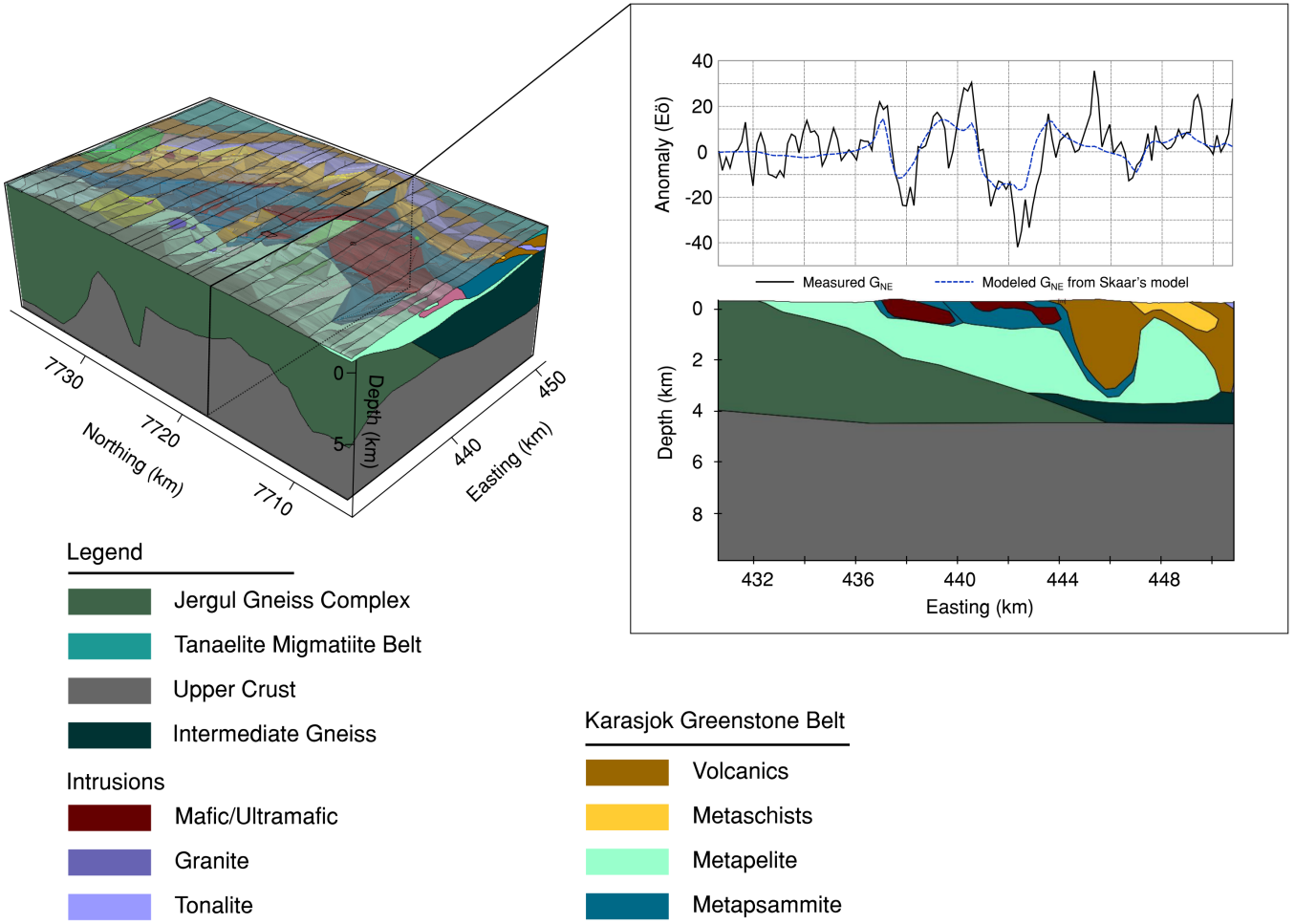

Figure 6.9: The prior lithology model of the survey area (Skaar, 2014) and a comparison between the measured $\mathbf{G}_{\mathrm{NE}}$ and the modeled $\mathbf{G}_{\mathrm{NE}}$ computed from the Skaar's model in IGMAS+. IGMAS+ computes modeled fields only using density contrasts which are derived from subtracting a use-defined reference density. The reference density is 2.67 g/cm^3. The cross-section is at Northing = 7718700 m.

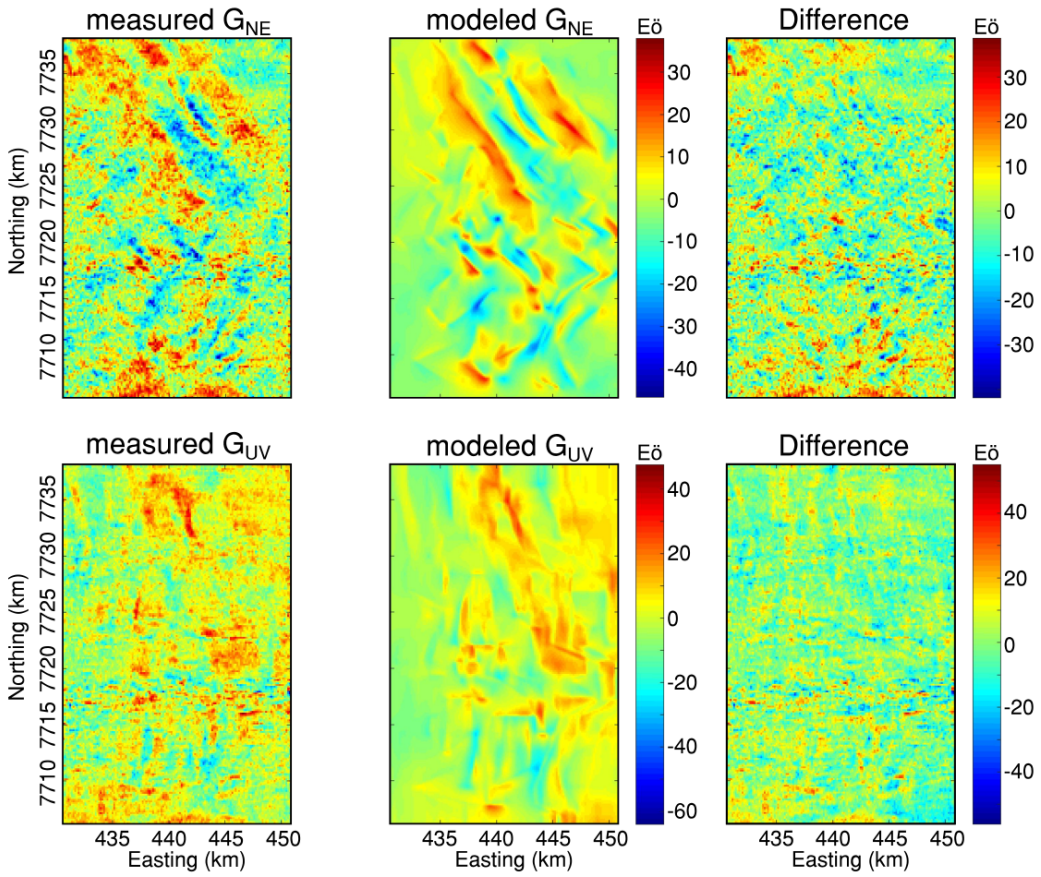

Figure 6.10: Comparison between the measured data and the modeled data derived from Skaar's lithology model along with their corresponding difference. The modeled fields are computed in IGMAS+. Since the IGMAS+ automatically subtracts the reference density (2.67 g/cm^3) from the model densities, so no significant terrain effects are detected in the modeled data.

6.6 Voxel model

For the inversion, the prior model in IGMAS+ has to be discretized into a voxel model. The area of the voxel model is identical with the survey area outlined in Figure 6.2. As a result of the low-pass filtering, the maximum resolution of the measured data is 150 m, which means that the data are only able to detect sources larger than 150 m (Dransfield and Christensen, 2013). For that reason, the dimension of a single cell in the voxel model is 150 m × 150 m × 150 m. The model is discretized into 213×135×23 voxels in total. It is noteworthy that the topography is also built into the voxel model. Therefore, the reference density is 2.67 g/cm^3, which is identical to the density value used for the terrain correction.

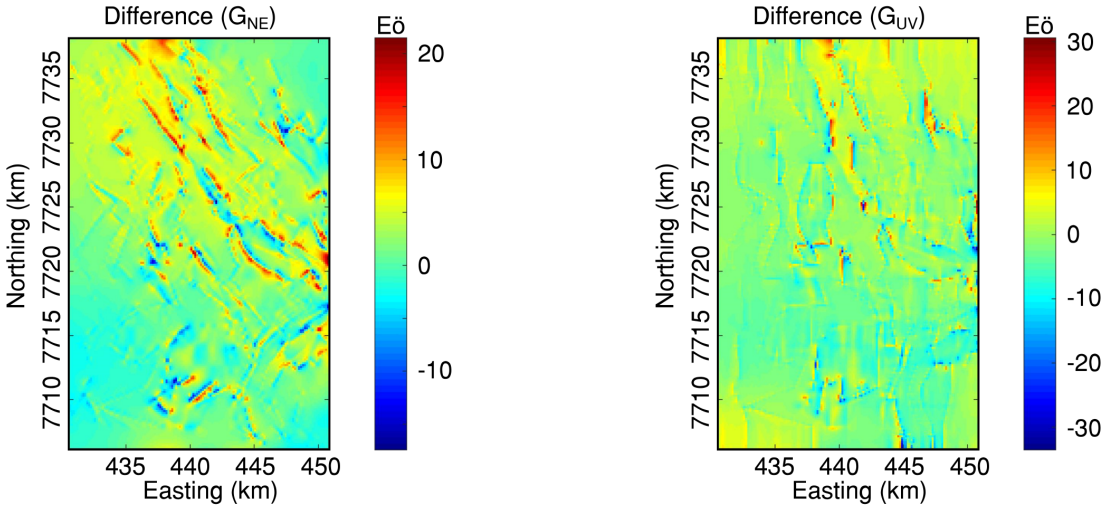

Figure 6.11: The difference between the modeled fields derived from the original Skaar's model displayed in Figure 6.9 (computed in IGMAS+) and the modeled fields derived from the the voxel model displayed in Figure 6.12 (computed in GeoModeller). For the comparison, the two models adopt the same density configuration as Skaar used for his modeling shown in Table 6.1.

Skaar (2014) states that the Karasjok Greenstone Belt is rather shallow and only up to 3 km deep and the shallower part makes the great contribution to the gravity gradients. Additionally, the gravity gradient data are more sensitive to shallow, small structures (Paoletti et al., 2016). Figure 6.11 shows the difference caused by the discretization and exclusion of the deeper part of the prior model. Therefore, we use only the top 2.95 km

volume of the model for our inversion (Figure 6.12).

Based on the samples and geographic locations at which the samples were taken, we have retrieved the statistics for each geological unit. After statistical analysis, the rocks in the Karasjok Greenstone Belt fall into 13 categories (For more details, see Table 6.1). There are 13 geological units in total. Each geological unit of the model has its own density distribution (Figure 6.13).

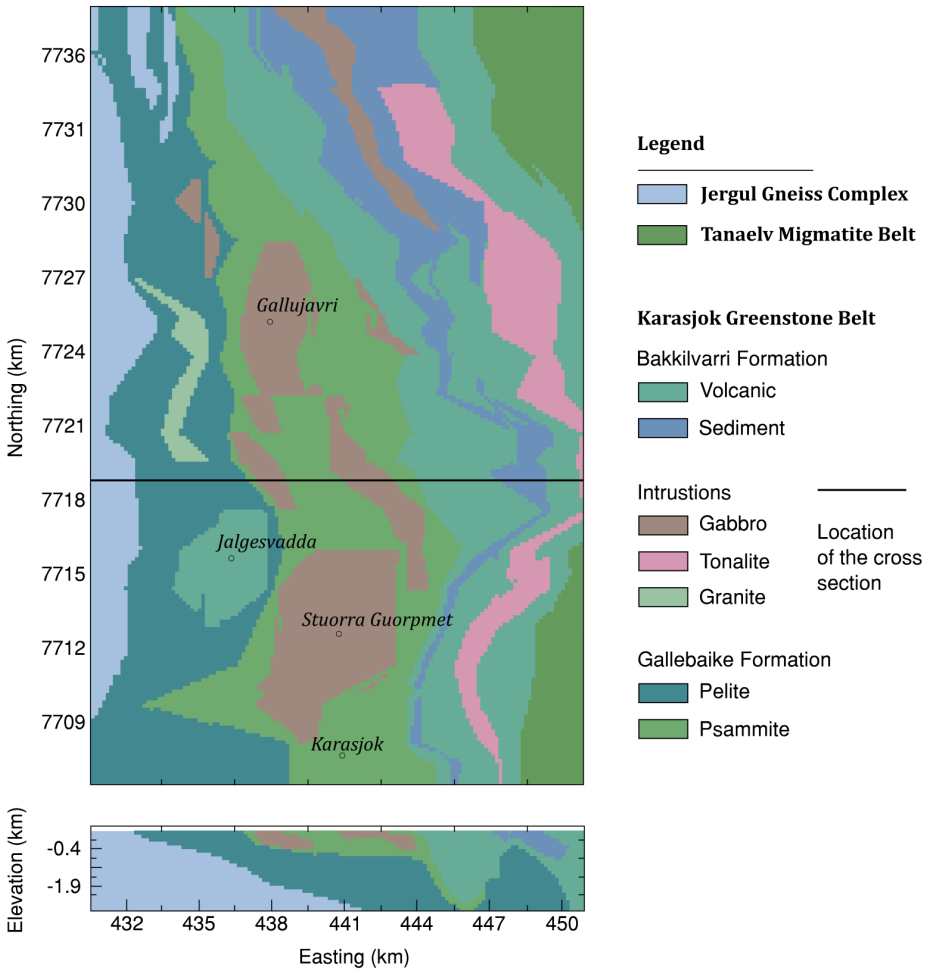

Figure 6.12: The discretized lithology model up to depth of 2.95 km, generated by IGMAS+. The cross-section is at Northing = 7718700 m.

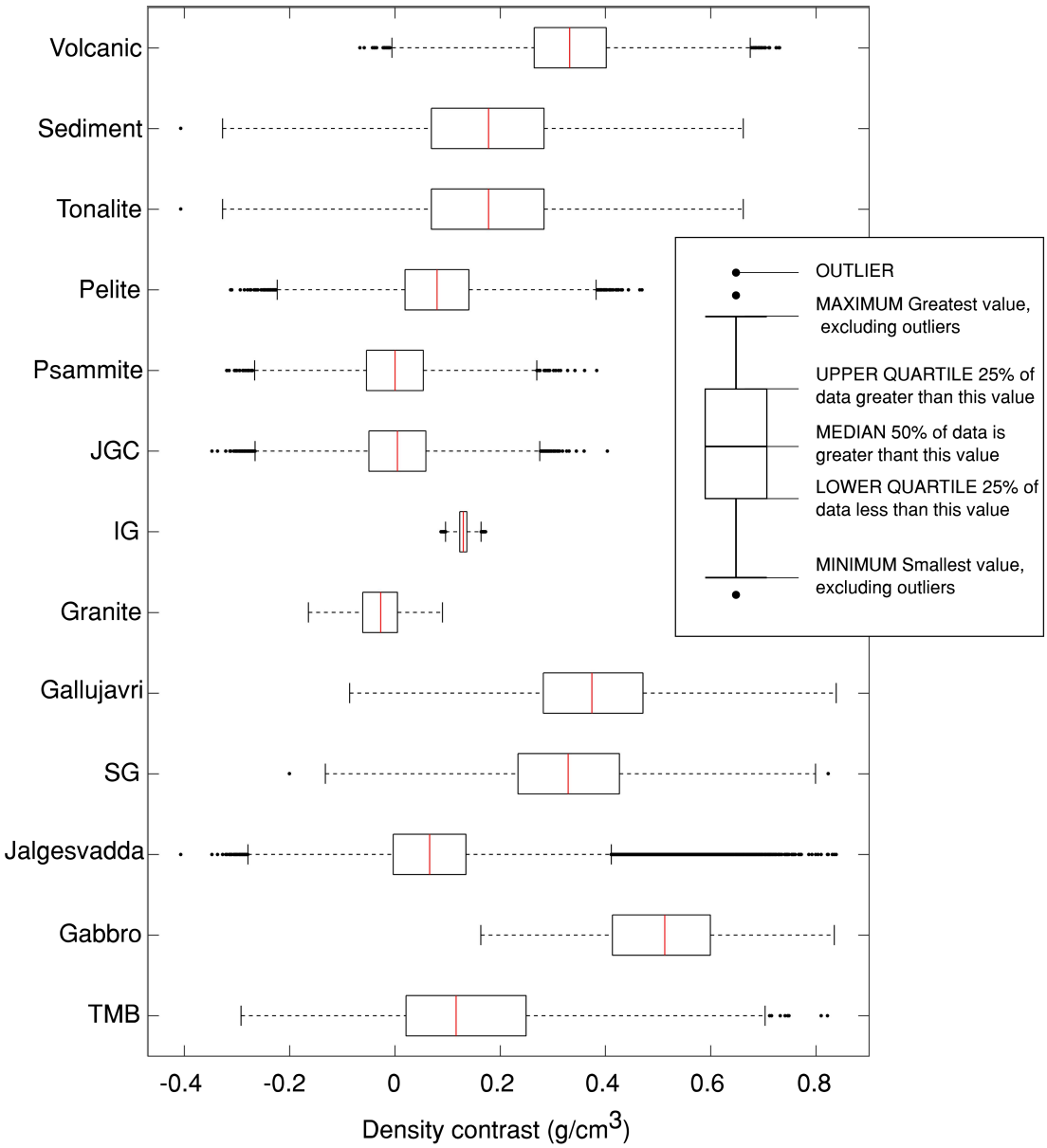

Figure 6.13: Box plot of density distributions of the geological units in the Karasjok Greenstone Belt. JGC, IG, SG, and TMB stand for Jergul Gneiss Complex (JGC), Intermediate Gneiss (IG), Stuorra Guorpmet (SG), and Tanaelv Migmatite Complex (TMB), respectively. The reference density is 2.67 g/cm^3. Figure 6.13 is equivalent to the prior density distribution summarized in Table 6.1.

Geological Unit	Min	Mean Density	Standard deviation	Max	Skaar's Modeling		Prior Density distribution for Stoachsitc Inversion	
					Lithologies	Modeling Density	Geological Unit	Density Distribution
Jergul Gneiss Complex n=278	2.520	2.675	0.075	2.981	Jergul Gneiss Complex	2.675	Jergul Gneiss Complex	$N(2.675, 0.075^2)$
Gallebaiki					Gallebaiki		Gallebaiki	
Amphibolite n=126	2.572	2.927	0.130	3.160	Volcanics	2.940	Jalgesvadda	$N(2.927, 0.130^2)$
Metapsammite n=101	2.510	2.670	0.077	3.170	Metapsammites	2.650~2.700	Psammite	$N(2.670, 0.077^2)$
Pelite n=100	2.580	2.749	0.090	3.072	Metapelites	2.750	Pelite	$N(2.749, 0.090^2)$
Bakkilivarri					Bakkilivarri		Bakkilivarri	
Amphibolite n=176	2.720	3.016	0.098	3.400	Volcanics	2.950~2.960	Volcanic	$80\%\times N(3.016, 0.098^2)$ $+20\%\times N(2.981, 0.090^2)$
Kommatiite n=97	2.711	2.981	0.090	3.218				
Metasediment n=45	2.600	2.785	0.136	3.159	Metaschists	2.750	Sediment	$70\%\times N(2.785, 0.136^2)$ $+30\%\times N(2.981, 0.090^2)$
Tanaelv Migmatite Belt								
Acidic Gneiss n=76	2.570	2.717	0.099	3.051	Tanaelv Migmatite Belt	2.800	Tanaelv Migmatite Belt	$57\%\times N(2.717, 0.099^2)$ $+43\%\times N(2.939, 0.157^2)$
Mafic Gneiss n=57	2.664	2.939	0.157	3.636				
Intrusion					Intrusion		Intrusion	
Mafic n=66	2.650	3.007	0.137	3.224	Mafic/Ultramafic	2.980~3.150	Gabbro	$N(3.007, 0.137^2)$
							Stuorra Guorpme	$N(3.007, 0.137^2)$
Ultramafic n=55	2.769	2.996	0.141	3.330			Gallujavri	$70\%\times N(3.007, 0.137^2)$ $+30\%\times N(2.996, 0.141^2)$
Felsic n=46	2.580	2.669	0.047	2.781	Granite	2.640	Granite	$N(2.640, 0.047^2)$
Unit: g/cm^3					Tonalite	2.700~2.770	Tonalite	$N(2.730, 0.050^2)$
					Thrusted basement	2.700		
					Intermediate Gneiss	2.800	Intermediate Gneiss	$N(2.800, 0.010^2)$

Table 6.1: Summary of the measured rock samples (Midtun, 1988; Skaar, 2014), the densities used in the 3D modeling (Skaar, 2014), and the prior statistical model of each geologic unit in KGB. $N(\mu, \sigma^2)$ denotes a normal distribution with a mean of μ and a standard deviation of σ. The percentage is used to describe a multimodal distribution, such as a bimodal (two peaks).

6.7 Inversion

6.7.1 Inversion specifications

To retrieve density distribution of the survey area and to examine the influence of the noise reduction on inversion as well as the usefulness of various combinations of gravity gradient tensor component, seven different combinations of the AGG components are selected for inversion. The combinations includes

- **2C**$_{\mathrm{m}}$ (m here stands for measured): two-component inversion of the measured $\mathbf{G}_{\mathrm{NE}}$ and $\mathbf{G}_{\mathrm{UV}}$ considered appropriate for use in inversion (Fugro Data Processing Report, 2011)
- **2C**$_{\mathrm{r}}$ (r here stands for reduced): two-component inversion of the noise-reduced $\mathbf{G}_{\mathrm{NE}}$ and $\mathbf{G}_{\mathrm{UV}}$ demonstrated in Chapter 4;
- **1C**: one-component inversion of the constructed $\mathbf{G}_{\mathrm{DD}}$ (abbreviated as 1C), the most commonly used gravity gradient tensor components;
- **2C**: two-component inversion of the constructed $\mathbf{G}_{\mathrm{NE}}$ and $\mathbf{G}_{\mathrm{UV}}$, having a certain advantage in delineating some subsurface structures in deterministic inversion suggested by Pilkington (2012),
- **3C**: three-component inversion of the constructed $\mathbf{G}_{\mathrm{NE}}$, $\mathbf{G}_{\mathrm{UV}}$, and $\mathbf{G}_{\mathrm{DD}}$, the vertical component included to improve the vertical resolution;
- **5C**: five-component inversion of the constructed $\mathbf{G}_{\mathrm{NN}}$, $\mathbf{G}_{\mathrm{EN}}$, $\mathbf{G}_{\mathrm{ND}}$, $\mathbf{G}_{\mathrm{EE}}$, and $\mathbf{G}_{\mathrm{ED}}$;
- **6C**: six-component inversion of the constructed $\mathbf{G}_{\mathrm{NN}}$, $\mathbf{G}_{\mathrm{EN}}$, $\mathbf{G}_{\mathrm{ND}}$, $\mathbf{G}_{\mathrm{EE}}$, and $\mathbf{G}_{\mathrm{ED}}$, and $\mathbf{G}_{\mathrm{DD}}$.

Additionally, the prior density distributions shown in Figure 6.13 and the discretized lithology model shown in Figure 6.12 are inputs for the inversion. Every inversion will run 10 million times in GeoModeller 3.3. Additionally, it is important to point out that the geological units in our inversion are configured to be fixed and not allowed to be altered.

6.7.2 Evaluating the reliability of the inversions

Since the beginning of the Bayesian inversion is highly influenced by the starting model, the determination in search for a point where the misfit not significantly improves has been established for retrieval of the statistics of the realizations, such as an arithmetic mean (called mean model in the paper) and a standard deviation (Geyer, 2011). It also indicates that stochastic inversion is not dependent on density values of the staring model. In other words, results of stochastic inversion are only determined by the input property laws and the input lithology model. Following the rule of thumb, we retrieved all the statistics from the seven inversion setups.

We calculated misfits between the input data and the predicted data from the mean models as shown in Figure 6.14 and Table 6.2. Compared to the initial misfits, the misfits after the inversion have been significantly minimized. Owing to the inevitable presence of noise in dynamic measuring environment and the limited instrumental resolution (Dransfield and Christensen, 2013), there are always misfits, especially when more than two components are involved. Because the inconsistency between different components cannot be easily recognized in one-component inversion (Martinez et al., 2013). The estimated intrinsic noise levels provided by Fugro Geosciences for the $\mathbf{G}_{\mathrm{NE}}$ and $\mathbf{G}_{\mathrm{UV}}$ are 3.71 and 3.58 Eö, respectively, so the misfits greater than the noise levels are expected. Nevertheless, the short-wavelength information missing in the model by Skaar (2014) has been recovered in the resolved mean models.

Together with the misfits, it is also critical to examine the dispersion or the standard deviation of the accepted realizations in the stochastic inversions. Because the standard deviation can help us understand if a retrieved mean model is able to reliably represent an ensemble of accepted realizations. A small standard deviation is invariably desirable. Because our prior model is a 3D model including 661365 voxels, we only provide the statistics of the standard deviations derived from the seven inversions. The small standard deviations in Table 6.3 pinpoint that the retrieved mean models are reliable from a statistical perspective.

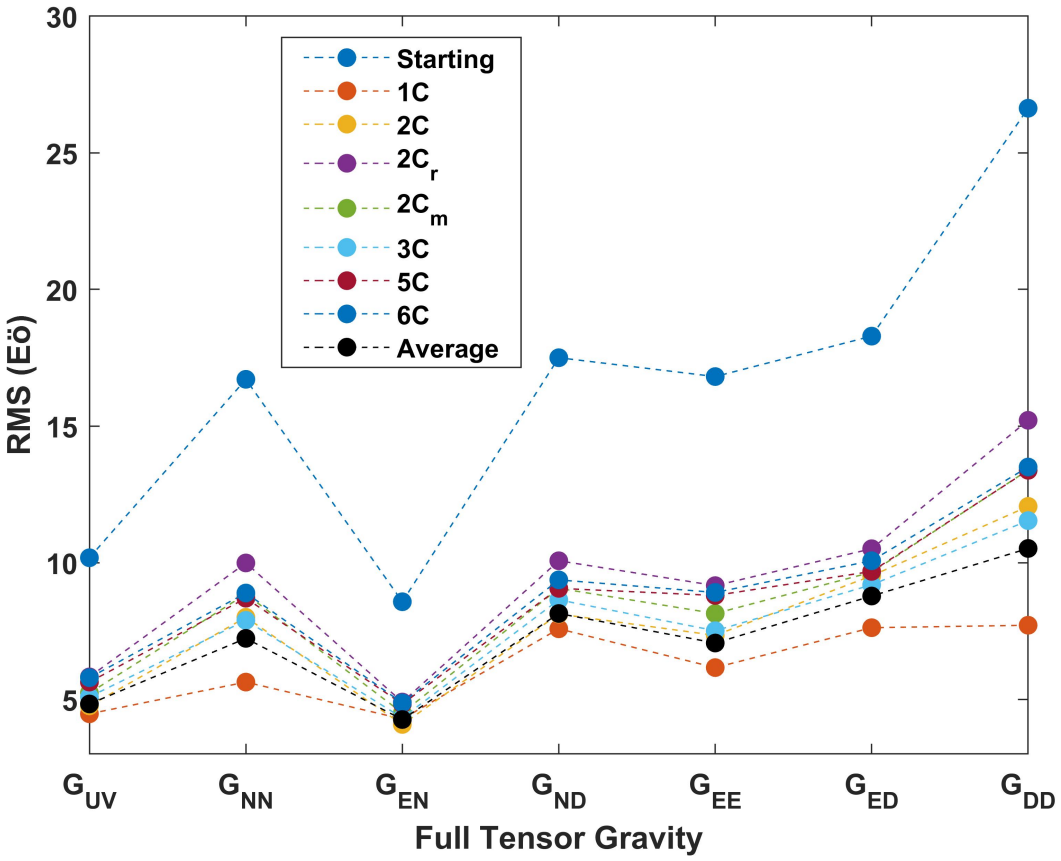

Figure 6.14: The RMS misfits between the input data and the predicted data are calculated in terms of the gravity gradient tensor components.

	$\mathbf{G}_{UV}$	$\mathbf{G}_{NN}$	$\mathbf{G}_{EN}$	$\mathbf{G}_{ND}$	$\mathbf{G}_{EE}$	$\mathbf{G}_{ED}$	$\mathbf{G}_{DD}$
Initial	10.18	16.71	8.57	17.50	16.81	18.29	26.63
1C inversion	4.47	5.63	4.28	7.85	6.16	7.62	7.71
2C inversion	4.76	8.00	4.08	8.12	7.34	9.52	12.06
$2C_r$ inversion	5.82	9.99	4.90	10.07	9.16	10.51	15.21
$2C_m$ inversion	5.23	8.85	4.50	9.06	8.14	9.65	13.39
3C inversion	5.09	7.89	4.32	8.64	7.51	9.19	11.54
5C inversion	5.63	8.70	4.83	9.06	8.80	9.68	13.38
6C inversion	5.79	8.89	4.87	9.37	8.91	10.07	13.50
The average model	4.83	7.23	4.26	8.14	7.06	8.78	10.52

Table 6.2: The root mean square (RMS) misfits in Eö between the input data and the predicted data for the six scenarios in terms of the gravity gradient tensor components. Shading denotes the components involved in the inversion. The resolved mean models were used to calculate the predicted data. Regarding the $2C_m$ inversion, the misfits of $\mathbf{G}_{NE}$ were calculated between the constructed $\mathbf{G}_{NE}$ and the predicted $\mathbf{G}_{NE}$. So were the misfits of $\mathbf{G}_{UV}$.

	Mean	STD	RMS	Per cent of cells
	[g/cm^3]	[g/cm^3]	[g/cm^3]	[≥ 0.01]
1C inversion	0.0015	0.0031	0.0034	2.55%
2C inversion	0.0008	0.0020	0.0022	0.92%
$2C_r$ inversion	0.0014	0.0028	0.0031	1.93%
$2C_m$ inversion	0.0006	0.0017	0.0018	0.55%
3C inversion	0.0003	0.0010	0.0011	0.18%
5C inversion	0.0002	0.0009	0.0009	0.11%
6C inversion	0.0002	0.0008	0.0008	0.09%

Table 6.3: The standard deviations of the accepted realizations (density models) derived from all the inversions. Specifically, the last column gives the proportion of the extreme values in the standard deviation less 1 per cent out of 626498 voxels (661365 voxels in total but 34865 voxels are used for volume caused by the terrain and cannot be modified in the inversion).

6.7.3 The $2C_m$ and the $2C_r$ inversion

The new noise reduction method has effectively reduced the noise levels of the measured $\mathbf{G}_{NE}$ and $\mathbf{G}_{UV}$. It has been demonstrated that noise up to around 3.4 Eö has been filtered. According to the profiles in Figure 6.15, in general, the amplitude of the reduced $\mathbf{G}_{NE}$ is smaller than that of the measured $\mathbf{G}_{NE}$. However, the predicted $\mathbf{G}_{NE}$ from the $2C_r$ inversion is virtually analogous to the one from $2C_m$ inversion regarding the amplitude and the shape. The observation indicates that the prior noise reduction hardly plays a significant role in the inversion. Also, the similar predicted data may lead to similar resultant density models.

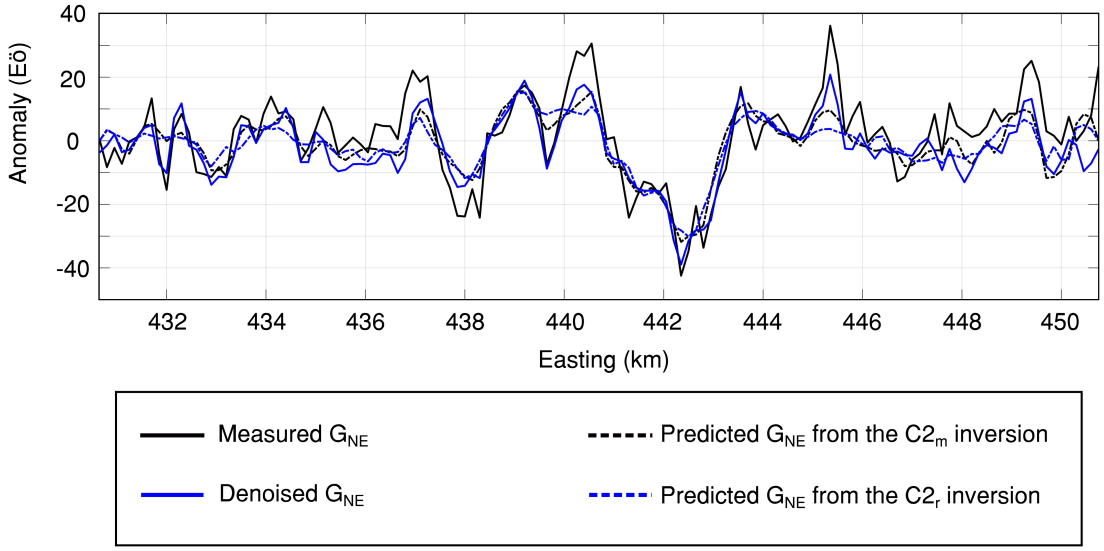

Figure 6.15: Profiles of the measured $\mathbf{G}_{NE}$, the noise-reduced $\mathbf{G}_{NE}$, and the predicted $\mathbf{G}_{NE}$ from the resolved mean models, which are extracted at Northing = 7718700 m.

We took cross-sections intersecting the North-South trend of KGB. The first cross-section from the top in Figure 6.16 is extracted from the starting model for reference, of which density values are randomly generated by the software according the pre-defined density distributions. The second cross-section (Figure 6.16b) is taken from the mean model derived from the $2C_m$ inversion of the measured $\mathbf{G}_{NE}$ and $\mathbf{G}_{UV}$, whereas the third cross-section is taken from the mean model derived from the $2C_r$ inversion of the noise-reduced $\mathbf{G}_{NE}$ and $\mathbf{G}_{UV}$.

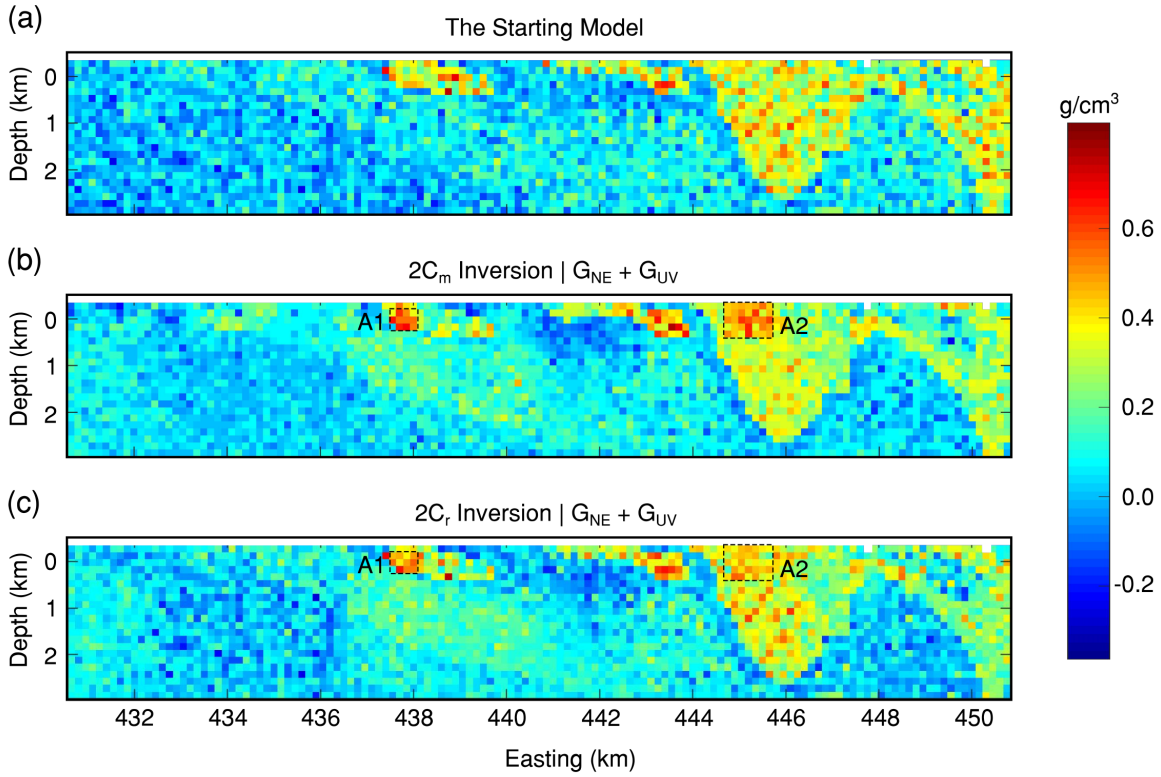

Figure 6.16: Display of a cross-section from the starting density model (a) and cross-sections extracted from the resolved mean models derived from, (b) the $2C_m$ inversion with the measured $\mathbf{G}_{NE}$ and $\mathbf{G}_{UV}$ as the inputs; (c) the $2C_r$ inversion with the noise-reduced $\mathbf{G}_{NE}$ and $\mathbf{G}_{UV}$ as the inputs. Density values of the starting model are automatically assigned according to the input density distributions by the software during the initialization of the inversion. And the cross-sections are extracted at Northing = 7718700 m.

The density values in the first cross-section in Figure 6.16a show basically no patterns. After the inversions, some patterns have started emerging. In general, the two cross-sections as shown in the lower panel are comparable, although the cross-sections appear to be visually coarse. The both inversions are able to reveal A1 and A2 high-density anomalies up to 0.6 g/cm^3. Especially, the A2 is distinctively higher than the average density contrast (0.3 g/cm^3) of the Bakkilvarri Formation (see Figure 6.13). The reason that the results are virtually identical might be because the noise-levels of the two measured components are already too low to influence the inversion in a significant manner, which leads to the general resemblance between the two cross-sections. Additionally, it also may be because the inversion process itself works like a band-pass filter and rejects the incom-

patible contents in the data, which is also the reason that equivalent source technique can be used for noise reduction (Martinez and Li, 2016). However, the A2 in the third cross-section does not appear as distinct as the one in the second cross-section. It may be because the high-frequency signals associated to this anomaly have been filtered by the noise reduction method. It also happens to the A1. As a consequence, noise-reduction should be carefully made. We recommend to start inversion with the measured data in the first place.

6.7.4 The $2C_m$ and the 2C inversion

We pointed out in the previous section that the measured data and the constructed data have nearly 5 Eö difference in total. According to the profiles in Figure 6.17, the predicted $\mathbf{G}_{\mathrm{NE}}$ from the C2 inversion and the $C2_m$ inversion, however, seems much closer to the constructed $\mathbf{G}_{\mathrm{NE}}$ than the measured $\mathbf{G}_{\mathrm{NE}}$, in terms of the amplitude and the shape. This indicates that whether the measured $\mathbf{G}_{\mathrm{NE}}$ or the constructed $\mathbf{G}_{\mathrm{NE}}$ is used for inversion, the predicted $\mathbf{G}_{\mathrm{NE}}$ tend to resemble the constructed $\mathbf{G}_{\mathrm{NE}}$. Likewise, the results of the inversion are also probably comparable.

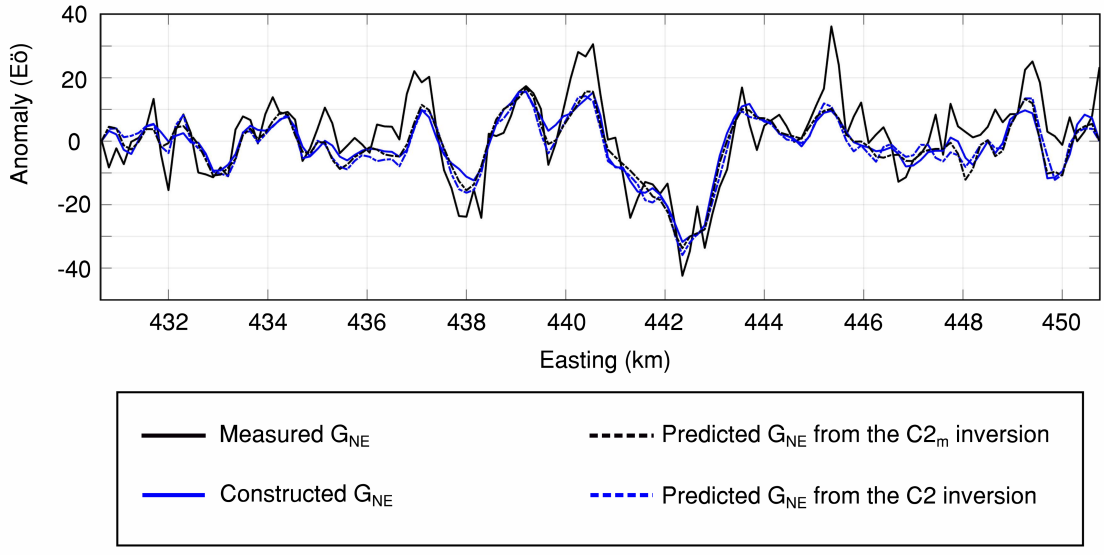

Figure 6.17: Profiles of the measured $\mathbf{G}_{\mathrm{NE}}$, the constructed $\mathbf{G}_{\mathrm{NE}}$, and the predicted $\mathbf{G}_{\mathrm{NE}}$ from the resolved mean models, which are extracted at Northing = 7718700 m.

The first cross-section from the top in Figure 6.18 is extracted from the starting model for reference as well. The second cross-section (Figure 6.18b) is taken from the

mean model derived from the $2C_m$ inversion of the measured $\mathbf{G}_{NE}$ and $\mathbf{G}_{UV}$, whereas the third cross-section is taken from the mean model derived from the 2C inversion of the constructed $\mathbf{G}_{NE}$ and $\mathbf{G}_{UV}$.

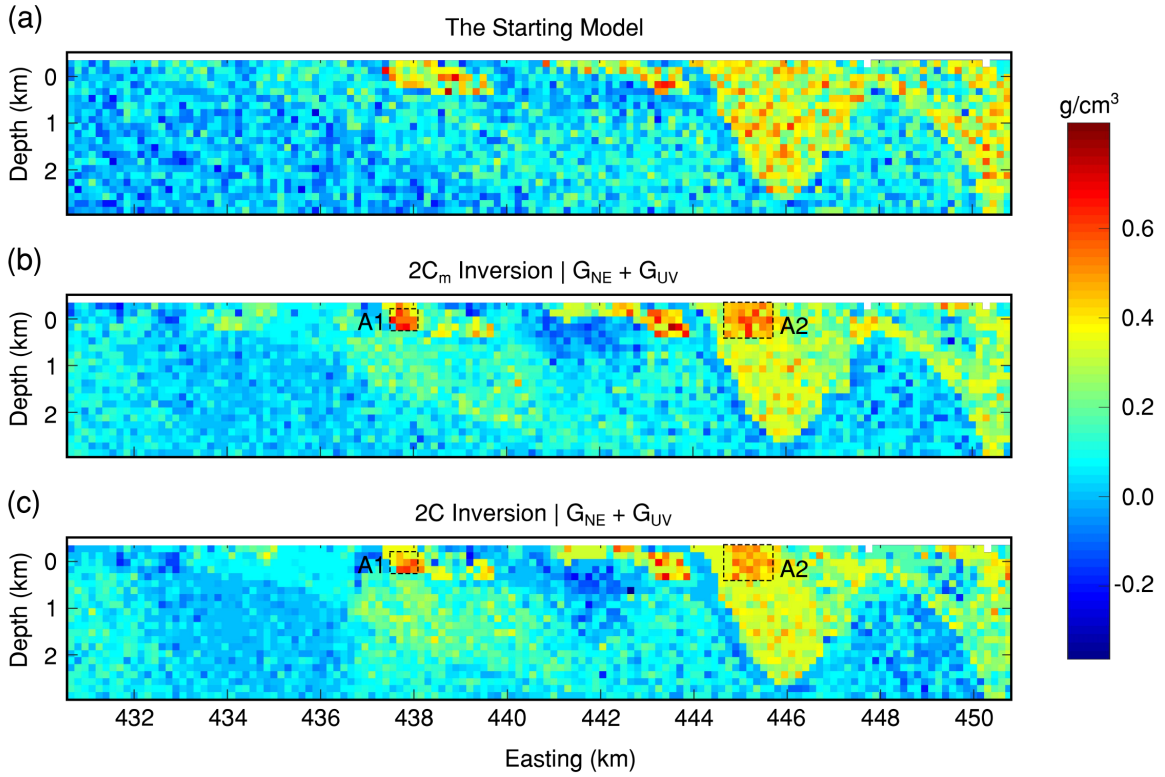

Figure 6.18: Display of a cross-section from the starting density model (a) and cross-sections extracted from the resolved mean models derived from, (b) the $2C_m$ inversion with the measured $\mathbf{G}_{NE}$ and $\mathbf{G}_{UV}$ as the inputs; (c) the 2C inversion with the constructed $\mathbf{G}_{NE}$ and $\mathbf{G}_{UV}$ as the inputs. Density values of the starting model are automatically assigned according to the input density distributions by the software during the initialization of the inversion. And the cross-sections are extracted at Northing = 7718700 m.

The major trend of the cross-sections in shown in the lower panel in Figure 6.18 is similar. The both inversions are able to reveal A1 and A2 high-density anomalies as well. Since the results are virtually identical, it indicates that the measured data and the constructed data can equally serve the purpose of inversion. On the other hand, it has been demonstrated that the difference between the measured components and the constructed components hardly affects the results of the inversion in our case. It is noteworthy that due to the fact that the noise levels of the measured components and the

constructed components are not identical and the latter is especially difficult to estimate, the measured data and constructed data should not be mixed as inputs of inversion. Additionally, the full tensor gravity can be only obtained with the construction process.

6.7.5 The multi-component inversions of the constructed GGT

According to the profiles in Figure 6.19, the predicted $\mathbf{G}_{\mathrm{NE}}$ from the inversions of the constructed data is also visually closer to the constructed $\mathbf{G}_{\mathrm{NE}}$ than the measured $\mathbf{G}_{\mathrm{NE}}$, like profiles in Figure 6.17. It further demonstrates that the 5 Eö difference due to the construction process did not influence the predicted data in a significant way.

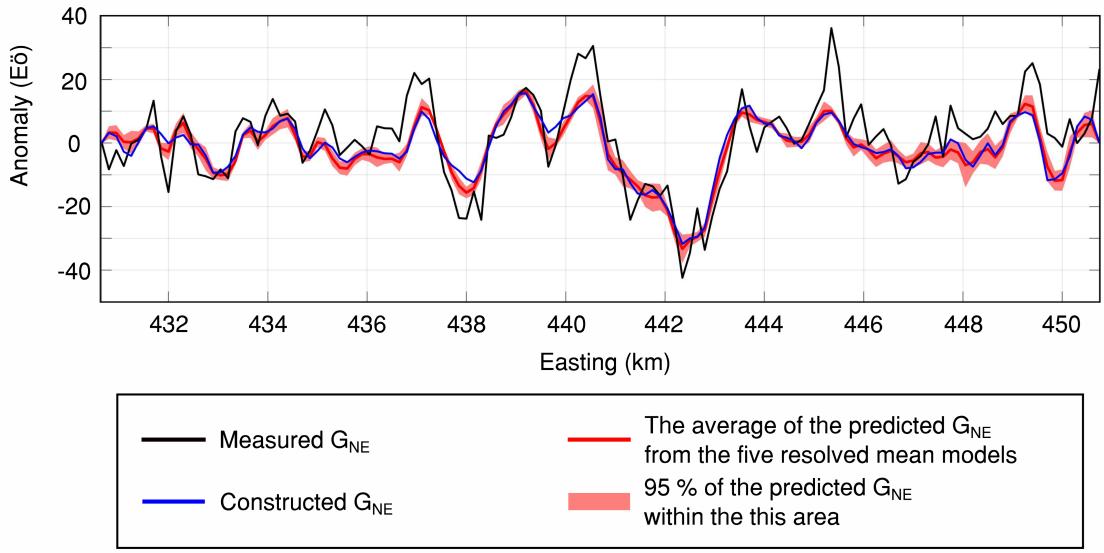

Figure 6.19: Profiles of the measured data, the constructed data, and the predicted data from the resolved mean models, which are extracted at Northing = 7718700 m.

With an increase of the input components, the cross-sections are getting more and more similar. Especially, the results from the 5C inversion and 6C inversion (Figure 6.20d and e) are almost indistinguishable. For example, density anomalies A1, A2, A3 have been revealed in the same location in the two cross-sections. Also, their corresponding misfit curves (Figure 6.14) are almost similar as well. It means that the inclusion of the extra $\mathbf{G}_{\mathrm{DD}}$ basically makes no significant contribution to the result of the 6C inversion but increases the computation complexity. In this case, the 6C inversion has relatively lower cost-effectiveness.

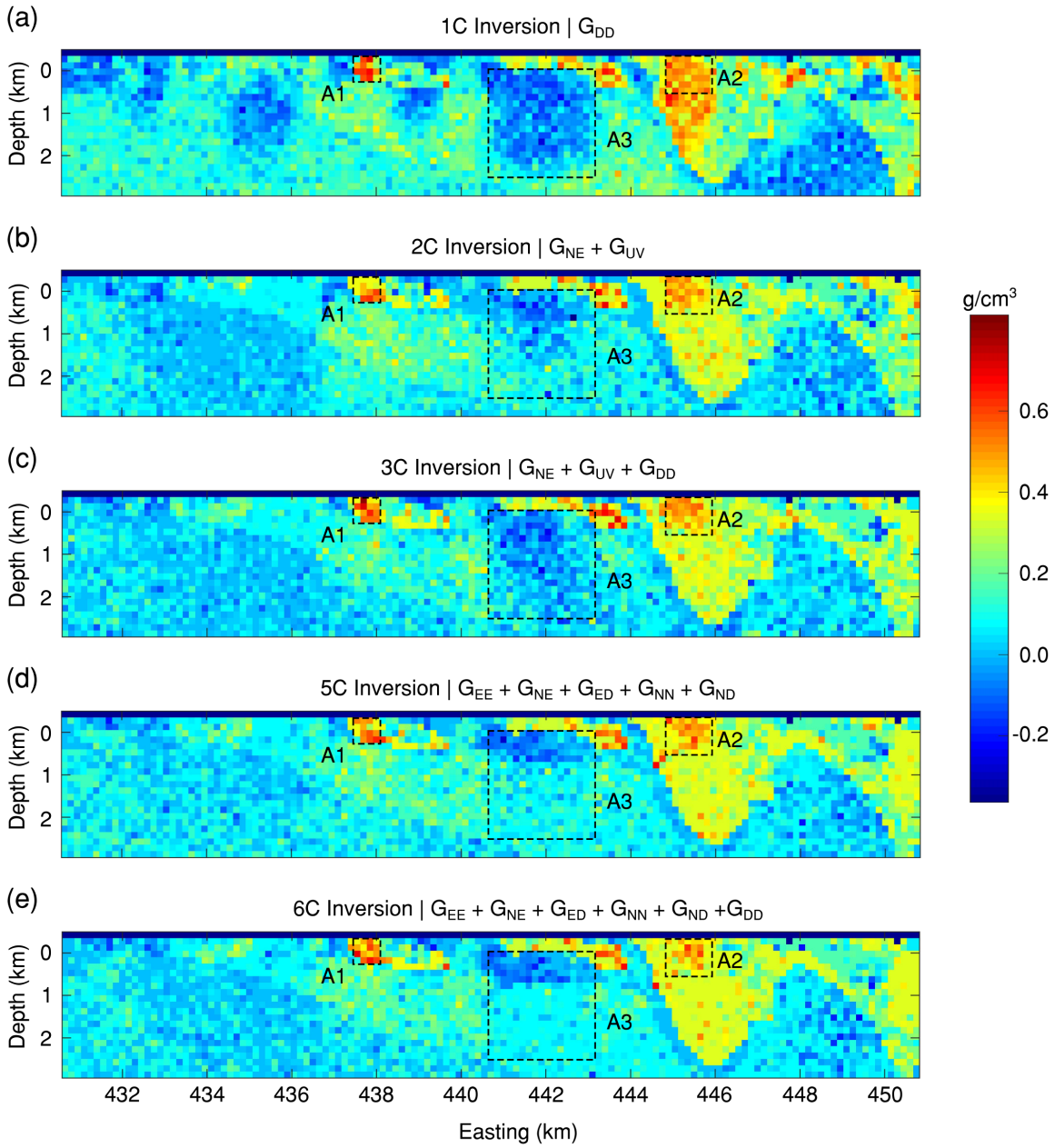

Figure 6.20: Display of five cross-sections extracted from acquired mean models by inverting the five different combinations of the constructed gravity gradient tensor components, (a) from the 1C inversion; (b) from the 2C inversion; (c) from the 3C inversion; (d) from the 5C inversion and (e) from the 6C inversion. The cross-sections are extracted at Northing = 7718700 m.

Regarding the 3C inversion, the result of the 3C inversion is generally comparable with the result of the 5C inversion (Figure 6.20). Interestingly, there is noticeable difference in the A3 region. It seems like that the 3C inversion provides improved depth sensitivity. In comparison with the corresponding misfit curve of the 5C inversion, more than 1 Eö information across the full tensor gravity has been mapped into the mean density model of the 3C inversion. It also indicates that the difficulty in fitting observed data may lead to the loss of some important information in the resolved density model. In this case, including $\mathbf{G}_{\mathrm{ED}}$ and $\mathbf{G}_{\mathrm{ND}}$ in the 5C inversion hardly delivers equally acceptable results. Apparently, the 3C inversion outperforms the 5C inversion and the 6C inversion as well. It further demonstrates that inverting extra six or five components does not necessarily improve the results in our case.

In comparison with the result of the 2C inversion, the result of 3C inversion shows exceptional depth sensitivity in the A3 region as well due to the extra information provided by the $\mathbf{G}_{\mathrm{DD}}$ component. Normally, with an increase of tensor components involved in inversion, it gets more and more difficult in fitting observed data, which leads to less information translated into resolved density models. On the contrary, the misfits of the $\mathbf{G}_{\mathrm{DD}}$ have been further reduced, which cannot be found in other scenarios (Table 6.2). Moreover, the nearly identical misfit curves of the 2C and 3C inversion (Figure 6.14) imply that the inclusion of extra $\mathbf{G}_{\mathrm{DD}}$ barely increases the difficulty in fitting the observed data in a significant way. With the help of $\mathbf{G}_{\mathrm{DD}}$, the depth sensitivity of the 3C inversion has improved in comparison with the 2C inversion.

Concerting the 1C inversion, the A1, A2, and A3 density anomalies which are found in other cross-sections have also been revealed. But there are also some patterns which cannot be detected in other cross-sections. Since the inconsistency between components cannot be easily identified in one-component inversion, it explains why the 1C inversion provides the smallest misfits. Additionally, the lack of enough constraints in inversion can be problematic. It is also the reason that the cross-section from the 1C inversion looks a bit different from the rest.

Since we have seven resolved mean models derived from the inversions, we simply retrieve the average of the seven mean model. Because averaging out the seven mean models is equivalent to a weighted average of the all accepted density models in the seven inversions with different inputs. The weights are determined by the acceptance rates of the inversion, which is configured to be around 21% in accordance with the

appropriate acceptance rate proposed by (Geyer, 2011). This averaging process will lead to a more accurate density model than any one of the seven mean models. Additionally, it is widely accepted that the averaging process can, in principle, cancel out the part which is incomparable in the models and reinforce the common part which the mean models share. Regarding the misfit level, it is not surprising that the average model outperforms the multi-component inversions listed in Table 6.2.

Based on this premise, we calculate the RMS (root mean square) difference between the mean models and the average model. The difference is shown in Figure 6.21. Generally, the differences are acceptably small. However, according to the curve, the mean model from the 1C inversion is farthest away from the average model, whereas the mean model from the 6C inversion is the closest one, which is not surprising. The mean model from the C2 inversion is still a bit far from the average model compared to the one from the 3C inversion. After the 3C inversion, the curve seems to converge. It can be seen from the curve that two more components involved in the 5C and 6C inversion do not reduce the model difference as much as that due to $\mathbf{G}_{\mathrm{DD}}$ involved in the 3C inversion. In this sense, the 3C inversion is an appropriate approximation to the optimum solution regarding computation efficiency.

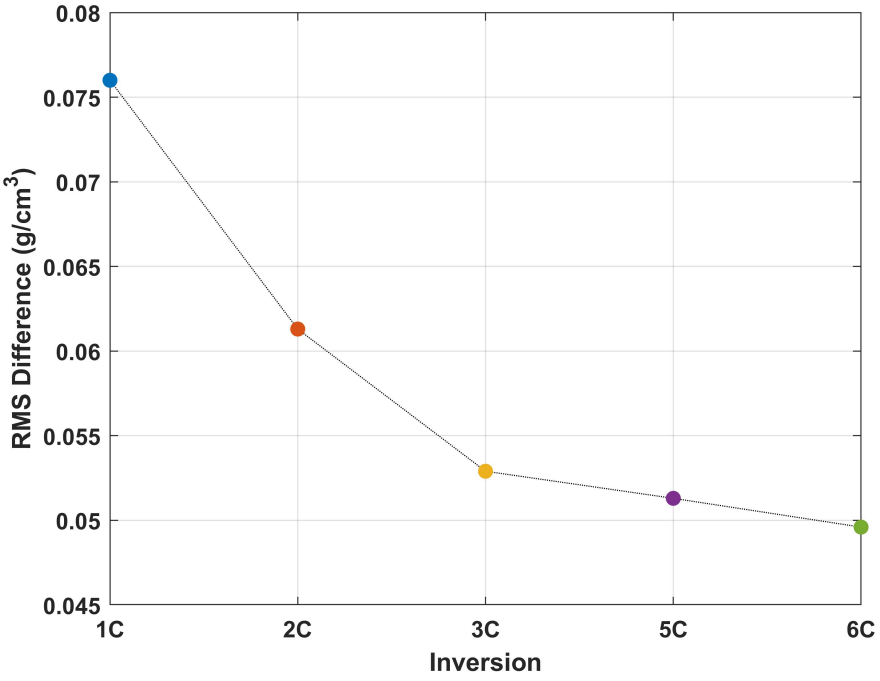

Figure 6.21: The RMS (root mean square) difference between the mean models and the average model.

6.7.6 Discussion

For starter, the prior noise reduction applied to the measured data does not improve the results. On the contrary, it causes some difficulty in delivering equally distinct result in comparison with the one without prior noise reduction. One plausible reason is that the noise reduction that has to be applied to the two measured components separately may have filtered some important information and introduced inconsistency. In our case, even the difference with the standard deviation of 5 Eö due to the construction process hardly influences the results of the inversion. As a consequence, unless existing noise in input data is significant enough to mask the real signals and does not follow zero-mean normal distributions, then it is not necessary to applied the noise reduction prior to the inversion. It is noteworthy that once the inconsistency is introduced, it is difficult to remove the inconsistency. Therefore, we recommend to start inversion with the measured data first. If the inversion results are not acceptable, then it is reasonable to consider to reduce the existing noise in the input data.

The fact that the differences which visually follow a normal distribution with a zero mean and standard deviations of up to 5 Eö due to the construction process barely impact the results of the inversion may be simply because the differences behave like zero-mean Gaussian noise. If the standard deviation is a bit greater and the mean is no more zero or the differences no longer follow normal distributions, the results might be completely different. Consequently, the conclusion is not universal and only valid in the setup described in the paper. A universal conclusion needs more thorough examination. Also, it does not necessarily mean that noise reduction is no longer useful. To the contrary, low-pass filtering makes a great contribution to the high signal-to-noise ratio of the AGG data.

Consider all the observed factors, the 3C component inversion is considered an acceptable compromise among the inversions in our case, in terms of the reliability and computation complexity. However, it does not necessarily mean that it is always the case. Moreover, with the help of $\mathbf{G}_{\mathrm{DD}}$, the depth sensitivity of the 3C inversion has been improved and yet only inverting $\mathbf{G}_{\mathrm{DD}}$ does not exert enough constraints on the 1C inversion. It means that the inclusion of $\mathbf{G}_{\mathrm{DD}}$ is useful to recover deep information. So $\mathbf{G}_{\mathrm{DD}}$ should be always included in inversion.

From the results, it can be easily noticed that the one-component inversion easily fits the observed data but may be problematic due to the lack of constraints and the

difficulty in fitting the observed data due to the multi-component inversion leads to less information being translated into resolved density models. Apparently, inversion of gravity gradient data is a trade-off between misfits and recovered information. Therefore, instead of inverting only one type of input data or one subset of FTG data to find a single optimum solution, we recommend to invert different combinations of gravity gradient components to retrieve an averaged solution from the acquired solutions. First of all, because non-uniqueness inheres in geophysical inverse problems. Second, because the averaged solution is relatively more reliable and stable from a statistical perspective.

6.8 Potential mineralization

For interpretation, all obtained information matters. Therefore, we simply just adopt the average model for the purpose.

The cross-sections and the plan view shown in Figure 6.22 were extracted from the average model. From the plan view (Figure 6.22), it can be seen that the Karasjok Greenstone Belt has a distinctively high-density region in the east and a comparatively low-density region in the west, which characterizes the Bakkilivarri Formation and Gallebaike Formation. Some small patterns with even higher density values which reside inside the unit "Volcanic" may be due to the presence of komatiites or gabbroic rocks, which are also indicated by its highly skewed right tail shown in Figure 6.23a. However, its proportion turns out to be smaller than it is assumed at the beginning. The unit "Sediment", a low-density region inside the "Volcanic" region, has a relatively smoother appearance, in agreement with its more focused density distribution (Figure 6.23b). The histogram of the unit "Sediment" also shows that its average density is even smaller than previously assumed. Besides, there are some other isolated high-density regions, which are due to either mafic or ultramafic intrusive rocks. According to the cross-sections (Figure 6.22), the structures with extra high densities are shallow and close to the surface. Besides, as for Pelite and Psammite in the Galliebaike Formation, their posterior density distributions basically conform to the prior density distributions but with less dispersions in respective density distribution.

We furthermore provide a volume-rendered image of the density contrast model (Figure 6.24a) computed from the average model. The area displays voxels with density contrast greater than 0.2 g/cm^3, which is the average density contrast of the amphibolite in this

region. Since KGB also abounds with komatiite and mafic/ultramafic rocks, the area in Figure 6.24a should be mainly made of amphibolite, komatiite and mafic/ultramafic rocks. Additionally, because the mafic/ultramafic rocks and komatiite are magnetic, the total magnetic intensity map is accompanied for comparison. The leveled total magnetic intensity was IGRF corrected using the 2010 model, 2011/08/15 as removal date at a constant elevation of 445 m above the WGS84 ellipsoid. As a result, the inclination, 78.33°, and the declination, 11°, were used to reduce the data to the north pole as shown in Figure 6.24b. In general, the high-density patterns coincides with areas with positive high magnetic response. Interestingly, we have found three regions having both high magnetic response and high bulk densities. The regions are outlined with black dash lines. As Skaar (2014) suggested that promising magmatic Ni-Cu-PGE (platinum-group-elements) mineralization appears related to the mafic/ultramafic intrusions such as Gallujavri region. More details on the correlation between the magnetic anomaly map and the density distribution could be gained by cluster analysis.

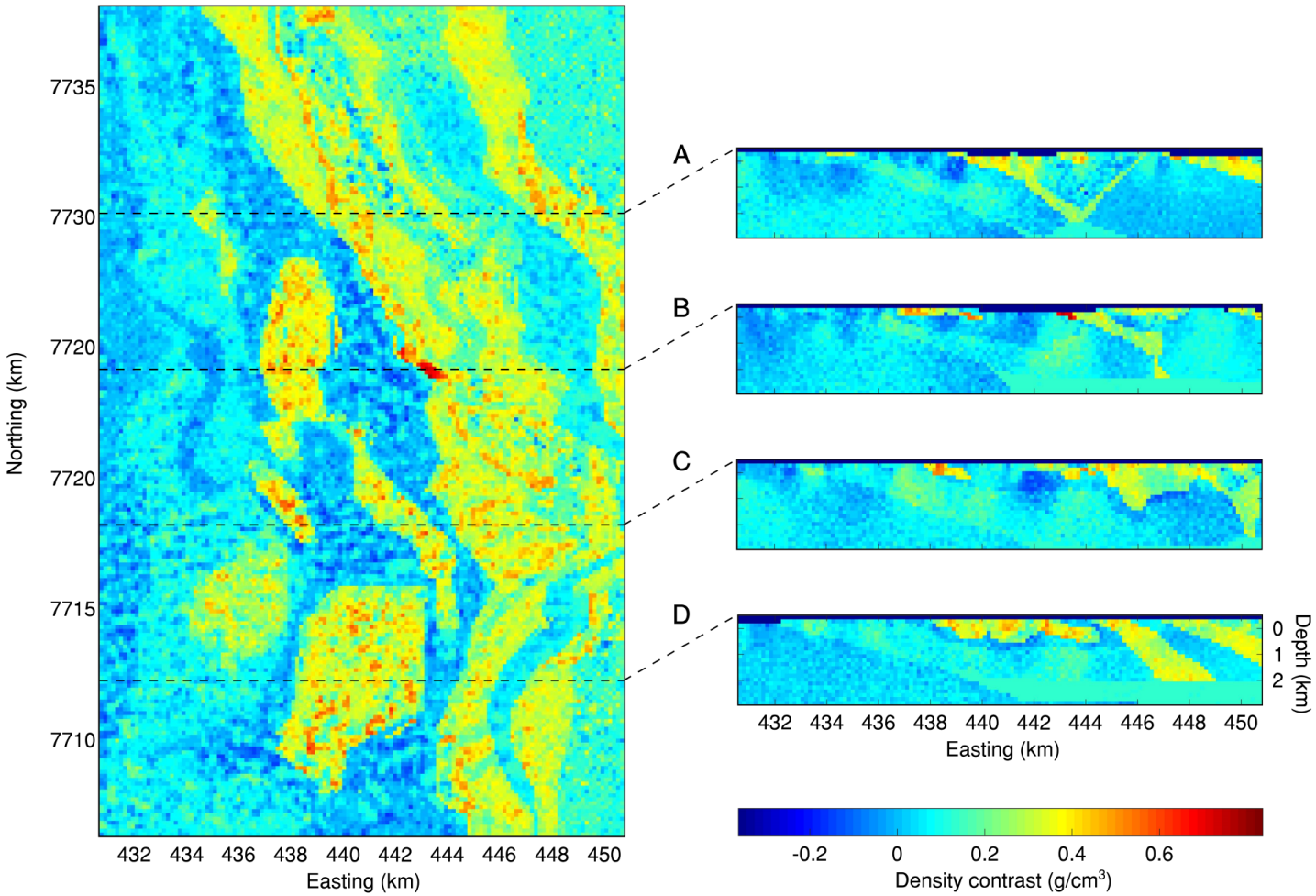

Figure 6.22: A plan view of the average model and four cross sections denoted by black dash lines from A to D, respectively.

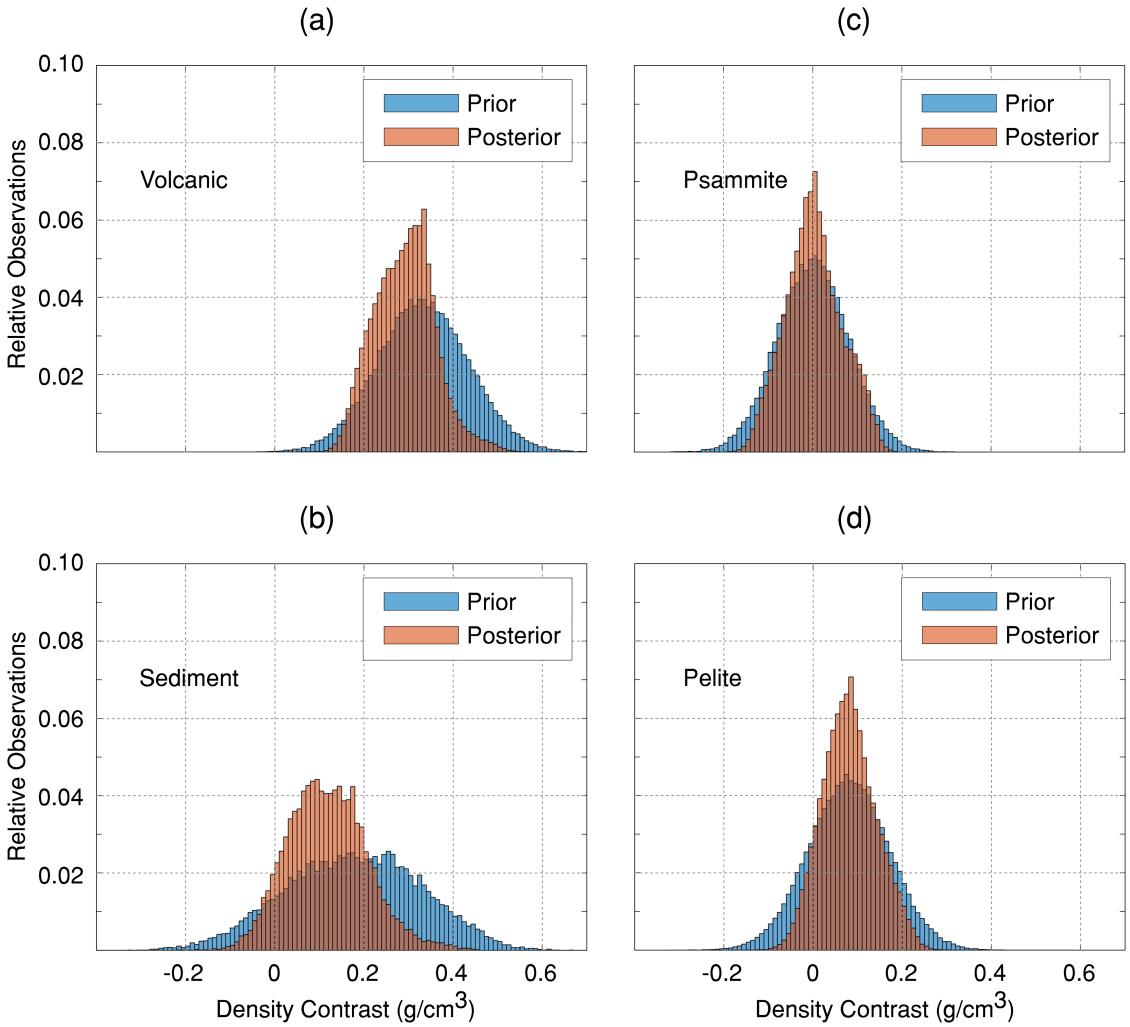

Figure 6.23: Comparison between the prior density distributions and the posterior density distributions.

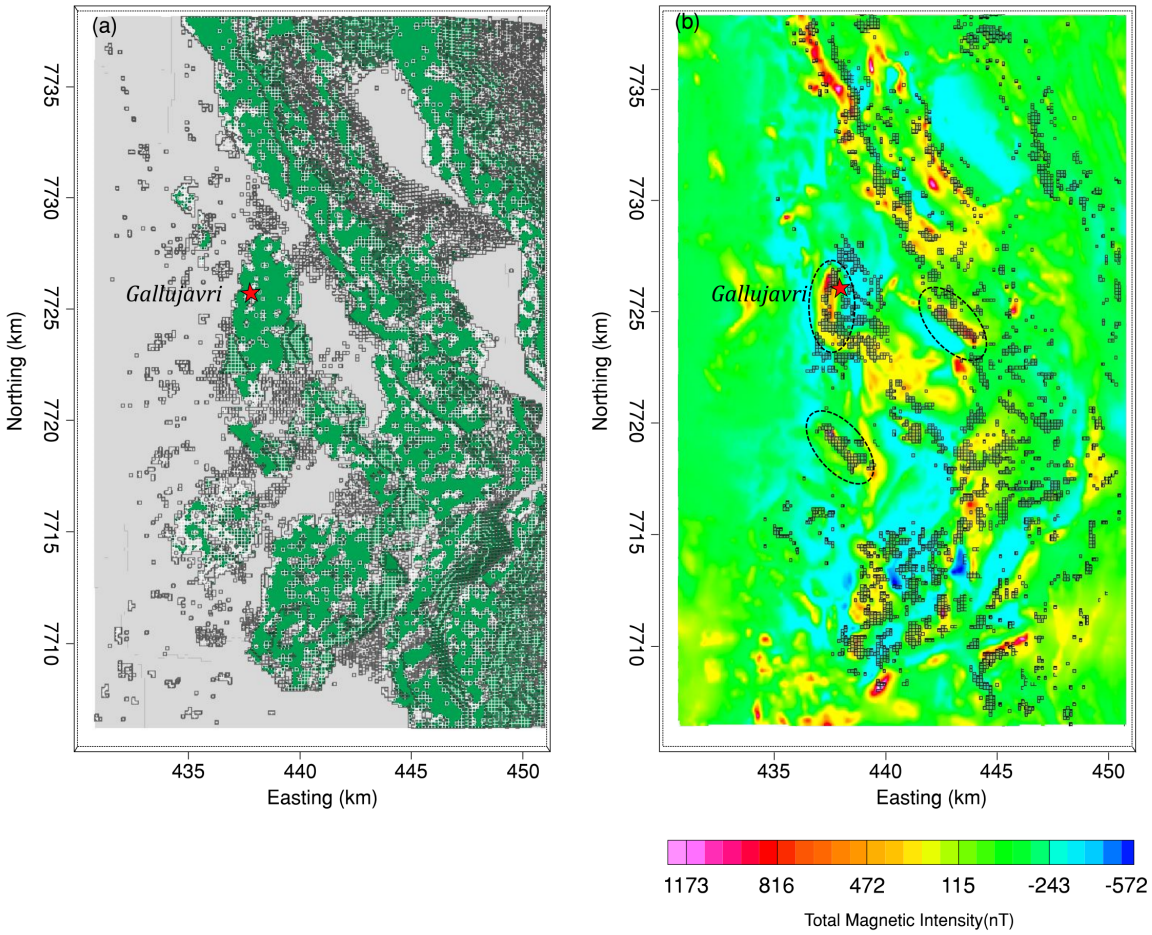

Figure 6.24: The volume-rendered image of the 3D density-contrast of the average model. (a) Voxel with density contrast greater than 0.2 g/cm^3 were kept and otherwise clipped. (b) Voxel with density contrast greater than 0.4 g/cm^3 were kept and otherwise clipped. In comparison, the total magnetic intensity which has been reduced to the pole is also provided. The leveled total magnetic intensity was then IGRF corrected using the 2010 model, 2011/08/15 as the removal data (The inclination is 78.33°, and the declination is 11°) at a constant elevation of 445 m above the WGS84 ellipsoid.

6.9 Conclusions

We have examined the influence of the prior noise reduction on the inversion and the usefulness of the various combinations of gravity gradient data in the inversion and have acquired seven density models of the survey area, accordingly. We applied the stochastic inversion to the gravity gradient data based on the Bayesian framework, which provides an ensemble of solutions resulting in the availability of retrieving the associated statistics, such the arithmetic mean and standard deviation.

The inversion results suggest that the short-wavelength information missing in the model by Skaar (2014) has been recovered after the inversions and modeling geology setting of a survey area with constant density is apparently insufficient to exploit the full content of the AGG data. Second, the noise reduction is not necessary in our case because the airborne gravity gradient data have been filtered so that the existing noise levels are insignificant for the inversions. It is also because the inversion itself also behaves like a band-pass filter which rejects the incompatible content in the data. It is demonstrated that even the difference with the standard deviation of 5 Eö due to the construction process hardly influences the results of the inversion. So inverting either the measured or the constructed data in our case can equally serve the purpose of interpretation. Furthermore, inverting six or five components does not necessarily provide as extra information in our case and it turns out that the three-component inversion is a practical compromise in our case.

To simplify the interpretation, we use an average model extracted from the derived mean models to understand the density distribution of the survey area. And the high contrast to the volcanic rock in the Bakkilivarri Formation makes up the major contribution to the gravity gradients. Besides, the promising magmatic Ni-Cu-PGE mineralization is considered to be around high-density contrast intrusions in the Karasjok area. Evidently, inversion of gravity gradiometry is a useful tool for discovering detailed density distribution of the area of interest. However, care must be taken while doing inversion based on the Bayesian approach because a failure of representing the real scenario of sparsely outcropped lithological units will certainly mislead the interpretation.

Chapter 7

Conclusions and Outlook

This thesis has presented an iterative noise reduction method and a fast equivalent source technique. These new techniques were applied to an AGG dataset of the Karasjok region. In addition, the AGG dataset was inverted for the density distribution.

The iterative noise method successfully suppressed high-frequency noise with the help of the given noise levels. With carefully selected parameters, the resulting residual, which can be considered as noise, differs from the input data. This method has been shown to be able to identify both high-frequency noises and systematic errors in the AGG data. In summary, the iterative approach, capable of reducing the noise in a semi-automatic way, is preferable to simple bandwidth filtering. However, like other low-pass filters, the method also has to be applied to multi-component datasets separately, which may introduce inconsistency between gravity gradient components.

The fast equivalent source technique proposed in Chapter 5 can naturally preserve the consistency between difference gravity gradients. By applying the method to the AGG data, it has jointly reduced noise in the measured data effectively without corrupting their consistency. In comparison with the routinely processed date which meet industry standard, the results show great resemblance, further confirming the reliability of the new approach. Also, an approach to estimate the density of the topography of the survey area based on the method was also presented. The estimation method can be useful to have an overview of the topography of the survey area, especially when only sparse pertrophyiscal data are available in a survey area.

By inverting seven combinations of gravity gradient tensor components from the AGG data, seven density models of the Karasjok area were acquired, accordingly. Additionally, the results suggest that the short-wavelength information missing in the model by Skaar (2014) has been recovered after the inversions and modeling geology setting of a survey

area with constant density is apparently insufficient to exploit the full content of the AGG data. Regarding whether noise reduction is necessary, it depends on the type of the noise and existing noise level. In our case, the AGG have been routinely low-pass filtered. The noise level in the data is relatively insignificant. And the noise determined by the new noise reduction method presented in Chapter 4 visually behaves like zero-mean Gaussian noise. It means that the noise is uncorrelated. If either of the conditions has been changed, the results may not be the same. As a result, the prior noise reduction does not necessarily improve inversion results. On the contrary, noise reduction should be carefully done, especially when data have already been routinely filtered. It is noteworthy that once the inconsistency between gravity gradients have been introduce, inconsistency can be problematic inversion. In our case, inverting the noise-reduced measured data fails to deliver equally distinct result in comparison with the one without the noise reduction. It seems that the inversion works like a band-pass filter which rejects some meaningless contents in the data. Because even the relatively bigger difference due to the construction process does not influence the inversions in a significant way. Therefore, to start any inversion with measured data first is recommended. Unless the inversion results are not acceptable, then it is reasonable to consider to reduce noise in the input data. Likewise, the results indicate that the measured data and constructed both can be used for inversion because the stochastic inversion itself has some noise immunity.

More importantly, with the help of $\mathbf{G}_{\mathrm{DD}}$, the depth sensitivity of the inversion of $\mathbf{G}_{\mathrm{NE}}$, $\mathbf{G}_{\mathrm{UV}}$, and $\mathbf{G}_{\mathrm{DD}}$ has been improved. It means that the $\mathbf{G}_{\mathrm{DD}}$ should be always included to recover deep information. However, $\mathbf{G}_{\mathrm{DD}}$ and other components can be only acquired by applying the construction process. Also, the results show that multi-component inversion is advantageous because of more constraints. As a result, the constructed components should be considered for inversion.

In our case, it turns out that the inversion of $\mathbf{G}_{\mathrm{NE}}$, $\mathbf{G}_{\mathrm{UV}}$, and $\mathbf{G}_{\mathrm{DD}}$ is considered an acceptable compromise, in terms of the reliability and computation complexity. This conclusion is drawn by comparing all the resolved models with the average model. However, in practice, instead of inverting only one type of input data or one subset of FTG data to find an optimum solution or searching for an optimum combination of FTG components, it is recommended to invert different combinations of gravity gradient components to retrieve an averaged solution from the acquired solutions. First of all, because non-uniqueness inheres in geophysical inverse problems. Second, because the averaged solution

is relatively more reliable and stable from statistical perspective.

At last, stochastic inversion of gravity gradient data is a useful tool for discovering detailed density distribution of the area of interest. However, it is worth noting that over/under-representing sparsely outcropped lithological units will certainly mislead the interpretation in stochastic inversion.

Possible next steps The internal consistency of the gravity gradient tensor is of great importance for data processing, thus developing iterative noise reduction method able to deal with multiple components is beneficial. To achieve this, an exact and mathematically rigorous relation between the gravity gradient components needs to be included.

Alternatively, an even faster method to compute equivalent source is invariably preferable. The method presented in Chapter 5 still has some room for optimization so as to further reduce the calculation time. In this thesis, the fast equivalent source method was only applied to two-component AGG measurements. Therefore, the application to real FTG measurements is a promising target for future investigations. Interestingly, the concept of the method can also be further developed for 3D inversion with the help of the 3D forward modeling method of potential fields in the wavenumber domain as proposed by Tontini et al. (2009), which would theoretically lead to significant reductions in computation time for inversion for large datasets.

Geophysical prospecting, interpretation, and analysis usually are relying on resolved physical property maps derived from inversion or imaging methods. Since a FALCON AGG survey is always accompanied by magnetometry, the observed total magnetic intensity (TMI) could potentially be exploited to give more insights into the potential mineral deposits, particularly if the mineralization is due to the concentration of magnetic minerals. Especially, if inversion of TMI is done, more details could be retrieved with the help of cluster analysis between a resolved susceptibility model and the density model.

Bibliography

Barnes, G. and J. Lumley (2011). Processing gravity gradient data. *Geophysics* 2.(76), I33–I47.

Barnes, Gary J., John M. Lumley, Phill I. Houghton, and Richard J. Gleave (2011). Comparing gravity and gravity gradient surveys. *Geophysical Prospecting* 59.(1), 176–187.

Blakely, Richard J. (1996). *Potential theory in gravity and magnetic applications*. Cambridge University Press.

Bosch, Miguel, Ronny Meza, Rosa Jimenez, and Alfredo Hoenig (2006). Joint gravity and magnetic inversion in 3D using Monte Carlo methods. *Geophysics* 71.(4), G153–G156.

Bouman, Johannes, Jörg Ebbing, Sjef Meekes, Rader Abdul Fattah, Martin Fuchs, Sofie Gradmann, Roger Haagmans, Verena Lieb, Michael Schmidt, Denise Dettmering, et al. (2015). GOCE gravity gradient data for lithospheric modeling. *International Journal of Applied Earth Observation and Geoinformation* 35, 16–30.

Braathen, Alvar and Børre Davidsen (2000). Structure and stratigraphy of the Palaeoproterozoic Karasjok Greenstone Belt, north Norway-regional implications. *Norsk Geologisk Tidsskrift* 80.(1), 33–50.

Briggs, Ian C. (1974). Machine contouring using minimum curvature. *Geophysics* 39.(1), 39–48.

Chen, J. and JC. Macnae (1997). Terrain corrections are critical for airborne gravity gradiometer data. *Exploration Geophysics* 28.(1/2), 21–25.

Chinnery, MA. (1961). Terrain corrections for airborne gravity gradient measurements. *Geophysics* 26.(4), 480–489.

Cooper, GRJ. (2002). Fixed point inversion of geophysical data. *Computers & Geosciences* 28.(7), 799–808.

Dampney, C. N. G. (1969). The equivalent source technique. *Geophysics* 34.(1), 39–53.

Davis, Kristofer and Y. Li (2011). Joint processing of total-field and gradient magnetic data. *Exploration Geophysics* 42.(3), 199–206.

DiFrancesco, D., A. Grierson, D. Kaputa, and T. Meyer (2009a). Gravity gradiometer systemsadvances and challenges. *Geophysical Prospecting* 57.(4), 615–623.

DiFrancesco, D., T. Meyer, A. Christensen, and Des FitzGerald (2009b). Gravity gradiometrytoday and tomorrow. *11th SAGA Biennial technical meeting and exhibition*.

Dransfield, M. and B. Milkereit (2007). Airborne gravity gradiometry in the search for mineral deposits. *Proceedings of Exploration 07: Fifth Decennial International Conference on Mineral Exploration edited by B. Milkereit*, 341–354.

Dransfield, M., A. Christensen, M. Rose, P. Stone, and P. Diorio (2001). FALCON test results from the Bathurst Mining Camp. *Exploration Geophysics* 32.(4), 243–246.

Dransfield, M. H. and A. N. Christensen (2013). Performance of airborne gravity gradiometers. *The Leading Edge* 32.(8), 908–922.

Dransfield, Mark and Yi Zeng (2009). Airborne gravity gradiometry: Terrain corrections and elevation error. *Geophysics* 74.(5), I37–I42.

Dransfield, MH., MJ. Buckingham, C. Edwards, FJ. Van Kann, AG. Mann, R. Matthews, and PJ. Turner (1991). Gravity gradiometry for geophysical prospecting. *Exploration Geophysics* 22.(1), 107–110.

Evstifeev, MI. (2017). The state of the art in the development of onboard gravity gradiometers. *Gyroscopy and Navigation* 8.(1), 68–79.

FitzGerald, Desmond J. and Horst Holstein (2006). Innovative data processing methods for gradient airborne geophysical data sets. *The Leading Edge* 25.(1), 87–94.

Fontanini, Francesco (2016). Optimization strategies for Markov chain Monte Carlo inversion of seismic tomographic data. PhD thesis. Jena.

Forsberg, Rene (1984). *A study of terrain reductions, density anomalies and geophysical inversion methods in gravity field modelling*. Tech. rep. Ohio State Univ Columbus Dept Of Geodetic Science and Surveying.

Fullagar, Peter and Pears Glenn (2010). From gravity gradients to density gradients. *Airborne Gravity 2010 - Abstracts from the ASEG-PESA Airborne Gravity 2010 Workshop: Edited by Lane. J. L. and Published jointly by Geoscience Australia and the Geological Survey of New South Wales, Geoscience Australia Record 2010/23 and GSNSW File GS2010/0457*.

Geyer, Charles (2011). Introduction to markov chain monte carlo. *Handbook of markov chain monte carlo* 20116022, 45.

Götze, H, Sabine Schmidt, Christine Fichler, and MR Alvers (2007). IGMAS+ a new 3D gravity, FTG and magnetic modeling software. *AGU Fall Meeting Abstracts*.

Guillen, Antonio, Gabriel Courrioux, Ph Calcagno, Richard Lane, Terry Lees, and Philip McInerney (2004). Constrained gravity 3D litho-inversion applied to Broken Hill. *ASEG Extended Abstracts* 2004.(1), 1–6.

Hastings, W Keith (1970). Monte Carlo sampling methods using Markov chains and their applications. *Biometrika* 57.(1), 97–109.

Hinze, William J (2003). Bouguer reduction density, why 2.67? *Geophysics* 68.(5), 1559–1560.

Hofmeyer, G. M. and C. A. Affleck (1994). *Rotating accelerometer gradiometer*. Google Patents.

Jekeli, Christopher (2006). Airborne gradiometry error analysis. *Surveys in geophysics* 27.(2), 257–275.

Jirigalatu, Jörg Ebbing, and Josef Sebera (2016). A new noise reduction method for airborne gravity gradient data. *Exploration Geophysics* 47.(4), 296–301.

Kass, Andy M. and Yaoguo Li (2008). Practical aspects of terrain correction in airborne gravity gradiometry surveys. *Exploration Geophysics* 39.(4), 198–203.

Kellogg, Oliver Dimon (2012). *Foundations of potential theory*. Vol. 31. Springer Science & Business Media.

Krill, AG. (1985). Svecokarelian thrusting with thermal inversion in the Karasjok-Levajok area of the northern Baltic Shield. *Norges Geologiske Undersøkelse Bulletin* 403, 89–101.

Landweber, Louis (1951). An iteration formula for Fredholm integral equations of the first kind. *American Journal of Mathematics* 73.(3), 615–624.

Lee, James B. (2001). FALCON gravity gradiometer technology. *Exploration Geophysics* 32.(3/4), 247–250.

Leliévre, Peter G, Colin G Farquharson, and Charles A Hurich (2012). Joint inversion of seismic traveltimes and gravity data on unstructured grids with application to mineral exploration. *Geophysics* 77.(1), K1–K15.

Li, X. (2015). Curvature of a geometric surface and curvature of gravity and magnetic anomalies. *Geophysics* 80.(1), G15–G26.

Li, Xiong and Michel Chouteau (1998). Three-dimensional gravity modeling in all space. *Surveys in Geophysics* 19.(4), 339–368.

Li, Y. and D. W. Oldenburg (1996). 3D inversion of magnetic data. *Geophysics* 61.(2), 394–408.

— (1998). 3-D inversion of gravity data. *Geophysics* 63.(1), 109–119.

Li, Yaoguo and Douglas W. Oldenburg (2010). Rapid construction of equivalent sources using wavelets. *Geophysics* 75.(3), L51–L59.

Li, Yaoguo et al. (2001). Processing gravity gradiometer data using an equivalent source technique. *2001 SEG Annual Meeting*. Society of Exploration Geophysicists.

Martinez, C., Y. Li, R. Krahenbuhl, and M. A. Braga (2013). 3D inversion of airborne gravity gradiometry data in mineral exploration: A case study in the Quadrilatero Ferrifero, Brazil. *Geophyiscs* 78.(1), B1–B11.

Martinez, Cericia and Yaoguo Li (2016). Denoising of gravity gradient data using an equivalent source technique. *Geophysics* 81.(4), G67–G79.

Metzger, Ernest H (1982). Development experience of gravity gradiometer system. *IEEE PLANS*. Vol. 82, 323–332.

Midtun, R (1988). Karasjok grönnsteinsbeltet: Regional geofysisk og geologisk tolkning. *NGU Skrifter* 88, 19.

Nabighian, M. N., M. E. Ander, V. J. S. Grauch, R. O. Hansen, T. R. LaFehr, Y. Li, W. C. Pearson, J. W. Peirce, J. D. Phillips, and M. E. Ruder (2005). Historical development of the gravity method in exploration. *Geophysics* 70.(6), 63ND–89ND.

Nillsson, Lars Petter and Morten Often (2006). *A summary report on the Ni-Cu-PGE occurences and their host rocks in the Precambrian of Finnmark*. Tech. rep. Norges Geologiske Undersøkelse, pp. 79+.

Nilsson, L. P., Peter M. Ihlen, Morten Often, Jon Are Skaar, and Rognvald Boyd (2015). Gallujavri and Raitevarri Potentially Large Deposits in the Karasjok Greenstone Belt. 36.

Often, M (1985). The Early Proterozoic Karasjok greenstone belt, Norway: A preliminary description of lithology, stratigraphy and mineralization. *Norges Geologiske Undersøkelse Bulletin* 403, 75–88.

Oliveira Jr., Vanderlei C., Valria C. F. Barbosa, and Leonardo Uieda (2013). Polynomial equivalent layer. *Geophysics* 78.(1), G1–G13.

Oliveira Lyrio, Julio Cesar Soares de, Luis Tenorio, and Yaoguo Li (2004). Efficient automatic denoising of gravity gradiometry data. *Geophysics* 69.(3), 772–782.

Pajot, Gwendoline, Olivier De Viron, Michel Diament, MF. Lequentrec-Lalancette, and Valentin Mikhailov (2008). Noise reduction through joint processing of gravity and gravity gradient data. *Geophysics* 73.(3), I23–I34.

Paoletti, V, M Fedi, F Italiano, G Florio, and S Ialongo (2016). Inversion of gravity gradient tensor data: does it provide better resolution? *Geophysical Journal International* 205.(1), 192–202.

Pawlowski, Bob (1998). Gravity gradiometry in resource exploration. *The Leading Edge* 17.(1), 51–52.

Pawlowski, Robert S. (1994). Green's equivalent-layer concept in gravity band-pass filter design. *Geophysics* 59.(1), 69–76.

Pilkington, M. and P. Shamsipour (2014). Noise reduction procedures for gravity-gradiometer data. *Geophysics* 79.(5), G69–G78.

Pilkington, Mark (2012). Analysis of gravity gradiometer inverse problems using optimal design measures. *Geophysics* 77.(2), G25–G31.

— (2014). Evaluating the utility of gravity gradient tensor components. *Geophysics* 79.(1), G1–G14.

Portniaguine, Oleg and Michael S. Zhdanov (1999). Focusing geophysical inversion images. *Geophysics* 64.(3), 874–887.

Roy, Kalyan Kumar (2007). *Potential theory in applied geophysics*. Springer Science & Business Media.

Rummel, R and M van Gelderen (1992). Spectral analysis of the full gravity tensor. *Geophysical Journal International* 111.(1), 159–169.

Sanchez, Vinicio, David Sinex, Yaoguo Li, Misac Nabighian, David Wright, and David vonG Smith (2005). Processing and Inversion of Magnetic Gradient Tensor Data for UXO Applications. *Symposium on the Application of Geophysics to Engineering and Environmental Problems 2005*. Society of Exploration Geophysicists, 1193–1202.

Sebera, Josef, Michal Šprlák, Pavel Novák, Aleš Bezděk, and Miloš Val'ko (2014). Iterative spherical downward continuation applied to magnetic and gravitational data from satellite. *Surveys in Geophysics* 35.(4), 941–958.

Sen, Mrinal K and Paul L Stoffa (2013). *Global optimization methods in geophysical inversion*. Cambridge University Press.

Shamsipour, Pejman, Denis Marcotte, Michel Chouteau, and Pierre Keating (2010). 3D stochastic inversion of gravity data using cokriging and cosimulation. *Geophysics* 75.(1), I1–I10.

Siedlecka, A (1985). Geology of the Iesjav'ri-Skoganvarre area, Northern Finnmarksvidda, North Norway. *Nor. geol. unders. Bull* 403, 103–112.

Siqueira, Fillipe C. L., Vanderlei C. Oliveira Jr., and Valria C. F. Barbosa (2017). Fast iterative equivalent-layer technique for gravity data processing: A method grounded on excess mass constraint. *Geophysics* 82.(4), G57–G69.

Skaar, Jon Are (2014). 3D geophysical and geological modelling of the Karasjok Greenstone Belt. MA thesis. NTNU.

Slotnick, Morris Miller (1932). Curvature of equipotential surfaces. *AAPG Bulletin* 16.(12), 1250–1259.

Stone, Peter M and Andrew Simsky (2001). Constructing high resolution DEMs from airborne laser scanner data. *ASEG Extended Abstracts* 2001.(1), 1–4.

Tarantola, Albert (2005). *Inverse problem theory and methods for model parameter estimation*. SIAM.

Tontini, F. Caratori, L. Cocchi, and C. Carmisciano (2009). Rapid 3-D forward model of potential fields with application to the Palinuro Seamount magnetic anomaly (southern Tyrrhenian Sea, Italy). *Journal of Geophysical Research: Solid Earth* 114.(B2).

Vio, R., J. Bardsley, M. Donatelli, and W. Wamsteker (2005). Dealing with edge effects in least-squares image deconvolution problems. *Astronomy & Astrophysics* 442.(1), 397–403.

While, James, Andrew Jackson, Dirk Smit, and Ed Biegert (2006). Spectral analysis of gravity gradiometry profiles. *Geophysics* 71.(1), J11–J22.

Wu, Leyuan and Gang Tian (2014). High-precision Fourier forward modeling of potential fields. *Geophysics* 79.(5), G59–G68.

Xia, Jianghai, Donald R. Sprowl, and Dana Adkins-Heljeson (1993). Correction of topographic distortions in potential-field data: A fast and accurate approach. *Geophysics* 58.(4), 515–523.

Zeng, Xiaoniu, Xihai Li, Juan Su, Daizhi Liu, and Hongxing Zou (2013). An adaptive iterative method for downward continuation of potential-field data from a horizontal plane. *Geophysics* 78.(4), J43–J52.

Zengerer, M, R Paterson, and C Campbell (2016). Apparent Terrain Density Estimations with Variable Terrain Corrections Using Stochastic Inversion. *78th EAGE Conference and Exhibition 2016*.

Zhao, Guangdong, Bo Chen, Longwei Chen, Jianxin Liu, and Zhengyong Ren (2018). High-accuracy 3D Fourier forward modeling of gravity field based on the Gauss-FFT technique. *Journal of Applied Geophysics* 150, 294 –303.

Zhdanov, M. S., R. Ellis, and S. Mukherjee (2004). Threedimensional regularized focusing inversion of gravity gradient tensor component data. *Geophysics* 69.(4), 925–937.

Zhdanov, Michael S (2002). *Geophysical inverse theory and regularization problems*. Vol. 36. Elsevier.

Zhdanov, Michael S, Xiaojun Liu, Glenn A Wilson, and Le Wan (2011). Potential field migration for rapid imaging of gravity gradiometry data. *Geophysical Prospecting* 59.(6), 1052–1071.